LONDON'S GLOBAL UNIVERSITY

Understanding Gas and Energy Storage in Geological Formations with Molecular Simulations

Kai Bin Yu

Department of Chemical Engineering

University College London

A thesis submitted for the degree of

Doctor of Philosophy

March 2023

Declaration of Authorship

I, Kai Bin Yu confirm that the work presented in this thesis is my own. Where information has been derived from other sources, I confirm that this has been indicated in the thesis.

Acknowledgements

I would like to thank my esteemed supervisor Dr Özgür Yazaydın, who always strives for novelty without compromising research integrity. Without him, this thesis would have been impossible. Thanks to Prof George Jackson and Dr Andrew Haslam at Imperial for introducing me to the microscopic world of jiggling molecules. I also want to thank Prof Geoffrey Maitland, my Master's supervisor, for his wisdom and advice. I have been supported by a departmental scholarship made possible by a legacy from H. Walter Stern, to whom I am forever grateful for this life-changing yet fruitful experience. I also want to express my gratitude to UCL Chemical Engineering for this prestigious award. IT Services for the fantastic work experience and the support from the ARC and Library Services teams. Lanita, François, Freddie, Sada, Aydın, Ben, Tran, and Selman went through this journey with me. Keeping the tidsoptimist in me in check, being able to vent to them has been meaningful. Lee for being my favourite person at UCL, keeping me safe and filling me with yummy doughnuts. A special thank Mr Chimken for being my *bestest* friend who always stands by my side through the chaotic journey of growing up, sitting with me in the trenches, and now I only see daylight, blue skies forever. Holding onto that trapeze in a world of whirlwinds, not letting go. Ronnie for his never-ending motivation that inspired me to go above and beyond. Jelena & Kyle for offering me a shelter during tough times. Andrea for helping me to understand the changes in my life and the meme sharing. Tommy, Jerry, Anthony, and Danny for the melodrama and supercuts. I remember it all too well. Taught me to enjoy moments like snow on the beach, this is me trying to let the light in. Eunice, Jodie, Kean Sin, Li Ann, Jackson, Pei Kiat, Wei Yine, Yang Chen, Michael for being friends, tolerated multiple versions of me. Friends that I made on Telegram, Chris, Soltan, Takanu, César, Aymeric, Kris, and Kieran. We are just beautiful people with beautiful problems. Heena, Rob, Vicki, and Martin for making me a better swimmer. The Victoria League, Doreen and Laura for housing me. Finally, I am grateful to my family, they supported me through thin and thick. Their unconditional love and endless patience have enabled me to pursue a PhD as a first-generation university student.

UCL Research Paper Declaration Form: referencing the doctoral candidate's own published work(s)

Please use this form to declare if parts of your thesis are already available in another format, e.g. if data, text, or figures:

- have been uploaded to a preprint server;
- are in submission to a peer-reviewed publication;
- have been published in a peer-reviewed publication, e.g. journal, textbook.

This form should be completed as many times as necessary. For instance, if you have seven thesis chapters, two of which containing material that has already been published, you would complete this form twice.

1. For a research manuscript that has already been published (if not yet published, please skip to section 2)**:**		
a) Where was the work published? (e.g. journal name)	The Journal of Physical Chemistry C	
b) Who published the work? (e.g. Elsevier/Oxford University Press):	American Chemical Society	
c) When was the work published?	04/05/2020	
d) Was the work subject to academic peer review?	Yes	
e) Have you retained the copyright for the work?	Yes	
[If no, please seek permission from the relevant publisher and check the box next to the below statement]: *I acknowledge permission of the publisher named under 1b to include in this thesis portions of the publication named as included in 1a.*		
2. For a research manuscript prepared for publication but that has not yet been published (if already published, please skip to section 3)**:**		
a) Has the manuscript been uploaded to a preprint server? (e.g. medRxiv):	Please select.	**If yes, which server?** Click or tap here to enter text.
b) Where is the work intended to be published? (e.g. names of journals that you are planning to submit to)	Click or tap here to enter text.	
c) List the manuscript's authors in the intended authorship order:	Click or tap here to enter text.	
d) Stage of publication	Please select.	
3. For multi-authored work, please give a statement of contribution covering all authors (if single-author, please skip to section 4)**:**		
Kai Bin Yu: Data curation, Formal analysis, Methodology, Visualization, Writing – original draft; A. Ozgur Yazaydin: Conceptualization, Methodology, Writing – review & editing, Project administration.		
4. In which chapter(s) of your thesis can this material be found?		

Chapter 3			
5. e-Signatures confirming that the information above is accurate (this form should be co-signed by the supervisor/ senior author unless this is not appropriate, e.g. if the paper was a single-author work):			
Candidate:	Kai Bin Yu	**Date:**	28/07/2022
Supervisor/ Senior Author (where appropriate)**:**	Ozgur Yazaydin	**Date:**	28/07/2022

UCL Research Paper Declaration Form: referencing the doctoral candidate's own published work(s)

Please use this form to declare if parts of your thesis are already available in another format, e.g. if data, text, or figures:

- have been uploaded to a preprint server;
- are in submission to a peer-reviewed publication;
- have been published in a peer-reviewed publication, e.g. journal, textbook.

This form should be completed as many times as necessary. For instance, if you have seven thesis chapters, two of which containing material that has already been published, you would complete this form twice.

1. For a research manuscript that has already been published (if not yet published, please skip to section 2)**:**		
a) Where was the work published? (e.g. journal name)	Energy & Fuels	
b) Who published the work? (e.g. Elsevier/Oxford University Press):	American Chemical Society	
c) When was the work published?	01/10/2021	
d) Was the work subject to academic peer review?	Yes	
e) Have you retained the copyright for the work?	No	
[If no, please seek permission from the relevant publisher and check the box next to the below statement]: ☒ *I acknowledge permission of the publisher named under 1b to include in this thesis portions of the publication named as included in 1a.*		
2. For a research manuscript prepared for publication but that has not yet been published (if already published, please skip to section 3)**:**		
e) Has the manuscript been uploaded to a preprint server? (e.g. medRxiv):	Please select.	**If yes, which server?** Click or tap here to enter text.
f) Where is the work intended to be published? (e.g. names of journals that you are planning to submit to)	Click or tap here to enter text.	
g) List the manuscript's authors in the intended authorship order:	Click or tap here to enter text.	
h) Stage of publication	Please select.	
3. For multi-authored work, please give a statement of contribution covering all authors (if single-author, please skip to section 4)**:**		
Kai Bin Yu: Data curation, Formal analysis, Methodology, Visualization, Writing – original draft; Geoffrey M. Bowers: Conceptualization, Writing – review & editing; Narasimhan Loganathan: Conceptualization, Writing – review & editing; Andrey G. Kalinichev: Conceptualization, Writing – review & editing; A. Ozgur Yazaydin: Conceptualization, Methodology, Writing – review & editing, Project administration.		

4. In which chapter(s) of your thesis can this material be found?			
Chapter 4			
5. e-Signatures confirming that the information above is accurate (this form should be co-signed by the supervisor/ senior author unless this is not appropriate, e.g. if the paper was a single-author work):			
Candidate:	Kai Bin Yu	**Date:**	28/07/2022
Supervisor/ Senior Author (where appropriate)**:**	Ozgur Yazaydin	**Date:**	28/07/2022

UCL Research Paper Declaration Form: referencing the doctoral candidate's own published work(s)

Please use this form to declare if parts of your thesis are already available in another format, e.g. if data, text, or figures:

- have been uploaded to a preprint server;
- are in submission to a peer-reviewed publication;
- have been published in a peer-reviewed publication, e.g. journal, textbook.

This form should be completed as many times as necessary. For instance, if you have seven thesis chapters, two of which containing material that has already been published, you would complete this form twice.

1. For a research manuscript that has already been published (if not yet published, please skip to section 2)**:**		
a) Where was the work published? (e.g. journal name)	Journal of CO2 Utilization	
b) Who published the work? (e.g. Elsevier/Oxford University Press):	Elsevier	
c) When was the work published?	20/06/2022	
d) Was the work subject to academic peer review?	Yes	
e) Have you retained the copyright for the work?	Yes	
[If no, please seek permission from the relevant publisher and check the box next to the below statement]: *I acknowledge permission of the publisher named under 1b to include in this thesis portions of the publication named as included in 1a.*		
2. For a research manuscript prepared for publication but that has not yet been published (if already published, please skip to section 3)**:**		
i) Has the manuscript been uploaded to a preprint server? (e.g. medRxiv):	Please select.	**If yes, which server?** Click or tap here to enter text.
j) Where is the work intended to be published? (e.g. names of journals that you are planning to submit to)	Click or tap here to enter text.	
k) List the manuscript's authors in the intended authorship order:	Click or tap here to enter text.	
l) Stage of publication	Please select.	
3. For multi-authored work, please give a statement of contribution covering all authors (if single-author, please skip to section 4)**:**		
Kai Bin Yu: Data curation, Formal analysis, Methodology, Visualization, Writing – original draft; Geoffrey M. Bowers: Conceptualization, Writing – review & editing; A. Ozgur Yazaydin: Conceptualization, Methodology, Writing – review & editing, Project administration.		
4. In which chapter(s) of your thesis can this material be found?		

Chapter 5			
5. e-Signatures confirming that the information above is accurate (this form should be co-signed by the supervisor/ senior author unless this is not appropriate, e.g. if the paper was a single-author work):			
Candidate:	Kai Bin Yu	**Date:**	28/07/2022
Supervisor/ Senior Author (where appropriate)**:**	Ozgur Yazaydin	**Date:**	28/07/2022

Abstract

Methane (CH_4), the cleanest burning fossil fuel, has the potential to solve the energy crisis owing to the growing population and geopolitical tensions. Whilst highly calorific, realising its potential requires efficient storage solutions, which are safe and less energy-intensive during production and transportation. On the other hand, carbon dioxide (CO_2), the by-product of human activities, exacerbates global heating driving climate change. CH_4 is abundant in natural systems, in the form of gas hydrate and trapped gas within geological formations. The primary aim of this project was to learn how Nature could store such a large quantity of CH_4 and how we can potentially extract and replace the in-place CH_4 with atmospheric CO_2, thereby reducing greenhouse gas emissions. We studied this question by applying molecular dynamics (MD) and Monte Carlo (MC) simulation techniques. Such techniques allow us to understand the behaviour of confined fluids, i.e., within the micropores of silica and kerogen matrices. Our simulations showed that CH_4 hydrate in confinement could form under milder conditions than required, deviating from the typical methane-water phase diagram, complementing experimental observations. This research can contribute to artificial gas hydrate production via porous materials for gas storage. Besides that, the creation of 3D kerogen models via simulated annealing has enabled us to understand how maturity level affects the structural heterogeneity of the matrices and, ultimately CH_4 diffusion. Immature and overmature kerogen types were identified to having fast CH_4 diffusion. Subsequently, our proof-of-concept study demonstrated the feasibility of recovering CH_4 via supercritical CO_2 injection into kerogens. Insights from our study also explained why full recovery of CH_4 is impossible. A pseudo-second-order rate law can predict the kinetics of such a process and the replacement quantity. A higher CO_2 input required than the CH_4 recovered highlights the possibility of achieving a net-zero future via geological CO_2 sequestration.

Impact Statement

The world is facing a climate crisis, and transitioning to sustainable energy sources is essential to mitigate its effects. The demand for green and sustainable energy is increasing globally, causing significant emotional and financial strains on individuals and businesses. The energy industry typically takes years, if not decades, to develop and adopt new technology with high public impact, such as high-capacity batteries to store renewables, to minimise downtime. CH_4, the main component of natural gas, offers substantial advantages over other hydrocarbons due to higher energy density and lower CO_2 emissions. However, the future use of CH_4 as a fuel depends on safe and economical storage technologies.

Human activities have contributed to the dramatic increase in atmospheric CO_2 concentration since the industrial revolution, and a net zero future requires CO_2 to be captured and stored. Exploiting unconventional energy resources, such as shale, to complement the existing energy portfolio to timely meet the rapidly growing energy demand is crucial. Although CH_4 production via hydraulic fracturing is commercially viable, up to 80% of it remains unrecovered, not to mention the amount of water required and the toxicity of the additives used. There is a need for a safe replacement fluid that improves CH_4 yield and reduces CO_2 emissions simultaneously.

This thesis seeks to tackle these challenges from a nature-inspired chemical engineering angle by offering detailed molecular-level observations of the behaviour of fluids confined within the natural pore networks of sedimentary rocks. Such insights allow the scientific community and industry to understand how transformative synthetic materials can be tuned to mimic nature and drive the design of new solid-storage technology that can efficiently and safely store gases like H_2, CH_4, and CO_2 through artificial gas hydrate formation. These results could also help develop innovative strategies for enhanced CH_4 recovery from geological formations through CO_2 injection, and consequently enabling CO_2 sequestration. Decoupling the various phenomena at play raises several unanswered

fundamental engineering questions, including how does manipulating the composition and structure of synthetic materials affect the storage capacity and transport of fluids? How can state-of-the-art solid-storage technology help make energy production more sustainable and affordable? These and other fundamental questions highlight the need for more research to find solutions to the UCL Grand Challenges.

In conclusion, my research has the potential to have a significant impact on the energy industry, the environment, and society as a whole. It highlights the importance of investing in research to find solutions to the critical challenges we face. Within academia, my research could inspire new avenues of research and collaboration between academia and industry, leading to the development of safer and more cost-effective energy storage and extraction technologies. Outside academia, my research could revolutionise the energy industry, contributing to a cleaner environment, and helping to decarbonise the economy.

Contents

Chapter 1 Introduction

The significant consumption of fossil fuels, primarily petroleum, in the last decades to fuel economic growth and the associated environmental issues after combustion have forced humankind to shift attention towards using greener energy resources. Methane (CH_4), as the main component of natural gas, offers substantial advantages over other fossil fuels, i.e., higher energy density and resulting in approx. 40% less carbon dioxide (CO_2) emission when combusted in the same quantity as coal and petroleum. However, the future use of CH_4 as fuel strongly counts on pursuing safe and economical storage technologies. The current technology for CH_4 storage depends on high-pressure and low-temperature processes, with associated economic and environmental concerns, to produce compressed natural gas (CNG) and liquefied natural gas (LNG), respectively. CH_4 is available in abundant quantities as gas hydrates and adsorbed gas embedded within the micropores of kerogens found in sedimentary rocks of natural systems.[1–3] These unexploited and unconventional sources have been estimated to be at least twice of that of all other fossil fuels combined,[4–6] enough to fill the gap whilst we transition to renewable sources. Natural systems found on earth are a product of evolution over the course of eons that favours efficient design in macroscopic and microscopic scales. Such optimisation is invisible to the naked eye, particularly at the microscopic scale. Molecular modelling is well suited to be used as a tool to uncover insights in length and time scale that experiments cannot probe in detail. In addition, fluids confined in complex porous environments are known to exhibit different properties compared to their bulk counterparts.[7] Whilst isotropic properties of bulk fluids are well defined, the behaviour of fluids under confinement can be considerably different due to strong fluid-substrate interactions and crowding effects when other fluid molecules are present near the surfaces.[8,9] This Thesis aims to advance understanding of the unique properties of porous sedimentary environments found in natural systems that facilitate gas and energy storage in enormous quantities at molecular scale. Furthermore, how we can exploit these characteristics when designing nature-inspired artificial energy

and gas storage solutions, e.g., solid CH_4 storage, CO_2 sequestration, etc., based on insights derived by molecular simulations. In **Chapter 2**, an introduction to the classical molecular simulation techniques employed in this Thesis will be presented.

Methane hydrates, also known as "flammable ice", are an energy-dense compound capable of storing up to 173 m^3 CH_4 per cubic metre.[10] They are commonly found in sediments and rocks under the seabed, which offers favourable thermodynamic conditions for hydrate formation. The phase equilibria and other thermophysical properties of bulk gas hydrates are well understood. However, attempts at reproducing hydrate formation at such thermodynamic conditions are hindered by slow formation kinetics. It is of crucial importance to understand the appearance of CH_4 hydrates and their stability, which governs hydrate formation and dissociation, in complex porous environments. By mimicking nature, we can obtain inspiration to improve the CH_4 storage capacity via nucleation and growth of artificial methane hydrates in porous media, similar to those found in deep-sea sediments. Silica is one of the most abundant subsurface materials and attracted considerable attention in systematic studies of fluids confined in their micro- and mesopores. Its outer layer is expected to be hydroxylated in the presence of water, resulting in a hydrophilic surface, and consequently affecting the behaviour of fluids entrapped within the pores. Besides that, interfacial water near the surface of the solid substrate has been shown to behave differently in terms of its structure and dynamics.[11,12] There is a need to understand the complex relationship between guest molecules, water and porous silica. Though this is still unclear to us, experimental results[13–17] have shown that confinement effects promote CH_4 hydrate formation under milder conditions than one would expect compared to bulk CH_4 hydrates. By taking advantage of the confinement effects in the nanocavities of silicas, gas hydrate can form under less demanding pressure and temperature conditions than nature and, more importantly, with faster kinetics. **Chapter 3** examines the effects of confinement on the formation of CH_4 hydrates in a slit-shaped silica micropore, as a proxy to that of hydrate-bearing sediments. Furthermore, the artificial

effects induced by applying tail corrections in such non-homogenous systems will also be highlighted.

Kerogens, another compound of focus in this Thesis, are a waxy mixture of complex hydrocarbons found in organic matter-rich sedimentary rocks in shale environments. They formed at the end of diagenesis and are slowly buried more deeply in the Earth to produce oil and gas as they undergo thermal maturation over geological timescale.[18] There are three main types of kerogens with varying maturity level, each carries a different amount of CH_4; however, the current exploitation technique can only recover about a fifth of the CH_4 in place,[19] not to mention the enormous environmental cost of the extraction process due to the use of toxic hydraulic fracturing fluids.[20,21] Gas transport in shale primarily occurs through diffusion,[22] however, due to the multiscale nature of the kerogen pore network, which assumes a broad spectrum of pore characteristics, e.g., connectivity, porosity, and tortuosity,[23,24] depending on their maturity level further complicates the mechanisms of gas transport. Understanding the diffusion behaviour of CH_4 in these microporous kerogen pores allows us to uncover the factors affecting gas recovery as well as the kinetics of the recovery process. Owing to experimental challenges in isolating pure kerogens from shale matrices, the exact structures of bulk kerogens are currently unknown to us. In **Chapter 4**, we constructed various 3D kerogen models of different maturity levels to address this, covering a broad region of the van Krevelen diagram.[25] Through grand canonical Monte Carlo (GCMC) simulations, we determined the amount of total gas in place (GIP) at reservoir-relevant conditions and subsequently computed the corresponding self-diffusivity of the in-place CH_4. This has allowed us to assess how maturity level as well as changes in physical characteristics, such as helium accessible volume, total surface area, pore size distribution, etc., upon the uptake of CH_4 affect the diffusion behaviour of in-place CH_4. To conclude this Chapter, the top two kerogen types with fast CH_4 diffusivity are reported.

In recent years, supercritical CO_2 has been proposed as an ideal candidate to replace the existing toxic fracking fluids used in the enhanced gas recovery processes. This is supported by the fact that kerogens preferentially adsorb CO_2 over CH_4.[26–40] Furthermore, the added benefit of using CO_2 is that the residual CO_2 remaining in kerogens after extraction could act as a carbon sink, i.e., geological CO_2 sequestration (GCS).[41–45] Thus far, the molecular mechanisms of CH4 displacement from kerogens through CO_2 injection are lacking. Moreover, it was unclear whether confinement effects due to the complex multiscale network of kerogen pores would affect the behaviour of the fluids entrapped within them and their extent to which they affect the replacement process. One of the criteria needed to achieve the commercial viability of the enhanced natural gas recovery process is that it must be rapid. Building on the knowledge obtained from earlier chapter, where immature (Type I-A) and overmature (Type II-D) kerogens were found to be the top two kerogen types with fast CH_4 diffusivity, we explored the use of CO_2 injection into their respective micropores as a means to recover the in-place CH_4 in **Chapter 5**. We injected supercritical CO_2 into kerogen slabs of Type I-A and Type II-D mimicking reservoir-relevant conditions and evaluated their CH_4 replacement ratio. The sorption induced strain due to CO_2 injection into the kerogen slabs is reported. The MSD profiles of adsorbed CO_2 on the micropores of kerogen slabs are compared to reveal the connectivity of micropores found in kerogen slabs of different maturity levels. In addition, the behaviour of recovered and residual CH_4 in Type II-D kerogens are also discussed to shed some light on the surrounding environments, which prevented the complete recovery of CH_4.

Finally, in **Chapter 6**, the overall achievements of this Thesis are summarised, and possible future research directions are suggested.

Chapter 2 The Theory

This present chapter offers an introduction to the theory and molecular simulation techniques necessary to understand the original work presented in this thesis. Although previous knowledge of statistical mechanics is not essential to read this chapter, the reader should be familiar with basic concepts of *classical* thermodynamics. There are many computational methods to simulate molecular system and the behaviour of its constituents at varying lengths and time scales, depending on the system of interest. These methods allow better prediction and understanding of materials, consequently, the development of new materials. Based on the resolution of the methods, they can be categorised into a few distinct types. From quantum mechanics (QM), molecular mechanics (MM) to meso-scale modelling, in descending order in terms of resolution. At the highest resolution, QM simulation based on first principles, by solving the Schrödinger equation and taking into account the electronic motions of molecules, it is impossible to study a large system size (number of atoms) with the currently available resources. Instead, classical molecular simulations, which rely on semi-empirical force fields, are commonly used to study less achievable systems with QM. A brief introduction to the molecular force field and classical molecular simulation techniques will be presented in the following section.

2.1 Background

Classical thermodynamics, which requires no knowledge at all of the underlying atoms or molecules, though successful in practical engineering problems, is not without its limitations. The *macroscopic* approach fails to describe, e.g., the differences in the behaviour of one fluid to another due to the differences in the constituent particles comprising the fluids. The realisation that thermodynamic properties are averages allows us to invoke statistical mechanics to link the macroscopic behaviour of materials and the microscopic interactions of particles that made up the bulk matter. The energy expression for a classical system of N interacting particles is the Hamiltonian, $\mathcal{H}$ (2.1), which is a function of positions and momenta of the particles. We can express $\mathcal{H}$ as the sum of

potential energy and kinetic energy in equation (2.2) below, a residual (configurational contribution) and ideal gas (kinetic contribution) parts, respectively, where one does not depend on another:

$$\mathcal{H}(\mathbf{r}^N, \mathbf{p}^N) \equiv \mathcal{H}(\mathbf{r}_1, \dots, \mathbf{r}_\mathrm{N}, \mathbf{p}_1, \dots, \mathbf{p}_\mathrm{N}) \tag{2.1}$$

$$\mathcal{H}(\mathbf{r}^N, \mathbf{p}^N) = U(\mathbf{r}^N) + \mathcal{K}(\mathbf{p}^N) \tag{2.2}$$

where $\mathbf{r}_1, \dots, \mathbf{r}_\mathrm{N}$ and $\mathbf{p}_1, \dots, \mathbf{p}_\mathrm{N}$ are the positions and momenta vector of the particles, respectively. In a simple atomic system, the kinetic energy term $\mathcal{K}$ can be expressed as:

$$\mathcal{K}(\mathbf{p}^N) = \sum_{\mathrm{i}=1}^{\mathrm{N}} \frac{\mathbf{p}_\mathrm{i}^2}{2\mathrm{m_i}} \tag{2.3}$$

Each ith particle of mass m_i has its own set position coordinates ($\mathbf{r} \equiv \{r_x, r_y, r_z\}$) and momentum coordinates ($\mathbf{p} \equiv \{p_x, p_y, p_z\}$). For a system of N particles, this collectively creates a point in a $6N$ dimensional phase space which corresponds to a microstate at a given time. A macrostate is specified by a few thermodynamic variables (e.g., volume (V), temperature (T), pressure (P), etc.). Many different microstates correspond to a single macrostate. For a given macrostate, many different microstates will be possible, and that each microstate may exist following the principle of equal *a priori* probabilities. For a system of large number of particles, it is more efficient to explore and sample points in phase space that are more probable to be explored by the system trajectory to yield satisfactory time averages of thermodynamic properties of interest. To circumvent this, Gibbs introduced a formalism called ensemble. A statistical ensemble is a complete collection of systems, in each of which the particles may have a different assignment in positions and momenta, but they are all characterised by common three macroscopic parameters of thermodynamic variables, e.g., N, V, T, P, energy (E) or chemical potential (μ). One can propose many different ensembles depending on the properties of interest one would like to compute. When a system is said to be ergodic, the ensemble average of a quantity is equivalent to the time average of the quantity. Ergodic hypothesis assumes that

the system will explore all possible states in the phase space when given sufficient time to evolve.

2.2 Force Field

Since the electronic structures of atoms are not considered in classical molecular simulations, it is essential to specify the connectivity of atoms and the intermolecular potentials that describe the interactions between atoms. A general functional form of the total potential energy of a molecular system, $U(\mathbf{r}^N)$ in equation (2.4);

$$\begin{aligned} U(\mathbf{r}^N) = & \sum_{bonds} k_b\left(r_{ij} - r_0\right)^2 + \sum_{angles} k_\theta\left(\theta_{ijk} - \theta_0\right)^2 \\ & + \sum_{torsions} \sum_{n} k_\omega\left[1 + \cos\left(n\omega_{ijkl} + \gamma\right)\right] \\ & + \sum_{non-bonded\ pairs\ i<j} \left[\frac{q_i q_j}{4\pi\epsilon_0\epsilon_r r_{ij}} + 4\epsilon_{ij}\left[\left(\frac{r_{ij}}{\sigma_{ij}}\right)^{-12} - \left(\frac{r_{ij}}{\sigma_{ij}}\right)^{-6}\right]\right] \end{aligned} \tag{2.4}$$

Here, $U(\mathbf{r}^N)$ is a function of the (nuclear) position of the of all atoms $\mathbf{r}^N$ and its derivatives give the forces acting on each atom. The contribution of the bonded interactions is described in the first three terms (bond stretchings, bond angle bendings and bond torsions, respectively) whereas the last two terms (Coulombic and 12–6 Lennard-Jones (LJ) potentials, respectively) represent pairwise non-bonded interactions. In detail, the first two harmonic terms describe the deformation energies of the bond lengths r_{ij} and bond angles θ_{ijk} from equilibrium values of r_0 and θ_0, respectively.

The first term is a sum over all bonds for every directly connected atom pairs ij. The second term is a sum over all angles θ_{ijk} between three connected atoms i, j and k. These terms with their corresponding force constant k_b and k_θ preserve the basic chemical structure of molecules and does not describe bond breaking and forming in chemical reactions. They can also be replaced with a more realistic functional form such as the Morse potential. For molecules with four consecutively connected atoms i, j, k and l, the third term with a cosine function describes the energy of a torsional rotation around three consecutive

covalent bonds, where k_ω is the dihedral force constant, multiplicity n refers to the number of potential energy minima over a period of rotation of 2π along the jk bond, ω is the torsional angle and the phase angle γ defines the position of the energy minima. The third term is a sum over all torsions, which can also include improper torsions in a molecular structure on three unconnected atoms bonded to a central atom.

For the non-bonded pair interactions, the fourth term represents the 12–6 Lennard-Jones (LJ) potential, where the repulsive and attractive interactions between atom pairs ij are described by an LJ well depth ϵ_{ij} and σ_{ij}, which is the distance where the interparticle potential is zero. In some force fields, the short-range repulsive term r_{ij}^{-12} is replaced with r_{ij}^{-9}, i.e., 9–6 LJ potential. For unlike atomic species, the LJ parameters ϵ_{ij} and σ_{ij} are calculated using Lorentz-Berthelot combining rules. The last term is the electrostatic interactions between two atoms with point charges q_i and q_j and interparticle separation r_{ij}, are described using the Coulomb's law, where ϵ_0 and ϵ_r are the permittivity of free space and relative dielectric constant, respectively.

Contributions from three-body or higher are rarely included in the functional form of the potential as it is very expensive to simulate. In many cases, three-body effects are accounted using an "effective" pair potential. Overall, the aforementioned parameters are usually derived from experimental data and DFT calculations of reference (small molecule) structures, and the fitting of or parameterisation of force fields is carried out with ensuring transferability in mind to allow wider application of the force fields.

2.3 Molecular Dynamics

Molecular dynamics (MD), developed by Alder and Wainwright in the 1950s for a system of hard spheres, is a computer simulation technique used to study the macroscopic thermodynamics properties of isolated molecular systems deterministically. The determinism of MD simulations is based on the laws of classical mechanics, which are deterministic and repeatable, given the same initial conditions. There is no involvement of

random number-based rotation, translation or displacement of atoms. The time evolution of a system with $\boldsymbol{N}$ atoms is obtained through integrating Newton's equations of motion (2.5) which gives the trajectory of positions ($\mathbf{r}^{\boldsymbol{N}}$) and momenta ($\mathbf{p}^{\boldsymbol{N}}$) of all species over time at constant number of particles ($\boldsymbol{N}$), box size ($\boldsymbol{V}$) and energy ($\boldsymbol{E}$) conditions, i.e., microcanonical ensemble at sufficiently long times for an ergodic system. This method allows time-dependent phenomena to be studied.

$$\mathbf{F}_i = \mathrm{m}_i \frac{\mathrm{d}^2 \mathbf{r}_i(t)}{\mathrm{dt}^2} \tag{2.5}$$

where $\mathbf{r}_i(t)$ is the position vector of ith particle and $\mathbf{F}_i$ is the force acting upon the ith particle of mass m_i at time t due to the interactions with the other particles. The force acting on ith particle is determined by the gradient of the potential energy U in equation (2.6) with respect to the particle positions:

$$\mathbf{F}_i(\mathbf{r}_\mathrm{N}) = -\nabla_i U(\mathbf{r}_\mathrm{N}) = -\left(\frac{\partial U}{\partial \mathrm{x}_i}, \frac{\partial U}{\partial \mathrm{y}_i}, \frac{\partial U}{\partial \mathrm{z}_i}\right) \tag{2.6}$$

Once the potential energy is evaluated, the equations of motion are used to update the position $\mathbf{r}_\mathrm{i}(t)$ and velocity $\mathbf{v}_\mathrm{i}(t)$ of each particle. The trajectories describing the time evolution of the system in phase space are defined by both position and velocity vectors. One of the important properties of the equations of motion is that they conserve the Hamiltonian (2.2), and therefore the total energy of the system is conserved (2.7). Hence, an MD simulation describes an NVE ensemble. Another important property is time reversibility, i.e., time reversal symmetry. The microscopic physics take the same form regardless of the of the direction of time.

$$\frac{d\mathcal{H}}{dt} = \sum_{i=1}^{N} \left[\frac{\partial \mathcal{H}}{\partial \mathbf{r}_i}\frac{\partial \mathbf{r}_i}{\partial \mathrm{t}} + \frac{\partial \mathcal{H}}{\partial \mathbf{p}_i}\frac{\partial \mathbf{p}_i}{\partial \mathrm{t}}\right] \tag{2.7}$$

$$= \sum_{i=1}^{N} \left[\nabla_i U(\mathbf{r}_N)\mathbf{v}_i + \frac{\mathbf{p}_i}{m_i}\mathbf{F}_i \right] = \sum_{i=1}^{N} [-\mathbf{F}_i\mathbf{v}_i + \mathbf{v}_i\mathbf{F}_i] = 0$$

The steps involved in MD simulations are as follows:

i. **Initialisation**: The number of atoms $\boldsymbol{N}$ is defined. The initial position $\mathbf{r}^{\boldsymbol{N}}(t = 0)$ and momentum $\mathbf{p}^{\boldsymbol{N}}(t = 0)$ of each particles are assigned.

ii. **Force calculations**: The forces acting on each particle i are calculated from the derivative of the potential energy, $\mathbf{F}_{\boldsymbol{i}}(\mathrm{t}) = \frac{d\mathbf{p}_{\boldsymbol{i}}}{dt} = -\nabla_{\mathrm{r}_i} U\left(\mathbf{r}^{\boldsymbol{N}}(t)\right)$ due to every particle j within its range of interaction at time, t.

iii. **Integration**: Newton's equations of motion are integrated using one of the finite-difference algorithms (e.g., Verlet algorithm) of different precisions to obtain new positions, $\mathbf{r}^{\boldsymbol{N}}(t + \delta t)$ and momenta, $\mathbf{p}^{\boldsymbol{N}}(t + \delta t)$. Repeat step ii until system properties no longer change with time.

iv. **Data analysis**: Calculate instantaneous properties of interest and take averages of the properties of interest over certain time intervals.

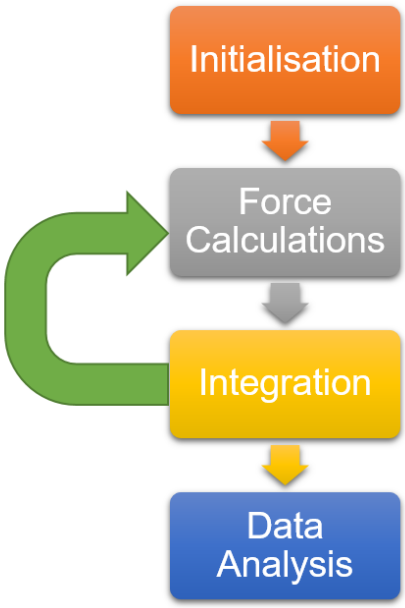

Figure 2.1: Basic workflow of a typical MD simulation.

MD simulations can be used to observe the dynamic evolution of a system in equilibrium or non-equilibrium state. Equilibrium molecular dynamics (EMD) simulations have been successfully employed to predict the thermodynamic and structural properties of systems from their equilibrium trajectories. At equilibrium, the system may still undergo fluctuations with time, but the time averages of thermodynamic properties should no longer change substantially with simulation time. In non-equilibrium molecular dynamics (NEMD) simulations, the system is driven away from thermodynamic equilibrium state, e.g., by imposing a temperature or concentration gradient. NEMD has become popular for its effectiveness in computing the transport flux as well as studying crystal growth in steady state. Like an equilibrium system, systems in steady state do not display net macroscopic change over time. However, a constant input of energy is required to maintain the system at steady state. The time evolution of a system is observed using different ensemble, e.g., microcanonical (NVE), canonical (NVT), isobaric and isothermal (NPT), and grand canonical (μVT) ensembles. Our work focused on canonical ensemble (NVT) and isobaric–isothermal ensemble (NPT). Both ensembles require maintaining the temperature and/or pressure of the system which are handled by thermostats and barostats, respectively. Typically, added dynamical variables which are coupled to the velocity of the atoms are used for thermostating whereas barostatting is achieved by altering the box volume. Examples such as Nosé–Hoover thermostat, Berendsen barostat and thermostat, Andersen thermostat and Parrinello–Rahman barostats are commonly used in simulations for maintaining the temperature and the pressure.

2.3.1 Integration Method

To solve the Newton's equations of motion numerically, one has to choose an appropriate integration algorithm that fulfil the following criteria:

(i) Accurate for large time steps

(ii) Time reversible – An important property of the classical equations of motion

(iii) Symplectic – Conserver energy and the area/volume of the phase space

There are various finite-difference approaches for integrating Newton's equations of motion, e.g., Verlet,[46] Leap-frog,[47] Velocity Verlet,[48] and Gear predictor–corrector,[49] in which the trajectory of all atoms are calculated over discrete (small) time steps, Δt. These methods are constructed so that the linear symplectic structure of phase space is preserved. Furthermore, they also offer advantages such as long-term conservation of energy and good approximation on the conservation of integrals of motion.

2.3.1.1 Verlet Algorithm

A Taylor series of the position of atom i forward in time, i.e., $t + \Delta t$, is as follows:

$$\mathbf{r}_i(t + \Delta t) = \mathbf{r}_i(t) + \dot{\mathbf{r}}_i(t)\Delta t + \frac{1}{2!}\ddot{\mathbf{r}}_i(t)\Delta t^2 + \frac{1}{3!}\dddot{\mathbf{r}}_i(t)\Delta t^3 + O(\Delta t^4) \qquad (2.8)$$

where $\dot{\mathbf{r}}_i(t) = \frac{d\mathbf{r}_i(t)}{dt} = \mathbf{v}_i(t)$ and $\ddot{\mathbf{r}}_i(t) = \frac{d^2\mathbf{r}_i(t)}{dt^2} = \mathbf{a}_i(t)$ are velocity and acceleration of particle i. Similarly, a Taylor expansion of the position of particle i backward in time can be written as:

$$\mathbf{r}_i(t - \Delta t) = \mathbf{r}_i(t) - \dot{\mathbf{r}}_i(t)\Delta t + \frac{1}{2!}\ddot{\mathbf{r}}_i(t)\Delta t^2 - \frac{1}{3!}\dddot{\mathbf{r}}_i(t)\Delta t^3 + O(\Delta t^4) \qquad (2.9)$$

Summing and rearranging equation (2.8) and equation (2.9) gives rise to an equation which is independent of velocity as:

$$\mathbf{r}_i(t + \Delta t) = 2\mathbf{r}_i(t) - \mathbf{r}_i(t - \Delta t) + \ddot{\mathbf{r}}_i(t)\Delta t^2 + O(\Delta t^4) \qquad (2.10)$$

Using Newton's equation, $\mathbf{F}_i = m_i\ddot{\mathbf{r}}_i(t)$, equation (2.10) can be rewritten as:

$$\mathbf{r}_i(t + \Delta t) \approx 2\mathbf{r}_i(t) - \mathbf{r}_i(t - \Delta t) + \frac{\mathbf{F}_i(t)}{m_i}\Delta t^2 \qquad (2.11)$$

Given previous position $\mathbf{r}_i(t - \Delta t)$, the current position $\mathbf{r}_i(t)$ and the current force $\mathbf{F}_i(t)$ (computed from $U\left(\mathbf{r}^N(t)\right)$, the new position can be determined using equation (2.11). The velocity of the particles can be approximated by equation (2.12).

$$\mathbf{v}_i(t) \approx \frac{\mathbf{r}_i(t+\Delta t) - \mathbf{r}_i(t-\Delta t)}{2\Delta t} \tag{2.12}$$

The disadvantages of the Verlet algorithm include:

i. It requires two sets of positions, at $\mathbf{r}_i(t-\Delta t)$ and $\mathbf{r}_i(t)$, to start a simulation.

ii. It does not keep track of velocities.

iii. Issues with precision unless the time step used is small.

2.3.1.2 Leap-Frog Algorithm

In this work, the Leap-Frog algorithm (a variant of Verlet) was used to solve Newton's equations of motions.

$$\mathbf{v}_i\left(t+\frac{1}{2}\Delta t\right) = \mathbf{v}_i\left(t-\frac{1}{2}\Delta t\right) + \ddot{\mathbf{r}}_i(t)\Delta t \tag{2.13}$$

$$\mathbf{r}_i(t+\Delta t) = \mathbf{r}_i(t) + \mathbf{v}_i\left(t+\frac{1}{2}\Delta t\right)\Delta t \tag{2.14}$$

In this algorithm, equation (2.13) is first executed to obtain the mid-step velocity at $t + \frac{1}{2}\Delta t$, utilising the stored values of current position $\mathbf{r}_i(t)$, acceleration $\ddot{\mathbf{r}}_i(t)$ and mid-step velocity $\mathbf{v}_i\left(t-\frac{1}{2}\Delta t\right)$ of particle i. The velocities first leap over the particle positions which then subsequently leap over to give rise to the next mid-step velocities of particles. Finally, the velocity of particle i at time t can then be approximated by averaging their mid-step velocities at $t+\frac{1}{2}\Delta t$ and $t-\frac{1}{2}\Delta t$ using the following equation:

$$\mathbf{v}_i(t) \approx \frac{1}{2}\left[\mathbf{v}_i\left(t+\frac{1}{2}\Delta t\right) + \mathbf{v}_i\left(t-\frac{1}{2}\Delta t\right)\right] \tag{2.15}$$

The advantage of this algorithm is that it is more precise than the Verlet algorithm and the particle velocities are explicitly; However, the disadvantage is that particle velocities and the positions calculated are not of the same time. Both the Leap-Frog and Verlet algorithms are time reversible and phase space volume preserving. However, they do not conserve the total energy of the system, the long-term energy drift should not be very significant provided a small timestep Δt is used.

2.3.2 Constraint Algorithm

In order to satisfy Newtonian motion for molecules with various mass points, many holonomic constraints have been proposed to enforce bond lengths and angles within the molecules. Therefore, a larger time step can be used, when high-frequency vibrational motions/oscillations are not important for the phenomenon being studied. In constraint dynamics, the Newton's equations of motion are coupled with holonomic constraints on the positions of the atoms. The SHAKE algorithm[50] is a direct modification of the Verlet Algorithm by imposing constraints on the bond lengths and angles through fixed interparticle distances r_{ij}. It simply resets all bond lengths to set values until all constraints are satisfied within a relative tolerance and is numerically stable for large molecules. Another method is LINCS algorithm,[51] a non-iterative two-step approach, where the projections of the new bonds on the old bonds are first set to zero, and then subsequently a matrix correction that prevents bond stretching due to rotation is implemented. The speed improvement of LINCS is about three- to four-fold faster than that of the SHAKE algorithm with the same accuracy. For the particular case of rigid water models, e.g., SCP and TIP4P water models, SETTLE[52] is a fast algorithm which resets the positions and velocities of water molecules to satisfy the holonomic constraints.

2.3.3 Thermostat

Solving Newton's equations of motion allows us to study the time evolution of a molecular system described by an NVE ensemble, where the total system energy is conserved but not its potential and kinetic energy. Whilst this allows the system to attain equilibrium eventually, its temperature changes. Therefore, it is appropriate to require a means to modulate system temperature. Furthermore, it is also useful to conduct MD simulations at constant temperature, such as those offered in NVT or NPT ensemble, as this closely mimic real experiments, something we have control of in real life. This can be achieved implementing a thermostat, which modifies the equations of motion (2.5) with added stochastic or deterministic terms. The temperature of a simulated system is typically

computed from the kinetic energy of the system using the equipartition theorem defined by equation (2.16):

$$\frac{3}{2}Nk_bT = \langle \sum_{i=1}^{N} \frac{1}{2} \mathrm{m}_i \mathbf{v}_i^2 \rangle \tag{2.16}$$

where k_b is Boltzmann's constant, m_i and $\mathbf{v}_i$ are the mass and velocity of atom i, respectively, and N is the total number of atoms in the system. The angle brackets imply that the system temperature T is a time-averaged quantity. Besides that, equation (2.16) can also be used to calculate the instantaneous temperature at time t. The instantaneous temperature will first drift, however, upon reaching equilibrium, it will fluctuate around the target temperature T_0.

In our study, the deterministic methods were used to maintain a constant temperature over the course of MD simulations. One of the most accessible implementations is the so-called 'simple' velocity rescaling thermostat,[53] which simply rescales all the atomic velocities by a factor of $\sqrt{\frac{T_0}{T}}$ to drive the current kinetic temperature T to the desired temperature T_0. However, this basic thermostat has been shown that the simple velocity rescaling thermostat does not properly sample the kinetic energy distribution.[54] This algorithm was found to introduce yield artificial effects in the dynamic, energetic, and structural properties of the system, so it is not recommended for production MD runs.[55] A similar approach was introduced by Berendsen et al.[56] to include a weak coupling of the system to an external thermal bath of temperature T_0. The Berendsen algorithm corrects slowly the deviation of system temperature T towards the desired temperature T_0 according to equation (2.17).

$$\frac{dT}{dt} = \frac{T_0 - T}{\tau_T} \tag{2.17}$$

where τ_T is the thermostat coupling constant during which the temperature deviation decays exponentially. Although the Berendsen thermostat is quite efficient in relaxing the

system to the desired temperature T_0, it does not sample the canonical or the isokinetic distribution. In practice, it is recommended to use the Berendsen thermostat with a small coupling constant during MD initialisation runs to equilibrate the system whilst allowing the system to attain the desired temperature.

During production MD runs, it is recommended to use a thermostat that samples the correct canonical ensemble, i.e., Nosé–Hoover thermostat, first developed by Nosé[57] and then further improved by Hoover.[58] The Nosé–Hoover thermostat works by introducing a friction parameter through which the motion of particles is controlled until the system temperature T approaches the desired value T_0. The modified global equations of motion are expressed in equation (2.18), with the strength of the coupling depending on the constant Q, the 'thermal inertia' of the heat bath.

$$\frac{d^2\mathbf{r}(t)}{dt^2} = \frac{\mathbf{F}}{\mathrm{m}} - \frac{p_\xi}{Q}\frac{d\mathbf{r}}{dt} \tag{2.18}$$

where $\mathbf{r} \equiv \{\mathbf{r}_i\}$, $\frac{\mathbf{F}}{\mathrm{m}} \equiv \sum_i \frac{\mathbf{F}_i}{\mathrm{m}_i}$, etc. The friction coefficient $\frac{p_\xi}{Q} \equiv \xi$ is a dynamic quantity, where the equation of motion of the heat bath parameter ξ is:

$$\frac{dp_\xi}{dt} = T - T_0 \tag{2.19}$$

Unlike the Berendsen thermostat, the Nosé–Hoover thermostat takes longer to relax the system towards the target value T_0. Switching to the Nosé–Hoover thermostat for production is preferable as the simulated system reaches equilibrium and allows correct NVT sampling.

2.3.4 Barostat

System pressure is often computed using the *virial*, which is a product of the derivative of the potential energy function (force) and the interparticle distance r_{ij}. The latter changes rapidly throughout the simulation, resulting in huge fluctuations in system pressure, even more so than quantity like temperature T and energy E in NVT and NVE ensemble,

respectively. Likewise, it is also helpful to control the pressure of a simulated system to mimic real-world experiments by coupling it to a *pressure* bath (analogous to that of a thermal bath) to impose a volume change of the simulation box. To achieve this, a barostat (algorithm) can be used to scale the system coordinates or modify Newton's equations of motion. There exist several barostats, such as Andersen,[59] Berendsen,[56] Nosé–Hoover,[60,61] and Parrinello–Rahman.[62] This thesis used both the Berendsen and Parrinello–Rahman barostats to control the pressure. The former was used in equilibration runs for quick relaxation of the system towards a specified value, whereas the latter was used in the subsequent production runs to enforce NPT ensemble, along with a Nosé–Hoover thermostat for temperature control. The Berendsen barostat maintains the pressure by coupling the system to a weakly interacting pressure bath, allowing scaling of the system volume so that the instantaneous pressure P approaches the target P_0 according to equation (2.20):

$$\frac{dP}{dt} = \frac{P_0 - P}{\tau_P} \tag{2.20}$$

Similarly, a relaxation time constant pertaining to the barostat τ_P exists during which the scaling of the system volume occurs. Even though the average pressure $\langle P \rangle$ generated by the Berendsen yields the target value, it does not sample the NPT ensemble. The Parrinello–Rahman barostat works by scaling the size and shape of the simulation box whilst producing the correct NPT ensemble. In addition, it can also be used to apply external anisotropic stress to parts of the system. The modified equations of motion is similar to that of equation (2.18) for Nosé–Hoover thermostat, where instead of a friction coefficient ξ related to a heat bath, a fictitious friction parameter M related to the external stress from a pressure bath acting upon a simulation box causing changes in lattice parameters [a, b, c, α, β, γ] is added.

$$\frac{d^2\mathbf{r}(t)}{dt^2} = \frac{\mathbf{F}}{\mathrm{m}} - \boldsymbol{M}\frac{d\mathbf{r}}{dt} \tag{2.21}$$

2.4 Monte Carlo Methods

Monte Carlo (MC), developed by von Neumann, Ulam, and Metropolis in the 1940s, is another molecular simulation technique based on probabilistic approach and is stochastic in nature (unlike MD), where the trajectory of the system evolves randomly to sample phase space. In general, the algorithm of MC is relatively simple compared to MD, a basic MC move involves the following:

1. Random selection of a particle (out of N particles) and perform a potential energy evaluation of the system at initial configuration, U_1.
2. Random displacement of the particle and evaluate the new energy of the system at a new configuration, U_2.
3. Compute the change in potential energy due to particle displacement $\Delta U = U_2 - U_1$.
4. Accept/reject the movement of the particle based on acceptance criteria.
    - If $\Delta U < 0$, accept the configuration as new state.
    - If $\Delta U > 0$, compute acceptance probability, $P^{acc} = \exp(-\Delta U/k_B T)$, and accept if $P^{acc} >$ rand[0,1], reject otherwise.
5. If the movement is accepted, the new configuration will be used as the next state. If the move is rejected, the original configuration will be used again as the next state.
6. Repeat many times and accumulate averages.

This Thesis focuses on using Grand Canonical Monte Carlo (GCMC) to predict the amount of CH_4 adsorbed in micropores of kerogens. In GCMC simulations, the chemical potential (μ), volume (V) and temperature (T) are kept constant. The number of particles N can fluctuate so that the chemical potential in the bulk and adsorbed phase are equal. This ensemble allows us to study the adsorption equilibrium of an adsorbate–adsorbent system, given the pressure or fugacity. It can be used to discover adsorbent materials with high separation efficiency for a given fluid mixture. To understand the statistical mechanics basis for the GCMC, we must first understand the partition function of the NVT ensemble.

2.4.1 Canonical Monte Carlo

The probability density for the canonical ensemble is proportional to

$$\exp[-\mathcal{H}(\mathbf{r},\mathbf{p})/k_B T] \tag{2.22}$$

and the partition function is

$$\mathcal{Q}_{NVT} = \sum \exp(-\beta \mathcal{H}(\mathbf{r},\mathbf{p})) \tag{2.23}$$

where $\beta = 1/k_B T$. For an atomic system, it can be written as

$$\mathcal{Q}_{NVT} = \frac{1}{N!}\frac{1}{h^{3N}} \int \ldots \int \exp[-\beta \mathcal{H}(\mathbf{r},\mathbf{p})]\ d\mathbf{r}\, d\mathbf{p} \tag{2.24}$$

By treating the Hamiltonian into an ideal gas (kinetic contribution) and a residual (configurational contribution) part

$$\mathcal{Q}_{NVT} = \frac{1}{N!}\frac{1}{h^{3N}} \int \ldots \int \exp[-\beta U(\mathbf{r})]\, d\mathbf{r} \int \ldots \int \exp[-\beta \mathcal{K}(\mathbf{p})]\, d\mathbf{p} \tag{2.25}$$

In the case of an ideal gas, where $U = 0$, $\mathcal{Q}_{NVT}^{ideal}$ can be expressed as

$$\mathcal{Q}_{NVT}^{ideal} = \frac{1}{N!}\frac{V^N}{\Lambda^{3N}} \tag{2.26}$$

with Λ being the thermal de Broglie wavelength

$$\Lambda = (h^2/2\pi m k_B T)^{1/2} \tag{2.27}$$

The residual part is simply

$$\mathcal{Q}_{NVT}^{residual} = V^{-N} \int \ldots \int \exp[-\beta U(\mathbf{r})]\, d\mathbf{r} \tag{2.28}$$

The residual part pertains to real gases, in which interatomic interactions are present, unlike in an ideal gas, which are considered negligible. The partition function can be written as

$$\mathcal{Q}_{NVT} = \mathcal{Q}_{NVT}^{ideal} \frac{Z}{V^N} \tag{2.29}$$

where Z is the configurational integral

$$Z = \int \dots \int \exp[-\beta U(\mathbf{r},)]\, d\mathbf{r} \tag{2.30}$$

The average of some property $\mathcal{A}$ in NVT ensemble is given by equation (2.31):

$$\langle \mathcal{A} \rangle_{NVT} = \frac{\int \mathcal{A} \exp(-\beta U(\mathbf{r})) d\mathbf{r}}{\int \exp(-\beta U(\mathbf{r})) d\mathbf{r}} \tag{2.31}$$

2.4.2 Grand Canonical Monte Carlo

The probability density for the grand canonical ensemble is proportional to

$$\exp[-\beta(\mathcal{H}(\mathbf{r},\mathbf{p}) - \mu N)] \tag{2.32}$$

and its partition function is

$$\mathcal{Q}_{\mu VT} = \sum_N \exp(\beta \mu N)\, \mathcal{Q}_{NVT} \tag{2.33}$$

For an atomic system, it can be written as

$$\mathcal{Q}_{\mu VT} = \sum_N \frac{1}{N!} \frac{1}{h^{3N}} \exp(\beta \mu N) \int \exp(-\beta \mathcal{H}(\mathbf{r},\mathbf{p}))\, d\mathbf{r}\, d\mathbf{p} \tag{2.34}$$

Or in scaled coordinates, $\mathbf{s} = L^{-1}\mathbf{r}$ and assuming a cubical simulation box where $L = V^{-1/3}$

$$\mathcal{Q}_{\mu VT} = \sum_N \frac{\exp(\beta \mu N)\, V^N}{N!\ \Lambda^{3N}} \int \exp(-\beta U(\mathbf{s}))\, d\mathbf{s} \tag{2.35}$$

Finally, the chemical potential of an ideal gas, μ can be expressed as

$$\mu = k_B T \ln\left(\frac{\Lambda^3 N}{V}\right) \tag{2.36}$$

Now that the core equations for the grand canonical ensemble have been represented in GCMC simulations, the following moves will be sampled according to the acceptance probability:

a) Particle displacement

$$P^{acc}(\mathbf{s} \to \mathbf{s}') = \min\{1, \exp[-\beta(U(\mathbf{s}'^N) - U(\mathbf{s}^N))]\} \tag{2.37}$$

b) Particle insertion

$$P^{acc}(N \to N+1) = \min\left\{1, \frac{V}{\Lambda^3(N+1)} \exp[\beta(\mu - U(\mathbf{s}^{N+1}) + U(\mathbf{s}^N))]\right\} \tag{2.38}$$

c) Particle deletion

$$P^{acc}(N \to N-1) = \min\left\{1, \frac{\Lambda^3 N}{\mathrm{V}} \exp[-\beta(\mu + U(\mathbf{s}^{N-1}) - U(\mathbf{s}^N))]\right\} \tag{2.39}$$

The average of some property $\mathcal{A}$ in GCMC is given by equation (2.40):

$$\langle \mathcal{A} \rangle_{\mu VT} = \frac{\sum_{N=0}^{\infty} (N!)^{-1} V^N z^N \int \mathcal{A}(\mathbf{s}) \exp(-\beta U(\mathbf{s}))\, d\mathbf{s}}{\mathcal{Q}_{\mu VT}} \tag{2.40}$$

2.5 Energy and Force Calculations

Many shortcuts were invented to reduce the computational effort in calculating molecular interactions. The number of particles in a simulation box N is minimal compared to the macroscopic limit. It is computationally infeasible to simulate bulk matter containing at least ~10^{23} particles. In MD simulations, the positions and momenta of every atom must be updated by re-evaluating the forces acting upon the atoms at every timestep. In both MC and MD simulations, the potential energy calculation primarily involves a summation of all nonbonded pair interactions, consisting of the van der Waal and electrostatic

interactions, costing tremendous computational time. One of the workarounds is to define a cutoff distance to deal with the limited computer memory and speed. Such an approach, called the Cutoff Method (CM) ignores nonbonded interactions between atoms separated by a distance greater than a specified cutoff value. This treatment works well for the van der Waal interactions; however, it does not apply to the long-range nature of electrostatic interactions of charged atoms. Many efficient techniques have been developed to treat electrostatic interactions by separating the electrostatic interactions into a long-range and short-range component at a given cutoff distance. Such a method computes the rapid changing short-range electrostatic interactions in real space. In contrast, the slow decaying potential over long-range is computed in reciprocal space using different approaches, e.g., Ewald summation,[63] Particle Mesh Ewald (PME),[64] and Particle-Particle Particle-Mesh methods (PPPM).[47] These methods significantly improve the efficiency of computing long-range electrostatic interactions. We employed the PME algorithm in our simulations to account for the long-range electrostatic interactions. Point charges are interpolated onto a grid and then transformed through a fast Fourier transformation (FFT) algorithm. Finally, the reciprocal energy can then be obtained via a single sum over the grid in k-space. By using the interpolation factor, forces acting on each atom can be obtained after the inverse transformation of the potential at the grid points.

2.6 Periodic Boundary Condition

Simulating a finite number of particles representing bulk matter is very far from the thermodynamic limit. It can cause a finite size effect, which dramatically affects the computed thermodynamic properties of interest. Periodic Boundary Conditions (PBC) is commonly used to minimise the boundary/surface effects, where the simulation box is imagined to be surrounded on all sides by exact replicas of itself, extending to infinity such that the particles in the simulation box experience the forces in the same way as they would do in an infinite system. When a particle leaves the box on one wall, its image, having the same momenta, enters the box at the opposite face. There are no walls at the boundary of the simulation box, thus avoiding the surface effects. However, the number of pairwise

interactions will also increase due to the presence of periodic images. As such, the minimum image convention is applied so that every particle could only interact with a single “image” of every other particle. A cutoff radius is used to truncate the interactions such that only the interactions within the cutoff radius will be considered.

Chapter 3 Does Confinement Enable Methane Hydrate Growth at Low Pressures? Insights from Molecular Dynamics Simulations

The material presented in this Chapter was published in 2020 in Volume 124, Issue 20, Pages 11015–11022 of The Journal of Physical Chemistry C. Available online via: https://doi.org/10.1021/acs.jpcc.0c02246.

3.1 Introduction

Gas hydrates, also known as clathrate hydrates, are a subset of nonstoichiometric crystalline inclusion compounds, which are formed when the self-assembly of water molecules into 3D hydrogen-bonded framework of cavities enclathrate small gas molecules. The ideal conditions for gas hydrate formation are usually at low temperatures (< 300 K) and high pressures (> 6 bar), and their structure is stabilised by van der Waals forces. To date more than 130 molecules (or hydrate formers) have been identified that form gas hydrates.[1] There are three common crystalline structures of gas hydrates, namely, structure I (sI), structure II (sII) and structure H (sH). The type of structure they adopt is determined by a range of factors, i.e., formation conditions and the type and the size of the guest molecules they hold enclathrated. One of the key properties of gas hydrates is their extraordinary gas storage capacity. At full occupancy (i.e., all cages fully occupied), 1 m^3 of sI gas hydrates can store up to 173 m^3 (STP) of gas.[10]

In the last few decades there has been a surge of interest in gas hydrate research due to their relevance in flow assurance,[5,65] global warming,[66–68] and marine geohazards[69,70]. Gas hydrate-based technologies have been proposed in various fields, including but not limited to, gas mixture separation,[71] energy recovery,[72] and gas storage and transportation[73]. The biggest challenges in exploiting gas hydrate-based technologies are the slow formation and dissociation kinetics and poor understanding of the formation and dissociation mechanisms of gas hydrates. There is a considerable amount of literature on gas hydrate formation and

dissociation in the bulk phase, with or without the presence of impurities, such as hydrate promoters and inhibitors, via experiments[74–80] and molecular simulations.[81–89] Consequently, the phase equilibria and other thermophysical properties of bulk gas hydrates are well established. On the other hand, the nature of hydrate formation and dissociation in confined nanospace, which is of crucial relevance to the understanding of the appearance of natural gas hydrates in complex porous environments, is a matter of ongoing scientific discussion.

Methane hydrates are the most abundant form of gas hydrates and typically found naturally in permafrost regions and marine sediments. Estimates suggest that the amount of energy stored as natural methane hydrates, although limited, is at least twice of that of all other hydrocarbon-based fuels combined, making it the largest source of unexploited fuel.[4,5] They are of cubic sI crystal type, where each unit cell is comprised of two "small" dodecahedron cages (denoted as 5^{12}) and six "large" tetrakaidecahedron cages (denoted as $5^{12}6^2$), with coordination numbers of 20 and 24, respectively. An average cavity radius of 3.95 and 4.33 Å for the small and large cages, respectively, is sufficient to accommodate a methane molecule per cage. Hence, a nominal stoichiometry of $1CH_4{:}5.75H_2O$ is obtained for methane hydrates at full occupancy.

Recent studies have focused on the provision of solid surfaces in gas hydrate studies, both experimentally and computationally. An improved understanding of methane hydrate formation in confinement is essential for a wide range of scientific and industrial purposes, especially in the advancement of hydrate-based technologies. To date, there has been little agreement about the precise nature of confinement effects. Some studies[90,91] suggested that the effect of inhibition is stronger than that of promotion in confined space due to reduced water activity. However, the promoting or inhibiting effects of porous materials are still largely unknown owing to experimental challenges associated with quantifying hydrate formation, which comprises of nucleation and growth, in such systems where the length and time scales involved are often inaccessible experimentally. To address this, together

with experimental studies, researchers have also employed computational approaches, such as molecular dynamics (MD) and Monte Carlo (MC) simulations to study gas hydrate systems.

Cha et al.[92] found that methane hydrate formation is promoted in the presence of bentonite, for which they suggested that the clay mineral surface could act as a nucleation site by forming an ordered layer of adsorbed water on the surface. Conversely, Handa and Stupin[93] reported thermodynamic inhibition of confined methane and propane hydrates in silica gel of average pore diameter of 15 nm as a result of reduced water activity. Similar observations can also be noted in the work of Uchida et al.,[94] using porous glasses with a pore size distribution ranging from 10 to 50 nm. Several studies[95–97] have utilised molecular simulations to study the promoting effects of Na-montmorillonite on methane hydrate formation, they showed that clathrate-like water structures enclosing methane molecules near the clay surfaces could stabilise confined methane hydrates. One study by Bai et al.[98] reported the nucleation mechanism of carbon dioxide hydrates in the presence of hydroxylated silica surfaces, which is a three-stage process; ice-like structures trigger the formation of intermediate hydrate structures that subsequently act as nucleation seeds for hydrate growth. Moreover, they also demonstrated that the pore size has little effect on the formation mechanisms except for narrow pores where no carbon dioxide hydrate can be formed due to steric constraints. In an MC study set out to study the effects of confinement on CH_4 hydrate dissociation, Chakraborty and Gelb[99] placed CH_4 hydrate crystals of various sizes (up to two unit cells thick) in the *z*-direction (perpendicular to the wall), thus varying the pore width of carbon-like slit pores. Furthermore, they have also examined the effect of different water models on hydrate dissociation mechanisms. They noted SPC/E hydrates are relatively less stable than hydrates of TIP4P variants. There was no clear dependency of pore size on hydrate stability for SPC/E hydrate, whereas the stability of TIP4P-type hydrates can be predicted by Gibbs–Thomson equation. Bagherzadeh et al.[100,101] conducted MD simulations with rigid silica surfaces and demonstrated that confinement affects the interfacial curvature of confined fluids as well as their distribution. Surprisingly, faster

dissociation rates were observed in confined systems and for systems without a buffer water layer adjacent to the silica surface. The latter finding suggests that the surfaces destabilise the hydrate phase such that there exists a layer of disordered water close to the surfaces, and hydrate formation does not occur from the surfaces, supporting the observations made by Chakraborty and Gelb.[99] Based on the same surface structure of silica, Liang et al.[102,103] identified methane hydrate growth progresses preferentially towards the bulk solution and the surfaces can act as a reservoir of methane molecules. In addition, they also noticed the formation of incomplete cages near the surfaces that could initiate methane hydrate nucleation. In an analysis of methane hydrate formation in clays of different pore sizes, Yan et al.[104] noted that the surface water exhibits certain cage-like structures. The presence of intercalated cations causes distortions and defects of intercalated methane hydrates due to disruptions in hydrogen bonding. In a study comparing hydrophilic and hydrophobic surfaces, Nguyen et al.[105] found that the latter enhances local gas density as well as promotes structural ordering of water near the solid surface, which consequently aids gas hydrate formation. While most studies utilising solid surfaces treated them as rigid and non-flexible structures, He et al.[106] explored the use of flexible structures of graphite and silica surfaces to study methane hydrate formation with various initial configurations of methane nanobubble in slit-shaped nanopores. They demonstrated that methane nanobubble of negative curvature (concave-shaped) adsorbed on the hydrophobic graphite surface results in a lower Young–Laplace pressure at the fluid interface, which effectively lowers the bulk methane concentration, and hence no observable methane hydrate formation. On the other hand, the hydroxylated silica surface promotes the formation of a convex-shaped methane nanobubble, which consequently results in methane hydrate formation. Furthermore, they also showed that, in a homogenised solution, methane hydrate preferentially forms in the bulk, away from the surfaces regardless of the hydrophobicity of the surfaces. Overall, these studies highlight the complexity of studying gas hydrate formation in porous media.

Recent experimental studies by Silvestre-Albero and co-workers suggest that porous materials can promote methane hydrate formation at conditions milder than that of required in the bulk, thanks to the confinement effects.[13–17] They found that wet activated carbon, which contains well defined slit pores, modifies methane adsorption isotherms, such that, methane adsorption is greatly enhanced compared to that of dry samples. Through synchrotron X-ray powder diffraction, they further confirmed methane hydrate formation took place in confined nanospace, and that the storage capacity increases with increasing pore size up to an optimum size of 25 nm.

As mentioned above, there have been a number of studies that investigated methane hydrate growth in confinement by employing molecular simulations. However, these studies were carried out at temperatures and pressures that hydrate growth is certain in the bulk; i.e, either very high pressure or very low temperature.[98,102–104,107] Therefore, so far it has not been possible to confirm whether confinement effects can facilitate methane hydrate growth at milder conditions compared to the bulk. For instance, the work of He et al.[106] shows that while methane hydrate growth takes place in hydroxylated silica slit pores no growth is observed in graphene slit pores. Although their work provides valuable insights about the effect of surface chemistry, it cannot show whether confinement promotes methane hydrate growth, because their simulations were carried out at 400 bar at which methane hydrate growth occurs in the bulk phase, i.e., without the effect of confinement.

In order to answer whether confinement effects can facilitate methane hydrate growth at milder conditions compared to the bulk, we carried out a systematic study by performing molecular dynamics simulations of methane water systems in the bulk and in hydroxylated silica pores at various pressures. Our study shows that, indeed, methane hydrate growth can take place in narrow pores at pressures lower than that of required for bulk methane hydrates.

3.2 Methodology

The direct phase coexistence methodology developed by Ladd and Woodcock[108] has been shown to predict the phase equilibria of gas hydrate systems in the bulk successfully.[109–115] In this method a three-phase configuration consisting of hydrate crystal, liquid water and vapour slabs co-exist. We used this method to study gas hydrate systems in confinement.

3.2.1 Water, Methane and Hydroxylated Silica Interaction Potentials

Most methane hydrate simulations reported in the literature have employed united-atom models for the methane molecules (Table 3.1) and 4-site, rigid, non-polarisable models for the water molecules (Table 3.2). This combination provides simplicity and speeds up the simulations. Furthermore, this approach has been shown to successfully reproduce the formation of methane hydrates in the bulk.[88,109,111]

Table 3.1: Summary of methane models used in methane hydrate simulations.

Methane Model	**References**
United Atom (single LJ site, TraPPE, OPLS-UA, etc.)	Chakraborty and Gelb,[99] Bagherzadeh et al.,[100,101] Conde and Vega,[109] Docherty et al.,[116] He et al.,[106] Jin and Coasne,[115] Liang et al.,[102] Liang and Kusalik,[103] Luis et al.,[112] Michalis et al.,[111] Walsh et al.,[85,88,89] Zhang et al.[117,118]
All-Atom (AA, OPLS-AA, etc.)	Luis et al.,[119,120] Yan et al.[104,121]

Table 3.2: Summary of water models used in methane hydrate simulations.

Water Model	**References**
mW[122]	Jacobson et al.[123]
SPC[124]	Yan et al.[104]
SPC/E[125]	Bagherzadeh et al.,[100] Chakraborty and Gelb,[99] Luis et al.[120]
TIP4P[126]	Chakraborty and Gelb,[99] Conde and Vega,[109] Luis et al.,[120] Yan et al.[121]
TIP4P/2005[127]	Chakraborty and Gelb,[99] Conde and Vega,[109] Docherty et al.,[116] Jin and Coasne,[115] Liang et al.,[102] Liang and Kusalik,[103] Luis et al.[114]
TIP4P/Ice[128]	Conde and Vega,[109] He et al.,[106] Jin and Coasne,[115] Luis et al.,[114,119] Michalis et al.,[111] Walsh et al.,[85,88,89] Zhang et al.[117,118]
TIP4Q[129]	Luis et al.[119]
TIP5P[130]	Luis et al.[120]

It has been shown that the solubility of guest molecules in water, which is dependent on their cross interactions, is essential to yielding an accurate description of gas hydrate formation.[85,106,109,110,123,131–133] Docherty et al.[116] demonstrated that using modified LB combining rules is an effective way to compensate for the absence of polarisation energies in non-polarisable models (TIP4P/2005 & UA methane) and hence a better estimation of methane solubility in liquid water. Note that in Table 3.3, the crossed interaction energies between methane-water obtained using TIP4P/Ice and TIP4P/2005 are of similar strength, which suggests TIP4P/Ice water model can provide a similar description of methane solubility as the TIP4P/2005 water model. Besides that, Conde and Vega have shown the advantage of the TIP4P/Ice water model, which was developed to reproduce the melting point of hexagonal ice (Ih), at reproducing the three-phase coexistence temperature for methane hydrates with a systematic shift of 3.5 K from experimental results.[109]

Table 3.3: Potential parameters of TraPPE-UA (methane), TIP4P/2005 (water) and TIP4P/Ice (water), and their cross-interaction parameters as obtained from LB rules ($\chi = 1$) and modified LB rules ($\chi = 1.07$) from Docherty et al.[116]

Model	σ **(Å)**	ϵ/k_B **(K)**	q_H (e)	d_{OM} **(Å)**
CH4 (TraPPE-UA)	3.7300	148.0		
TIP4P/2005	3.1589	93.2	0.5564	0.1546
TIP4P/Ice	3.1668	106.1	0.5897	0.1577
TIP4P/Ice-CH4 ($\chi = 1.00$)	3.4484	125.3		
TIP4P/2005-CH_4 ($\chi = 1.00$)	3.4445	117.4		
TIP4P/2005-CH_4 ($\chi = 1.07$)	3.4445	125.7		

Based on the reasons above, in our study, water and methane molecules were represented by the TIP4P/Ice water model, a four-site model with a massless particle for the oxygen charge,[128] and TraPPE United Atom (TraPPE-UA) model,[134] respectively. The hydroxylated silica surfaces were described by a CHARMM-based force field developed by Lopes et al.,[135] which allows flexibility of the silica surfaces.

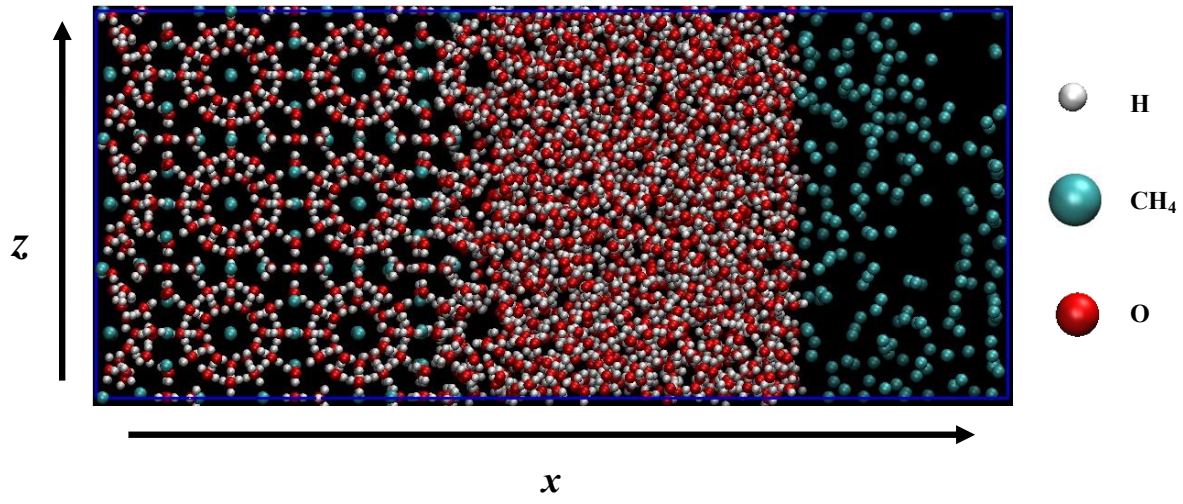

Figure 3.1: Initial configuration of the bulk systems.

3.2.2 Initial Configuration of Bulk Systems

The preparation of the initial configuration of the bulk systems closely follows the procedure set out by Conde and Vega,[109] and can be briefly summarised as follows; to generate the three-phase configuration, we first obtained a single-crystal structure of

methane hydrate determined from XRD measurements as reported by Kirchner et al.[136] While retaining the positions of carbon and oxygen atoms at their crystallographically determined positions, we added hydrogen atoms as well as dummy atoms to the oxygen atoms according to the geometry of TIP4P/Ice model. Hydrogen atoms were not added to the carbons since we used a united atom methane model. The resulting unit cell structure was then replicated to create a supercell containing 3 × 3 × 3 (27) sI methane hydrate unit cells. Finally, three slabs consisting of (i) 3 × 3 × 3 (27) sI methane hydrate unit cells, (ii) 1242 water molecules, and (iii) 216 methane molecules were equilibrated separately, using short *NVT*-MD simulations. The y and z dimensions of the water and methane slabs were kept equal to the hydrate slab (i.e., 3.563 nm × 3.563 nm). Then, they were brought together with a 0.1 nm buffer distance between them. Finally, energy minimisation via steepest descent was carried out to avoid bad contacts. The dimensions of the initial configuration of the bulk systems (Figure 3.1) were approx. 8.409 × 3.563 × 3.563 nm^3.

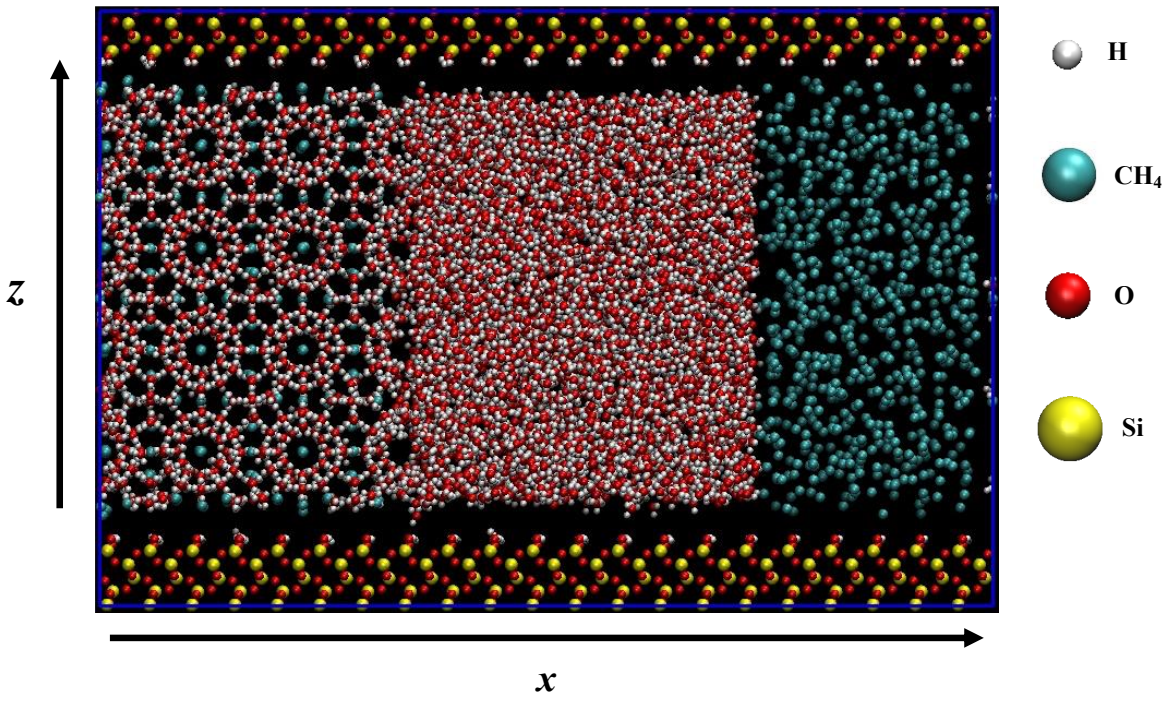

Figure 3.2: Initial configuration of the confined systems.

3.2.3 Initial Configuration of Confined Systems

The initial configuration of the confined systems used in this study consists of a three-phase configuration (i.e., solid hydrate crystal, liquid water and methane gas) placed within a slit-shaped silica nanopore as shown in Figure 3.2. To generate the silica slit pore, a silica block was first created by replicating a unit cell of α-cristobalite unit cell for 21 × 12 × 10 times. Then a portion of the supercell that corresponds to the thickness of four sI methane hydrate unit cells (≈ 4.75 nm) was removed from the centre of the silica block, leaving behind a slit pore. Finally, nonbridging oxygen atoms were subsequently protonated, yielding silanol groups on the surfaces.

The three-phase configuration in the slit pore was created from 7 × 5 × 4 (140) sI methane hydrate unit cells, which consists of 1225 methane molecules and 6650 water molecules. In the crystalline form, this would occupy about 80% of the slit-pore volume shown in Figure 3.2. For the crystal slab, 3 × 5 × 4 (60) sI methane hydrate unit cells were used. The 700 methane and 3845 water molecules in the remaining 4 × 5 × 4 (80) unit cells, were used to create methane and water slabs, respectively, by equilibrating them separately using short *NVT*-MD simulations. The three slabs were then brought together with a 0.1 nm buffer distance between them to create a three-phase configuration. Finally, the three-phase configuration was placed in the slit-shaped pore of hydroxylated silica. In order to avoid bad contacts, energy minimisation via steepest descent was performed. The dimensions of the initial configuration of the confined systems were 10.45 × 5.97 × 6.95 nm^3. A flowchart illustrating the preparation of the initial configurations is provided in Figure A1. Sample input files, including force field parameters and initial configurations, can be obtained online.

3.2.4 Simulation Settings

All MD simulations were performed using GROMACS 2019.4 molecular dynamics simulations software.[137] The leapfrog algorithm with a time-step of 2 fs was used for integrating Newton's equations of motions. Water molecules were held rigid by the

SETTLE algorithm.[52] Periodic boundary conditions were applied in all directions. The short-range non-bonded interactions were modelled with the Lennard-Jones (LJ) potential. The Lorentz–Berthelot combining rules were used to calculate the cross-interaction LJ parameters of unlike atoms. The long-range Columbic interactions were calculated using a smooth Particle Mesh Ewald (PME) method of fourth order polynomial with a mesh width of 0.12 nm.[138] A cutoff distance of 11 Å were used for the LJ interactions and the real part of the Ewald sum. For both energy and pressure, no long-range dispersion corrections (a.k.a. tail corrections) applied. The simulation temperature was controlled using a Berendsen thermostat[139] with a coupling time of 1 ps. In the *NPT* simulations, the pressure was maintained using an anisotropic Berendsen barostat[139] with a coupling time of 1 ps, such that, all three dimensions of the systems were allowed to fluctuate independently. All MD simulations were run for up to 6 μs and carried out at 271.65 K. It is important to note that this temperature factored in a model-specific 3.5 K temperature offset,[111] such that the simulation temperature is meant to model systems at 275.15 K (2 °C), at which the equilibrium pressure of methane hydrate is known to be 32 bar (Figure 3.3).[140] Sample input files, including force field parameters, from MD simulations are available online.

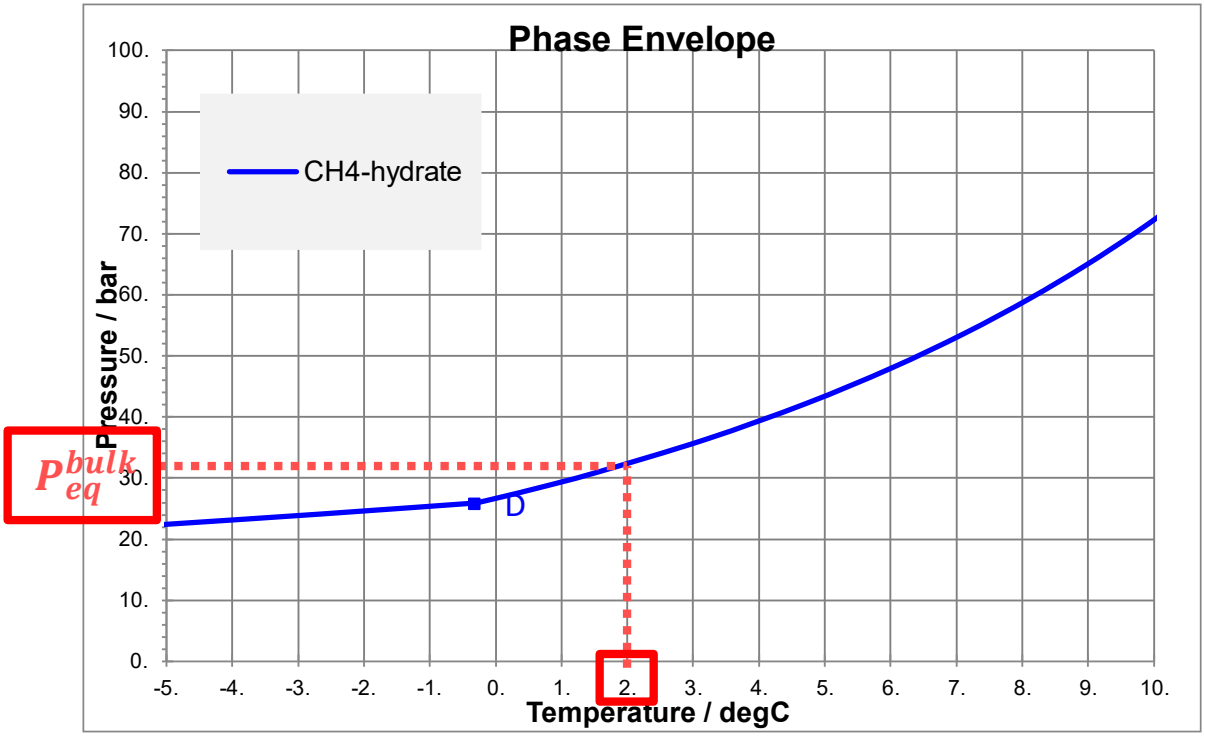

Figure 3.3: Phase diagram of the methane and water binary mixture. Along the blue curve, methane hydrate phase coexists with methane vapour and liquid water (above ice point) or ice water (below ice point).

3.3 Results and Discussion

3.3.1 Model Validation

Before investigating whether confinement effects promote methane hydrate growth, we tested the molecular models employed for methane and water for the bulk systems. For this, we conducted MD simulations in the *NPT* ensemble for the bulk systems at five pressures: 1, 10, 24, 40, and 100 bar. Previous studies have associated decrease and increase in potential energy of the system to phase transitions, i.e., hydrate growth and dissociation, respectively.[88,109,111] Figure 3.4 shows the potential energy of the bulk systems as a function of simulation time. For the systems simulated at 1, 10 and 24 bar, i.e., below the equilibrium pressure at 2 °C, a characteristic spike, which signifies hydrate dissociation,[109–111] followed by an immediate dip in the potential energy was observed after which the simulations became unstable. In these simulations, a rapid expansion of the simulation box as a result of full hydrate slab dissociation was observed. The hydrate dissociation rate was fastest at the lowest pressure. On the other hand, for the bulk system at 40 bar, the potential energy increases slightly but then stabilises after a microsecond, i.e., fluctuates around a mean

value. The initial increase in the potential is associated with the partial dissociation of the hydrate phase leading to the expansion of the simulation box. However, the subsequent stabilization of the potential energy shows that, although hydrate growth is not observed within the 6 μs simulations time, a state of three-phase coexistence was established (Figure A2), and growth may be observed at longer simulation times. Finally, in the case of 100 bar, the steady decrease in potential energy over the course of simulation indicates hydrate growth, which can be corroborated by the snapshots presented in Figure 3.5, where simulation box shrinkage can be noted. The characteristic two-step decrease in potential energy, where a "steady" decrease in potential energy followed by a "rapid" decrease in potential energy, which was reported in previous studies for hydrate growth,[88,109,111] was not observed for the bulk system we simulated at 100 bar. This implies that the hydrate growth was "gradual". Surprisingly, the formation of a methane nanobubble was not observed in the bulk system at 100 bar. This discrepancy could be attributed to the relatively lower driving force applied as compared to other studies.[88,109] Overall, the results from the bulk systems demonstrate that the molecular models employed in were able to correctly predict the behaviour of methane hydrates in bulk, such that, no growth was observed when external pressure applied was below the bulk equilibrium pressure of 32 bar and above that pressure either the growth or the onset of the growth of methane hydrates were observed.

We also looked into how dispersion corrections affect the simulation of methane hydrate growth in the bulk. For this, the simulation in the bulk at 24 bar was repeated with dispersion corrections applied to both energy and the pressure. In stark contradiction with the simulation at 24 bar in which dispersion corrections were not applied and the experimental data, turning the dispersion corrections on led, incorrectly, to complete crystallisation within about at 2.5 μs (Figures Figure A3 and Figure A4). It is apparent that dispersion corrections can yield artificial effects such that they result in an increased driving force for methane hydrate growth which can lead to crystallization at conditions such a result cannot be observed in the bulk. This is in line with the findings of Michalis et

al., which highlighted that dispersion corrections will cause gas compression and such effect is more pronounced at low pressures.

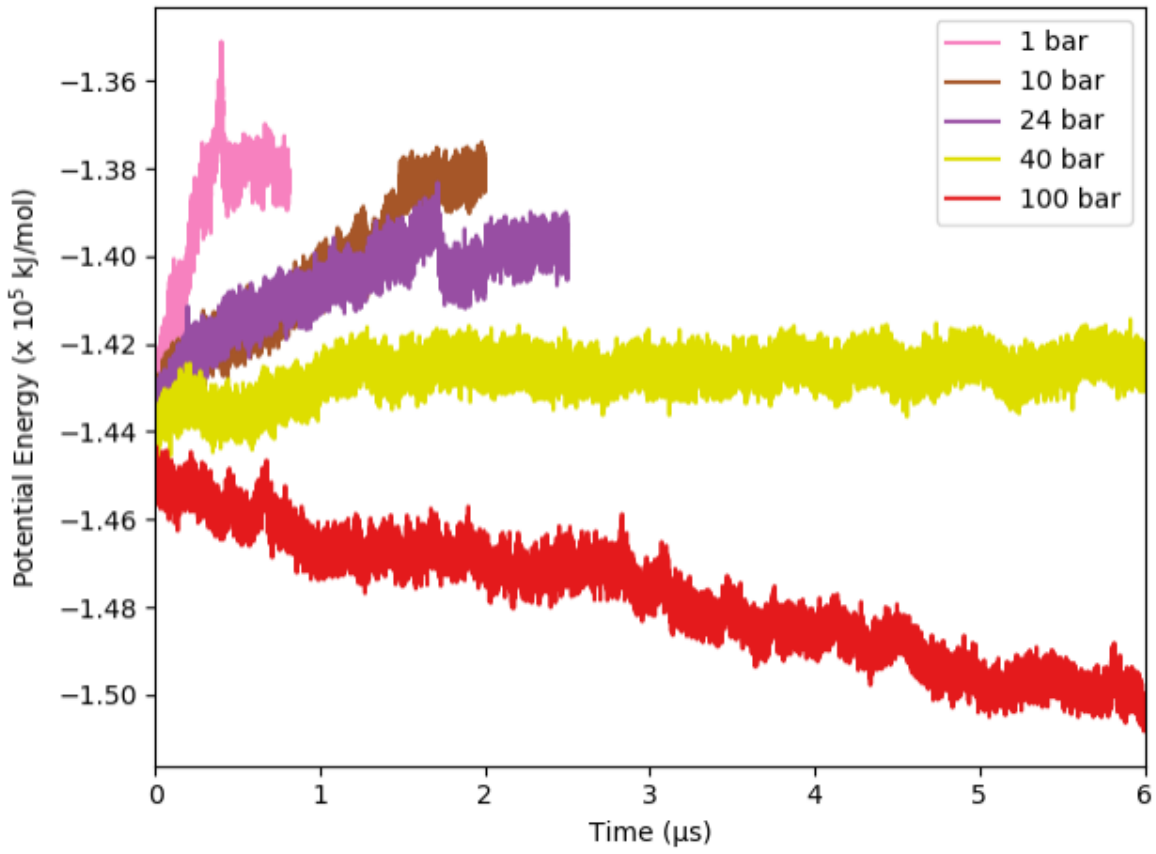

Figure 3.4: Variation of the potential energy of the bulk systems as a function of the *NPT*-MD simulation time. At 1, 10 and 24 bar, methane hydrates are not stable and dissociate (increase in potential energy). On the other hand, at 40 bar three-phase coexistence is observed (plateau in potential energy). However, at 100 bar methane hydrate growth is observed (decrease in potential energy).

(A) 1 μs

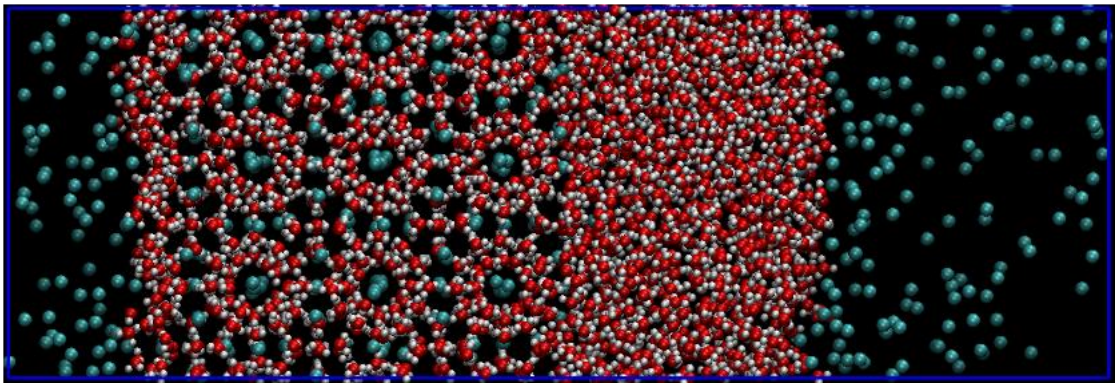

(A) 2 μs

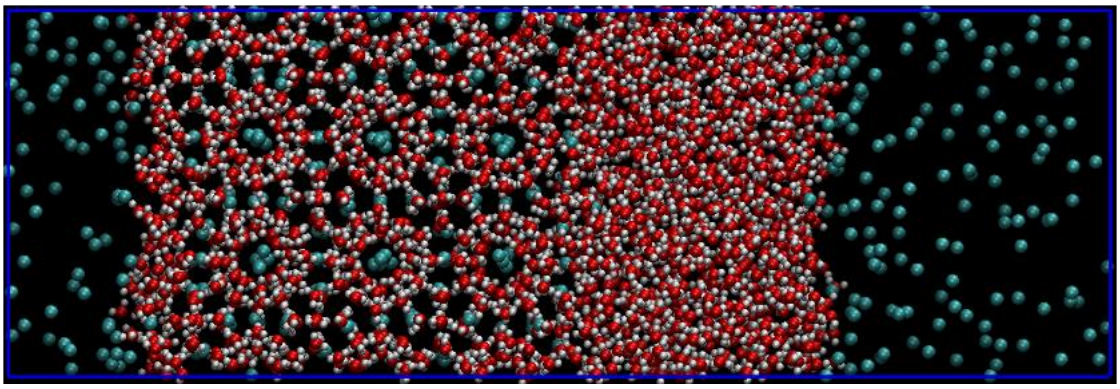

(A) 4 μs

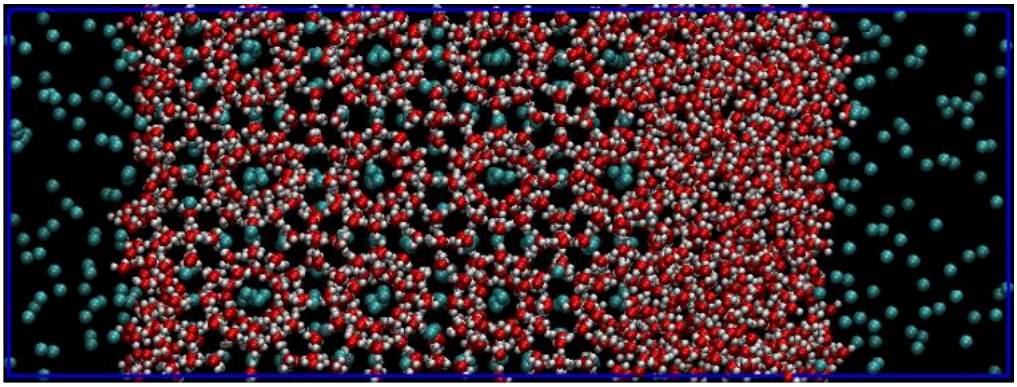

(A) 6 μs

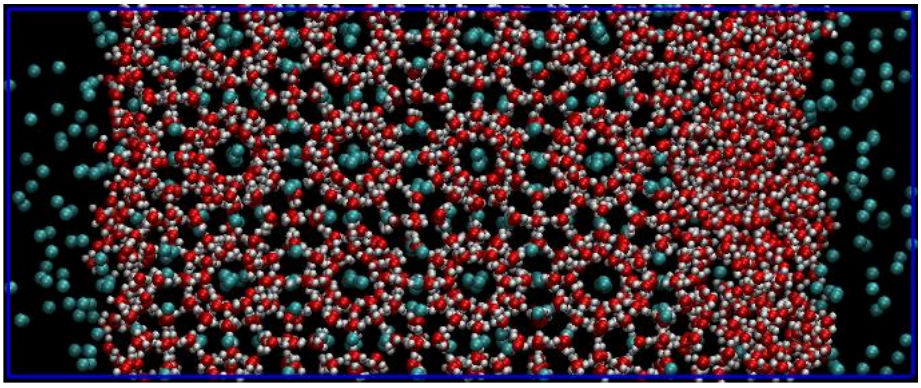

Figure 3.5: Snapshots from the bulk system simulation at 100 bar.

3.3.2 Effect of Confinement

To understand the effect of confinement on the growth of methane hydrates, MD simulations were conducted in the *NPT* ensemble where three phase configuration methane hydrates were subjected to the presence of a silica slit pore (Figure 3.2) at the following five pressures; 1, 10, 24, 40, and 100 bar. It is apparent from the results shown in Figure 3.6 that hydrate growth is observed in all simulations, and the higher the pressure the faster the growth rate of methane hydrates in confinement. The width of the silica pores, i.e., the distance between the two surfaces in the z direction, decreases with increasing pressure (Figure A7). This means the confinement effect is the smallest in the 1 bar case, yet methane hydrate growth is still observed as shown in Figure A5. Interestingly, only the simulation at 100 bar displays the commonly reported characteristic of a two-step decrease in potential energy. The results shown in Figure 3.6 can be used to interpret the progression of the simulation, i.e., a "gradual" growth step happens in the first 1.75 μs, and then a "spontaneous" growth step follows consecutively. On the other hand, all other simulations exhibit only "gradual" growth. Besides that, the growth rate was observed to be slower at 40 bar than that of lower pressures. This result is somewhat counterintuitive and may be explained by the fact that hydrate formation is stochastic and such effect is more pronounced when the driving force is low. Further analysis based on a structural order parameter, $F_{4\varphi}$, as shown in Figure A6, can be used to characterise the state of the system by probing the torsion angles of water molecules involved within a hydrogen-bonding network. The $F_{4\varphi}$ order parameter (3.1) is a function of the torsion angle between H_2O molecule pairs found within 3 Å.[141,142]

$$F_{4\varphi} = \langle \cos 3\varphi \rangle \tag{3.1}$$

where φ is the H–O…O–H torsional angle. The hydrogen atoms used to calculate $F_{4\varphi}$ are the outermost hydrogen atoms in the H_2O dimer. The final $F_{4\varphi}$ value is then obtained by averaging over all possible H_2O pairs for the entire system. The typical $F_{4\varphi}$ values for ice, liquid water and hydrate are -0.40, -0.04 and 0.70, respectively. We quantified the CH_4 hydrate growth/dissociation by analysing how the $F_{4\varphi}$ order parameter for H_2O molecules

changes as a function of simulation time. It can be observed that a decrease in the potential energy of the confined systems corresponds to an increase in $F_{4\varphi}$, indicating hydrate growth. At the end of the simulation, the $F_{4\varphi}$ values did not reach the expected value of 0.7 as the confined systems did not converge into a fully crystalline but an amorphous hydrate phase, as shown in Figure 3.7, as well as the presence of disordered water molecules adjacent to the wall surfaces.

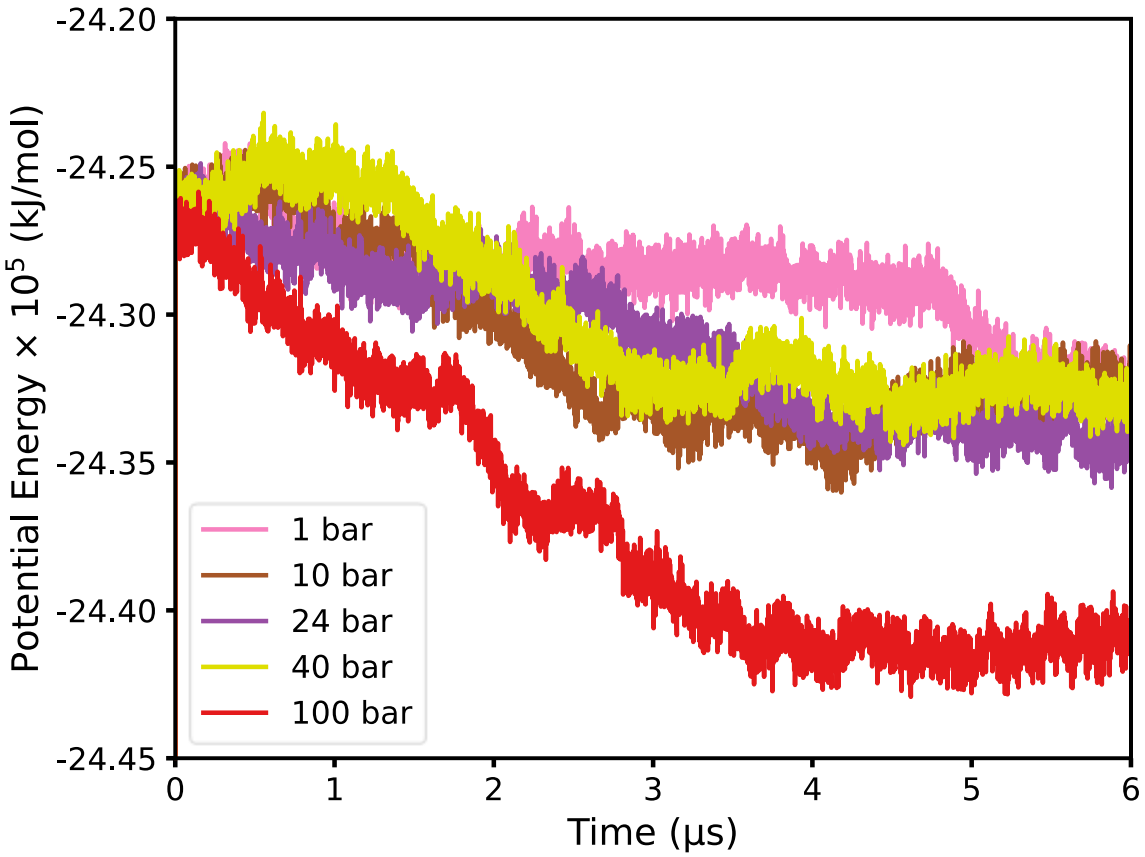

Figure 3.6: Variation of the potential energy of the confined systems as a function of the *NPT*-MD simulation time Methane hydrate growth observed in all simulations. Methane hydrate growth can be observed in all simulations (decrease in potential energy).

In the snapshots displayed in Figure 3.7 for the simulation conducted at 100 bar, first a "gradual" growth of methane hydrates from the hydrate-water interface (Figure 3.7A) as well as the formation of convex-shaped methane slab can be observed. Subsequently, a "spontaneous" lateral growth of the hydrate slab can be seen due to the formation of a methane nanobubble (Figure 3.7B-D), which were also observed by He et al.[106] In addition, incomplete and distorted hydrate cages can be observed near the silica surfaces.

(A) 1 μs

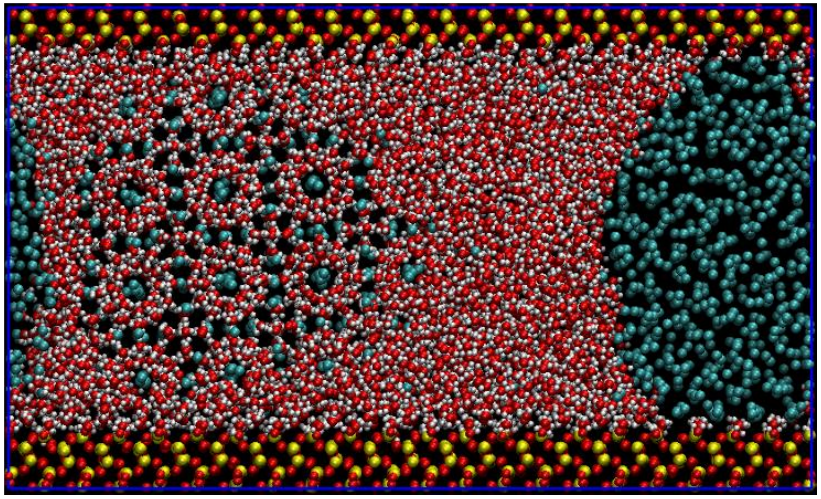

(C) 4 μs

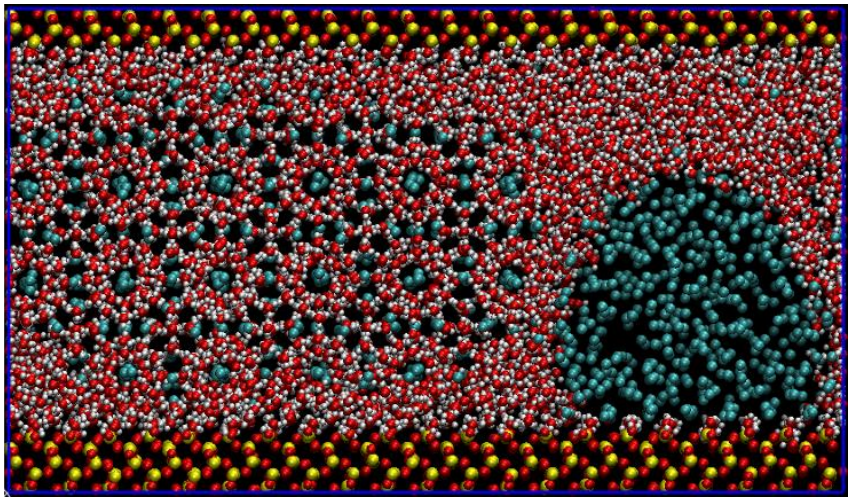

(B) 2 μs

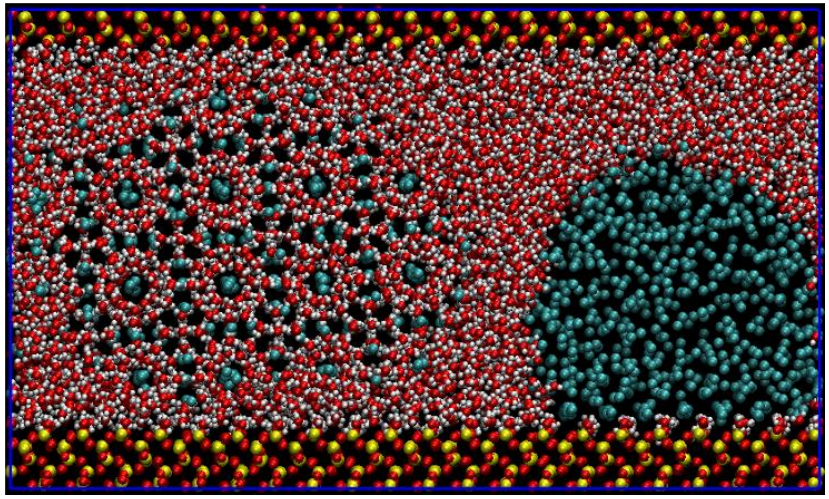

(D) 6 μs

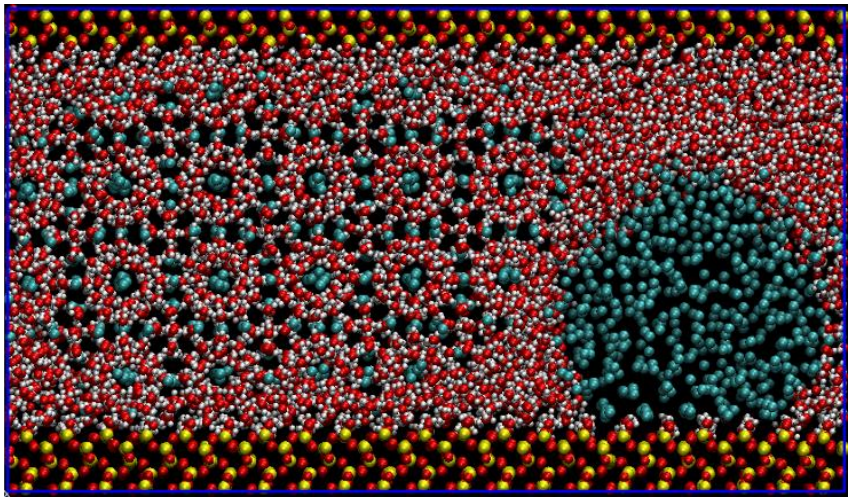

Figure 3.7: Snapshots of the confined system simulation at 100 bar.

Although initially complete cages were present adjacent to the silica surfaces, these were replaced by a thin water layer during the course of the simulation without causing the dissociation of the remaining cages. This also accords with earlier experimental and theoretical observations,[100,101,106,143] which showed that the surfaces are coated with a thin layer of ordered water due to strong hydrogen bonding with the silanol groups on silica surface. It has been hypothesised that the stabilising effect of silica on cage-like water structures may promote hydrate formation,[106] and that the formation of cage-like water structures is a necessary step for gas hydrate formation.[144] In the "gradual" growth step, hydrate growth is a mass transfer limited process as the methane molecules must first dissolve and diffuse through the water slab to the hydrate-water interface to be enclathrated, hence the potential energy decreases steadily. However, in the "spontaneous" growth step, when the growing hydrate slab came in contact with the supersaturated methane solution, the growth was accelerated, and consequently accompanied by a steep decrease in the potential energy of the system. It is well established the hydrophilicity of the surface influences the curvatures (contact angles) of water droplets due to surface wettability,[145] which in turn affects the shape of the methane slab in the confined system (Figure 3.7), making a clear distinction when compared to the bulk system (Figure 3.5) at 100 bar, where the shape of the methane slab remained the same throughout the simulation. Prior studies have noted the effects of surfaces of different hydrophobicity on the wetting angle of fluid coming in contact with the surfaces,[106,145,146] such that, it affects the Young–Laplace pressure (P_{YL}) arisen from the interfacial curvature and hence influence the concentration of methane in the aqueous phase,[147] which plays an important role in hydrate formation.[85,132,133,148] Consistent with the findings of He et al.,[106] our results show that hydrophilic hydroxylated silica surfaces promote convex-shaped (positive curvature) methane nanobubble where the direction of P_{YL} is pointing outwards. In addition, they also pointed out that when P_{YL} is pointing outwards, it increases the aqueous concentration of methane, and consequently a higher hydrate growth rate can be observed.

Comparing the energy profiles of the bulk (Figure 3.4) and confined (Figure 3.6) systems, it is clear that in the bulk systems growth of methane hydrate crystals was dependent on the external pressure applied, and that the simulation outcome reproduced the experimental methane-water phase equilibria. Whereas, in the confined systems, hydrate growth can be observed regardless of the external pressure applied, even at pressures lower than the minimum pressure required for the formation of methane hydrates in the bulk. This result could be attributed to an increased tangential pressure as well as increased probability of formation of clathrate-like water structures in confinement.[149] The latter is essential for the spontaneous onset of hydrate formation according to the cage adsorption hypothesis by Guo et al.[144]

3.4 Conclusions

In this study, by performing MD simulations, we investigated whether methane hydrate growth can take place in confinement at milder conditions compared to the bulk. This was largely motivated by recent experimental work that used porous materials for the synthetic growth of methane hydrates. Furthermore, previous molecular simulation studies of methane hydrate growth in pore systems were carried out at very high pressures, making it impossible to determine confinement could enable methane hydrate growth at pressures lower than that of required in bulk. Prior to this study, little was known about hydrate growth in confinement at low simulation pressures (≤ 100 bar). In order to gain understanding of confinement effects on methane hydrate formation at low pressures we employed the direct phase coexistence approach in our MD simulations. In the simulated bulk systems, the external pressure dictates whether methane hydrate growth is observed or not at constant temperature, such that, the behaviour of methane hydrate obeys the expected experimental methane hydrate phase equilibria. Whereas, in confinement, regardless of the external pressure applied, methane hydrate growth is observed, even at the pressures lower than the minimum pressure required for hydrate formation in bulk, suggesting, indeed, confinement effects enable methane hydrate growth at relatively milder conditions. We further showed that applying dispersion corrections (i.e., tail

corrections) could yield artificial effects that incorrectly leads to fast crystallization of hydrates.

Overall, our findings provide insights into how confinement promotes hydrate formation and can help others develop accurate methodologies and simulation settings to study the behaviour of gas hydrates in confinement. However, there still remain many points to be investigated. For instance, the pore width and shape can also be a factor for hydrate growth. Furthermore, it is not totally unambiguous how the external pressure applied in the simulations of the confined systems is representative of the pressure of the bulk methane used in the experiments to make synthetic methane hydrates in wet porous materials. To develop a full picture of the effect of confinement on hydrate growth in porous materials additional modelling and experimental research will be needed.

Chapter 4 Diffusion Behaviour of Methane in 3D Kerogen Models

The material presented in this Chapter was published in 2021 in Volume 35, Issue 20, Pages 16515–16526 of Energy & Fuels. Reprinted (adapted) with permission from Yu et al. Copyright 2022 American Chemical Society. Available online via: https://doi.org/10.1021/acs.energyfuels.1c02167.

4.1 Introduction

Shale gas is attracting considerable attention as an unconventional energy source due to the abundance and geographic distribution of shale as well as the ever-increasing global energy demand.[150,151] Recent advancements in shale gas extraction techniques such as horizontal drilling and hydraulic fracturing, which enhance the extraction volume and shale permeability, respectively, have allowed successful commercial exploitation of shale hydrocarbon resources. However, a recent assessment suggests only up to a fifth of the hydrocarbons in a shale matrix can be recovered using the aforementioned methods.[19] During production, shale gas migrates from the shale matrix to a production wellbore through a network of fractures created by the injection of pressurised fluid;[152–156] typically water, though interest in supercritical carbon dioxide based approaches is growing.[157,158] It has been established that the rate-limiting step in shale gas production lies in the gas migration from the shale matrix of low permeability into the fracture network. Thus, it is of crucial importance to understand the transport of small organic molecules in shale matrices to explain the relatively low yield and rationalize production decline over time.[159–161] Such studies are also needed to identify ways to optimize the shale gas extraction techniques.

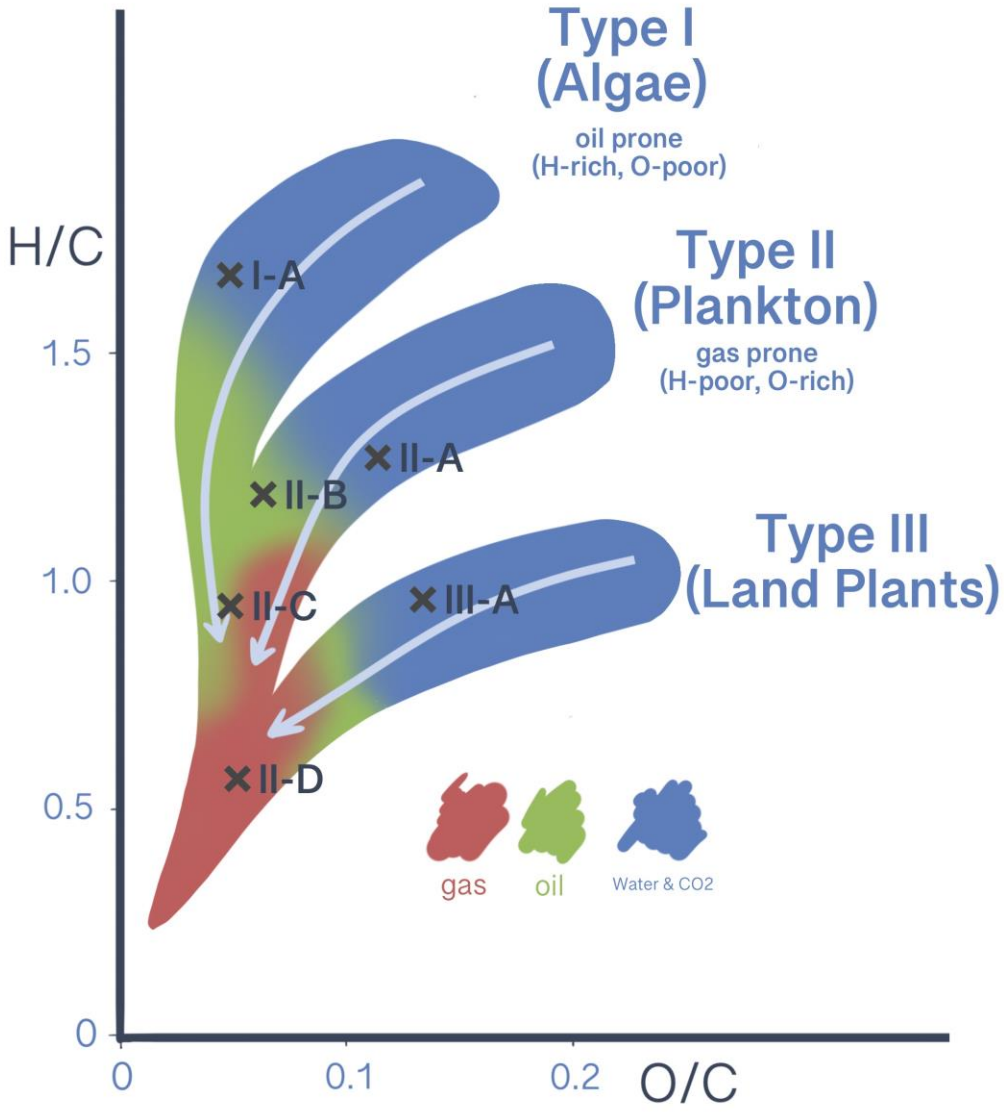

Figure 4.1: The van Krevelen Diagram.[25] The arrows indicate the transformations of kerogens over geological timescale due to thermal maturation, and the crosses mark the kerogen types considered in this work.

Within shale rocks, the majority of the organic material is present as kerogen - a waxy, complex, heterogeneous mixture of hydrocarbons found in organic matter-rich sedimentary rocks deposited in lacustrine, marine, and terrestrial environments around the world. In such an environment, kerogens formed at the end of diagenesis are slowly buried more deeply in the Earth and undergo thermal maturation (i.e., catagenesis and metagenesis), during which subsurface thermal stress causes kerogen fragments to break down chemically, eventually producing oil and gas.[18] Kerogens are insoluble in common organic solvents, such as carbon tetrachloride.[162] Because of their chemical heterogeneity,

kerogens are typically classified into three main types based on overall C/H/N ratios determined via elemental analysis. Each type (Type I, II, and III) occupies a specific region on the van Krevelen diagram (Figure 4.1),[25] a plot of H/C ratio against oxygen-to-carbon O/C ratio. The type of kerogen present in a shale depends on numerous factors, including but not limited to its biological origin, depositional environment, burial depth, and age/maturity level. Previous research[33,163,164] reports that the main factor dictating the adsorption capacity of shale samples for CH_4 and CO_2 is their total organic content (TOC), much of which is kerogen. Further studies comparing the adsorption capacity of shale and isolated kerogen samples confirmed the uptake of CH_4 and CO_2 is significantly higher in pure kerogen than that of shale.[34–37] Observing and quantifying the adsorption and transport processes in such systems presents numerous experimental challenges, such as the difficulty in obtaining shale samples and isolating pure, unaltered kerogen as well as the need to examine behaviour over many length and time scales. To mitigate these limitations, classical methods of atomistic computer simulations, such as molecular dynamics (MD) and Monte Carlo (MC) or hybrid MD/MC simulations, provide a convenient way of studying kerogen at a molecular level, providing unique insight into the behaviour of these fluids in nanometer-scale confined spaces. Molecular simulations can provide detailed insight into the kerogen structure and how that structure responds upon fluid uptake/desorption, the rate at which the uptake/desorption occurs, and the effect of fluid–kerogen interactions on adsorption and transport.

However, the complete molecular structure of isolated kerogens is not known, meaning that construction of realistic molecular models remains a challenge. Several experimental techniques, such as solid-state ^{13}C NMR spectroscopy, sulphur X-ray absorption near edge structure (S-XANES), and X-ray photoelectron spectroscopy (XPS), have been used to characterise kerogen samples.[165] These studies identify the elemental composition, the fundamental functional groups and their distribution in the structure, and chemical/structural features present in a given kerogen sample. From these data, realistic two-dimensional (2D) kerogen models can be created with appropriate overall chemical

composition and functionality. Thanks to several important studies, detailed 2D molecular diagrams of kerogen have been created for several types and maturity levels. Behar and Vandenbrouke[166] constructed detailed 2D molecular diagrams representative of the three main kerogen types at various stages of their evolution. The model structures they proposed have a high starting molecular weight for the least mature kerogens with decreasing molecular weight as kerogen maturity increases. Their pioneering work enabled Zhang and LeBoeuf[167] to modify the models in their study of the volumetric properties of immature Green River Shale kerogen. In particular, Zhang and LeBoeuf's modification brought the kerogen model in closer alignment with the chemical composition of an extracted immature Green River Shale kerogen. Following a similar approach, Siskin et al.[168] also proposed a 2D Green River oil shale kerogen model consisting of seven unique molecules based on selective chemical derivatizations and NMR spectroscopy. More recently, 3D configurations of kerogen based on Siskin et al.'s model have been built through a combination of *ab initio* and molecular mechanics calculations.[169,170] One common feature of all these models is that the kerogen molecules contain a large number of atoms to duplicate the elemental analysis data. Ungerer et al.[171] overcame this problem by creating six realistic and relatively smaller kerogen models of different types and maturity levels, covering a broad region of the van Krevelen diagram.[25] In addition to constructing models with computational efficiency in mind, incorporating prior knowledge about molecular fragments allowed them to improve kerogen models such that geometrical constraints imposed by (tetrahedral) alkane and (planar) aromatic fragments can be satisfied in 3D. The six kerogen model units are representative of kerogen samples obtained in various depositional environments, where Type I, Type II, and Type III correspond to kerogens of lacustrine, marine, and terrestrial origins, respectively. These individual molecular units can be used as building blocks to generate larger models of nanoporous kerogen matrices. Since Ungerer et al.,[171] a considerable amount of literature has been published based on their models. More recently, in the same vein, Lee et al.[172] developed three new molecular models for Type II kerogen based on a sample extracted from the Bakken formation.

In a 2016 study, Ho et al.[173] demonstrated that methane release in kerogen matrix is a two-step process, with an initial pressure-driven fast release of free gas followed by a slow release of adsorbed gas through desorption and diffusion across the low permeability kerogen matrix.[174] The second desorption/diffusion step is the rate-limiting step, with diffusion behaviour of methane in pores differing from that of bulk methane. Furthermore, Ho and colleagues show that the same packing procedure can give rise to kerogen matrices with different pore connectivity and that some methane might be trapped in isolated pores and non-recoverable. In an investigation into the swelling properties of Type II-D kerogen,[175] they observed swelling of the kerogen matrix following gas adsorption leading to increased surface area, porosity and pore size of the kerogen model. Kazemi et al.[176] calculated both self- and transport diffusion coefficients of methane in a Type II-C kerogen matrix, showing that both converge to a similar value (low diffusivity) as the pressure increases. Michalec and Lísal[177] controlled the microporosity of a Type II-D kerogen model by introducing spherical dummy particles of varying sizes (up to 15 Å) as the kerogen matrices were packed. Subsequently, they compared the adsorption of shale gas on rigid kerogen structures of different microporosity through GCMC as well as MD simulations. The simulated kerogen exhibited lower gas uptake due to lower pore space accessibility, which can be improved by modelling kerogen as a flexible matrix. They also showed that the kerogen matrix preferably adsorbs CO_2 rather than CH_4 due to stronger van der Waals and electrostatic interactions. This result corroborates earlier findings by Sui and Yao[178] and Wang et al.[179] who explored the adsorption of CH_4 and CO_2 in Type II-A kerogen matrix computationally. Through MD simulations, Pathak et al.[180] studied the swelling of flexible Type II-C kerogen by simulated annealing of kerogen models with fixed mass liquid hydrocarbons. Vasileiadis et al.[181] manipulated the porosity of Type II-D kerogen matrices of different system sizes through introduction of dummy particles of different sizes (up to 40 Å) and devised a new algorithm to characterise porosity in kerogen. Their results indicate that system size effects appear to affect the system density and pore size distribution, both of which are also affected by the choice of the force field for the simulations. Pore characteristics, e.g., methane accessible area and volume, increase with

increasing number of kerogen units as well as the number of dummy particles and the dummy particle size. In the absence of dummy particles, the pore limiting diameter (PLD) of kerogen matrices is smaller than TraPPE-UA model of CH_4.[134] They suggested using a large system size when simulating kerogen models of this kind. In a separate study, they found that a linear relationship between porosity and adsorption capacity, and that diffusion across kerogen matrices is anisotropic.[182] Zhao et al.[183] and Huang et al.[184] considered the effects of maturity and moisture content and on methane adsorption in Type II kerogen matrices. In both studies, a positive correlation has been shown between methane adsorption and kerogen maturity. This is further supported by a later study by Alafnan et al.[185] Tesson and Firoozabadi[186] reported methane adsorption in both rigid and flexible Type II-A kerogen and concluded that kerogen flexibility has limited effect on the self-diffusion of methane. It is worth pointing out that while ensuring flexibility of the kerogen matrix, their MD simulations were conducted in the *NVT* ensemble, where deformation was not accounted for. Wu and Firoozabadi[187] conducted boundary-driven non-equilibrium molecular dynamics (BD-NEMD) simulations to study the transport of methane across a matrix comprises of 60 Type II-A kerogen molecules. They noted that a reduction in the CH_4 flux is primarily driven by the change in pore size and shape as the kerogen matrix was flexible. He et al.[188] developed a new model to quantify the diffusive tortuosity of kerogens based on Type II-C kerogen. In order to realistically model mature Type II kerogens, Rezlerová et al.[189] modelled embedding of various molecules in the kerogen matrices of Type II-C and Type II-D through annealing dynamics, thereby inducing microporosity. They also subsequently introduced mesoporosity by creating a slit-shaped mesopore of varying sizes (i.e., 20 or 30 Å) between the replicated matrices to model a multi-scale pore network. They computed the adsorption isotherms of pure CH_4 and a binary equimolar mixture of CH_4 and CO_2 for their models and also evaluated the self-diffusivity of CH_4 and CO_2. They noted that an overmature Type II-D kerogen has a higher accessible surface area than a mature Type II-C kerogen due to the preferential parallel stacking of the overmature kerogen macromolecules. In addition, this stacking arrangement in the overmature kerogen creates a less tortuous micropore network, such

that the self-diffusivity of CH_4 is higher than that in the mature kerogen. Their study also complements the conclusions from other studies[177–179] that kerogens are relatively selective towards CO_2 vs. CH_4. Comparably, Sun et al.[190] represented fractures in kerogen using slit-shaped nanopores of different sizes (up to 15 Å) and studied adsorption and diffusion of pure gas and a binary mixture of CH_4 and CO_2 in Type II-D kerogen. They found that the kerogen matrix preferably adsorbs CO_2 more than the slit mesopores. Both studies observed that the CH_4 adsorption isotherm in kerogen follows type-I Langmuir adsorption behaviour. Li et al.[191] conducted MD simulations to study CO_2 storage in water-filled slit-shaped nanopores of different sizes through a kerogen matrix of the Type II series. Chong et al.[192] cluster size analysis showed the existence of pore discontinuity upon adsorption of CH_4 and CO_2, whereas with water, continuity can be observed in the micropores of Type II-A kerogen matrix. In addition, results from multiple investigations[26,178,183,192,193] into immature Type II-A kerogens with different starting number of kerogen macromolecules have demonstrated that despite achieving similar final simulated density, the differences in the porosity of the resulting packed molecular structures can be as high as an order of magnitude.

Together, these studies highlight the complexity of kerogens and that they assume a broad spectrum of pore characteristics (connectivity, constrictivity and tortuosity).[23,24] Adding to the complexity, the use of different kerogen model molecules and packing/annealing procedures may lead to different results. Whilst all the models described here are chemically representative, it is unclear how structurally descriptive they are compared to pure isolated kerogen or kerogen as it would be found in a field sample of shale. Generating a reliable and controlled distribution of 3D kerogen structures remains challenging, particularly given the limited experimental data to use as blueprints for guidance. Given these challenges, in this study we set out to qualitatively assess the diffusion behaviour of methane in kerogen matrices constructed from model kerogen molecules (as shown in Figure B1) representing different types and maturity at conditions relevant to a geological shale-gas reservoir (365 K and 275 bar).

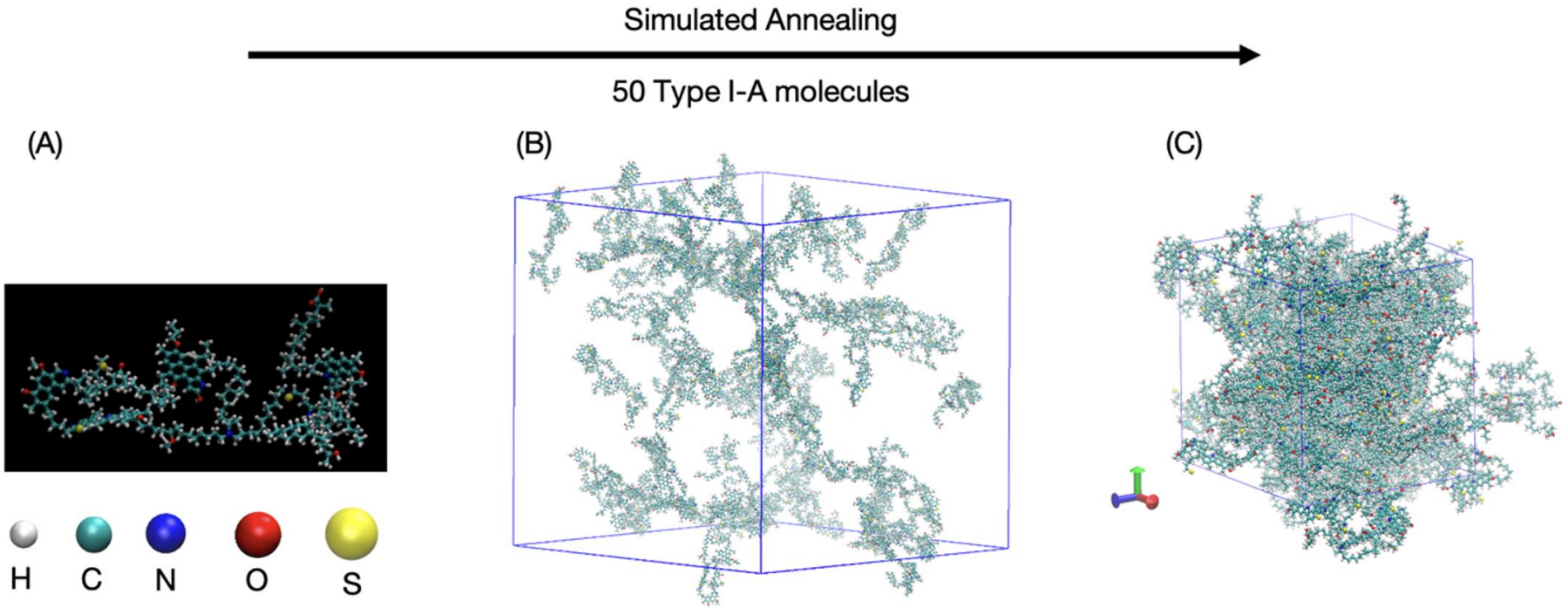

Figure 4.2: A schematic diagram of the annealing/relaxation procedure. (A) A single Type I-A kerogen unit. (B) The initial configuration of the system before annealing. (C) A kerogen matrix of Type I-A after annealing.

A sufficiently large number of macromolecules (i.e., 50) were used to avoid system size effects noted in the literature and no dummy particles were involved to introduce porosity. Unlike earlier studies,[179,182,186] which conducted their studies in *NVT* ensemble with a relatively short simulation time, in order to mimic reservoir conditions and allow realistic deformation (swelling) of the kerogen matrices, here we computed the MSD of CH_4 in hundred nanosecond long MD simulations via both *NVT* and *NPT* statistical ensembles. To the best of our knowledge, this is the first study to include all major kerogen types, enabling this work to provide a broader overview of CH_4 diffusion in kerogens.

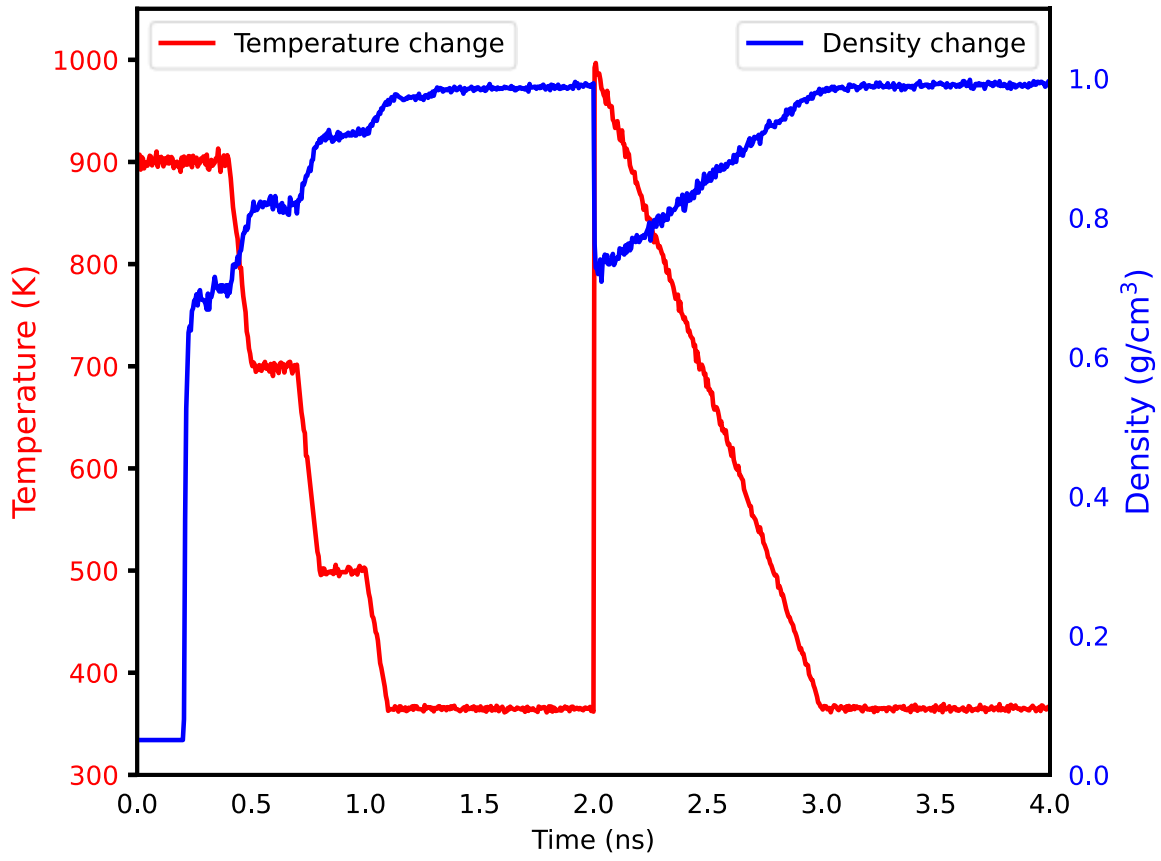

Figure 4.3: Heating and cooling profile during annealing dynamics for Type I-A kerogen.

4.2 Methods

Whilst the exact structures of bulk kerogen are unknown, many researchers have utilised simulated annealing procedures to construct model kerogen matrices out of several model

kerogen molecules (Figure 4.2), where a number of molecular units of a kerogen type are first placed in a large simulation box (low initial kerogen density). The box is subsequently equilibrated through a series of cooling and heating cycles, often in a stepwise manner and at high pressure, resulting in a condensed structure, i.e., a matrix. The density of the final configuration is then compared against experimental data of the corresponding kerogen type to validate the packed structure.

4.2.1 Creation of Bulk Kerogen Matrices

The relaxation procedure set out by Michalec and Lísal[177] was closely followed to prepare the initial configuration of bulk kerogen matrices. 50 kerogen macromolecules were randomly inserted into a large cubic simulation box with an initial system density of ~0.05 g/cm^3 to avoid interactions with copies of their images through the imposed periodic boundary conditions. This was done for each kerogen type reported by Ungerer et al.[171] Then the systems were relaxed through energy minimisation via steepest descent, followed by annealing dynamics. A total of 12 cycles were executed as described in Table 4.1. The choice of final temperature and pressure represents a typical shale reservoir at ~3-4 km depth. Figure 4.3 shows the changes in system density during annealing for Type I-A system, as an example. To reduce the statistical uncertainty, this relaxation procedure was carried out with ten independent runs, and to check for convergence, the final system density of 10 matrices was then averaged and compared to experimental data. We then randomly selected three of the 10 relaxed matrix structures for the subsequent grand canonical Monte Carlo simulations (GCMC).

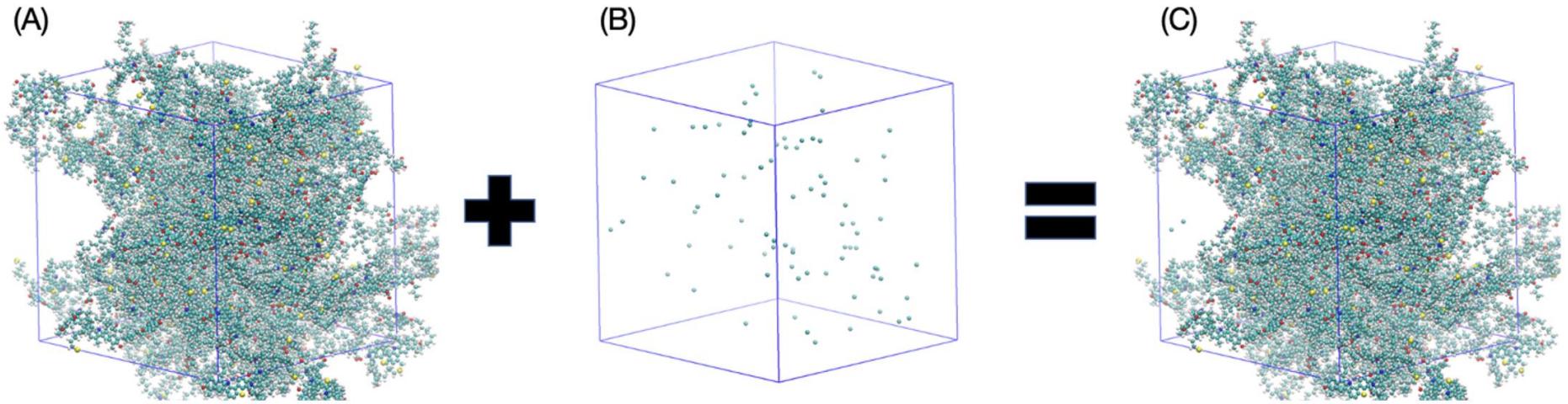

Figure 4.4: A schematic diagram of the preparation of kerogen matrix loaded with methane. (A) An unfilled kerogen matrix. (B) A random initial configuration of methane molecules, where the capacity was pre-determined through GCMC. (C) A filled kerogen matrix.

4.2.2 Grand Canonical Monte Carlo Simulations

GCMC simulations were employed to compute CH_4 loading in selected matrices for each kerogen type. In the grand canonical ensemble, the chemical potential (μ), volume (V) and temperature (T) of the systems are fixed whereas the number of molecules fluctuate. The GCMC simulations allowed us to compare variations in CH_4 loading due to packing as well as to determine the number of CH_4 molecules to insert in the kerogen matrices for MD simulations (Figure 4.4).

Table 4.1: The annealing procedure for the creation of kerogen matrices.

Ensemble	**T (K)**	**P (bar)**	***t* (ns)**
NVT	900	–	0.2
NPT	900	10	0.2
NPT	900 → 700	10	0.1
NPT	700	10	0.2
NPT	700 → 500	10	0.1
NPT	500	10	0.2
NPT	500 → 365	10	0.1
NPT	365	10	0.2
NPT	365	10 → 275	0.2
NPT	365	275	0.5
NPT	1000 → 365	275	1.0
NPT	365	275	1.0

4.2.3 Molecular Dynamics

In order to generate the initial configurations for MD simulations, one of the three kerogen matrices used in the GCMC simulations was selected for each type of kerogen. We randomly inserted the number of CH_4 molecules corresponding to the predicted CH_4 loadings from GCMC simulations into the kerogen matrices. The steepest descent algorithm was used to relax the CH_4 loaded systems to avoid bad contacts. Then, the systems were subjected to an NVT MD run and successively an NPT run, both for 100 ns where N, V, T and P represent the number of atoms, volume, temperature, and pressure, respectively.

In order to minimize statistical error, we performed five independent MD simulations for each kerogen type, with randomly determined different initial CH_4 positions in the matrix. Finally, we computed the mean square displacement (MSD) of methane molecules for each kerogen matrix in all three directions of Cartesian space. The entire workflow for the simulations is illustrated in Figure B2.

4.2.4 Kerogen and Methane Interaction Potentials

A number of force fields have been used to model kerogen, including but not limited to, COMPASS,[194] CVFF,[195] DREIDING,[196] GAFF,[197] and PCFF+.[171] PCFF+ was originally used in the development of kerogen model units by Ungerer et al.[171] However, the short-range non bonded interactions in PCFF+ are described by a repulsive–attractive 9–6 Lennard-Jones (LJ) potential, which is incompatible with many other force fields that include a 12–6 LJ potential, such that it is difficult to simulate kerogen with other compounds. CVFF is one of the most commonly used force fields in kerogen simulations,[173–175,177,191,192] and the 12–6 LJ potential in its functional form is compatible with other force fields. CVFF correctly reproduces the experimental density of the Type II kerogen series[191] and provides a reasonable description of kerogen interactions with its constituents, e.g., carbon dioxide (EPM2),[198] methane (TraPPE-UA),[134] and water (SPC).[199] The partial atomic charges of CVFF atoms were assigned using a bond increment scheme. In this study, we further extended the application of CVFF to model two additional immature kerogen types, namely, Type I-A and Type III-A. Methane molecules were represented by the TraPPE-UA model,[134] which has been shown to correctly predict thermodynamic properties and reproduce experimental phase equilibrium data. The relevant simulation input files and force field parameters used in this work can be found online.

4.2.5 Simulation Settings

RASPA molecular simulation package[200] (2.0.39) was used for GCMC simulations. Each GCMC run included a 5×10^5 initialization cycle followed by a 5×10^5 production cycle, where each cycle is N steps. N is equal to the number of particles present in the system.

Owing to the enormous number of atoms involved, for computational efficiency, kerogen structures at this stage were treated as a rigid framework, and the methane-kerogen interactions were pretabulated. During the GCMC simulations, insertion/deletion, translation, and reinsertion of methane molecules were sampled with equal probability (approx. 33 %). The acceptance rules for insertion and deletion in the grand canonical ensemble included fugacity, a measure of chemical potential, and was calculated using the Peng–Robinson equation of state for methane.[201]

All MD simulations were performed using GROMACS 2020.4 molecular dynamics simulation software.[137] A time step of 0.5 fs was used in the integration of Newton's equations of motion via the leapfrog algorithm. During the annealing procedure, a velocity rescaling thermostat[202] was used to control the system temperature, whereas during the MD production runs, a Nosé–Hoover thermostat[57,58] with a coupling time of 0.1 ps was used. In the NPT simulations, the pressure was maintained using an anisotropic Parrinello–Rahman barostat[62] with a coupling time of 0.5 ps, such that all three dimensions of the systems were allowed to fluctuate independently to allow realistic deformation of kerogen matrices. Long range Coulombic interactions were calculated using a smooth particle mesh Ewald (PME) method[138] of a fourth order polynomial with a mesh width of 0.12 nm.

In both MD and MC simulations, periodic boundary conditions were applied in all three directions. LJ potential was used to describe short-range non-bonded interactions. The LJ interactions of unlike atom pairs in different molecules or further than 3 bonds of the same molecule were calculated using the Lorentz-Berthelot mixing rules. A cut-off radius of 14 Å was used for the LJ interactions and the real part of the Ewald summation. Long-range dispersion corrections were not applied to energy or pressure. All simulations were carried out at 365 K and 275 bar unless stated otherwise. Sample input files, including force field parameters, from MD and GCMC simulations can be obtained online.

Utilising PoreBlazer v4.0,[203] a grid-based algorithm was used to calculate and characterize the porosity of the kerogen matrices, before and after the MD simulations. Settings in PoreBlazer were modified such that CVFF interaction parameters, 14 Å cut-off radius, and the cubelet size of 0.2 Å were used in the calculations. Pore limiting diameter, which is defined as the maximum penetrant diameter where a pore network remains percolated, was calculated. In addition, accessible pore volume was estimated with the Widom's ghost atom insertion method[204] by using a helium probe, with parameters taken from Hirschfelder et al.,[205] where $\sigma_{He} = 2.64$ Å and $\frac{\varepsilon}{k_B}_{He} = 10.9$ K. Accessible geometric surface area of the kerogen matrices was calculated using a N_2 probe of size 3.314 Å.[206]

4.3 Results and Discussion

4.3.1 Kerogen Model Validation and Characterization

Before investigating the effects of anisotropy and heterogeneity of the different kerogen matrices, we validated the CVFF force field to ensure the calculated densities of the kerogen matrices are comparable to experimental data. For each kerogen type, we created 10 condensed kerogen matrices, each starting from a random initial configuration of kerogen molecules, using the simulated annealing procedure outlined in the methods. Table 4.2 shows the average simulated density of six kerogen types in comparison to relevant experimental data. The density of Type I-A compares quite well with the Green River Shale sample. However, the densities of the Type II kerogen series appear to be slightly lower or close to the lower bound of experimentally measured Kimmeridge Clay kerogen densities, except for Type II-B for which we found no experimental comparison set in the literature. A possible explanation for this might be that Ungerer et al.'s Type II kerogen model molecules[171] are based on Duvernay kerogen samples. It is well understood that kerogens of the same maturity may exhibit different chemical compositions,[165] even when extracted from the same geological site. In addition, their composition is also dependent on the evolutionary history of the sedimentary formation that they formed in and the heterogeneity in composition of kerogen samples. Experimental data[207] suggest that Duvernay kerogens have a density range of 1.28 ± 0.3 g/cm^3, which our results fit well.

Similarly, the same explanation applies to Type III-A kerogen,[165] since the calculated density is reasonably close to the lower boundary of the reported range. A comparison of our results with the density of Type II kerogens from other modelling studies shows that our results are slightly lower than the reported values. It is important to highlight that during the initial step of our packing procedure, the kerogen units were inserted randomly to account for a wide range of structural variations, whereas most researchers[177,186,192] considered limited cases, where the kerogen macromolecules were oriented in the same direction, with the assumption that they will ultimately evolve into a uniformly layered kerogen matrix. Furthermore, the discrepancy between our results and those of other Type II modelling studies could be attributed to the packing procedure and conditions or the number of kerogen molecules involved. Vasileiadis et al.[181] reported system size effect when using kerogen models of the same kind, where system density decreases as the number of kerogen molecules increases. It seems possible that these results are related to the favourable stacking of the polyaromatic units of kerogen macromolecules,[208] where pores in one direction may be elongated and cause reduction in system density. Overall, the simulated density of kerogen matrices is in the range of 0.96 – 1.20 g/cm^3 which is in line with the general trend of the available experimental and modelling data.

Table 4.2: Comparison of experimental and averaged simulated kerogen densities at 365 K and 275 bar.

Kerogen Type	**Source**	**Density (g/cm^3)**	
		Experimental	**Simulated**
I-A	Green River Shale	0.95[209]	0.964 ± 0.004
II-A	Kimmeridge Clay Formation	1.18–1.29[210]	1.117 ± 0.008
II-B	-	-	1.080 ± 0.017
II-C	Kimmeridge Clay Formation	1.18–1.25[210]	1.138 ± 0.022
II-D	Kimmeridge Clay Formation	1.30–1.40[210]	1.305 ± 0.015
III-A	Blanzy–Montçeau Basin	1.16-1.20[211]	1.119 ± 0.060

4.3.2 GCMC Simulations

To account for structural variation that arises during the annealing procedure caused by the random initial configurations of the kerogen units used, we first randomly chose three of the 10 packed structures for each kerogen type for a consistency check. First, we perform GCMC simulations to determine their CH_4 adsorption capacity. Table 4.3 shows an overview of methane adsorption for the kerogen matrices estimated via GCMC simulations. It is apparent that immature kerogen of Type I has the lowest methane uptake, followed by relatively moderate and high methane adsorption capacity for Type II-A and Type III-A immature kerogens, respectively. In addition, the CH_4 adsorption capacity increases with thermal maturity in Type II kerogen series. These results match those observed in earlier modelling studies[26,183–185,189] and experimental measurements.[212–216] The CH_4 adsorption capacity was found to be highest in Type II-D kerogen compared to the other kerogen types.

Table 4.3: The amount of CH_4 loading in various rigid microporous kerogen matrices obtained via GCMC simulations at 365 K and 275 bar.

Kerogen Type	**Loading (mmol/g)**
I-A	0.430 ± 0.002
II-A	0.683 ± 0.001
II-B	1.353 ± 0.001
II-C	1.363 ± 0.002
II-D	2.034 ± 0.004
III-A	1.969 ± 0.002

The amount of CH_4 loading has a positive correlation with increasing aromatic content of the kerogen units, where Type II-D kerogen has the highest percentage of aromatic content of all.[171] This can be explained by the preferential parallel stacking of the polyaromatic parts of the kerogen macromolecules,[208] and hence larger accessible surface area, resulting in increased CH_4-kerogen interactions.[189] The results of the aforementioned relationships are depicted in a scatter plot in Figure 4.5. From the chart, there is a clear trend of increasing CH_4 loading with the increase of the aromatic carbon content and surface area of the kerogen matrices. Closer inspection of the figure shows that the surface areas of the

considered kerogen matrices are not uniform, and this is likely due to the packing procedure that we employed. The computed methane uptake in our overmature Type II-D kerogen models, which did not have any artificially induced microporosity, is 2.5 times higher than that reported by Michalec and Lísal.[177] A possible explanation for this might be that Michalec and Lísal[177] used a smaller number of kerogen molecules and are therefore more susceptible to finite size effects. It has been reported that structural properties such as methane accessible area changes with the number of macromolecules as well as the packing procedure used.[26,178,181,183,192,193] As a result, the pore network characteristics of the packed structures from our studies are likely to differ from other studies whether artificial porosity is introduced in those studies or not. As a result of these size effects and a limited sample size, the relationship between pi stacking and increased surface area might not generalize for other kerogen types or packing methodologies.

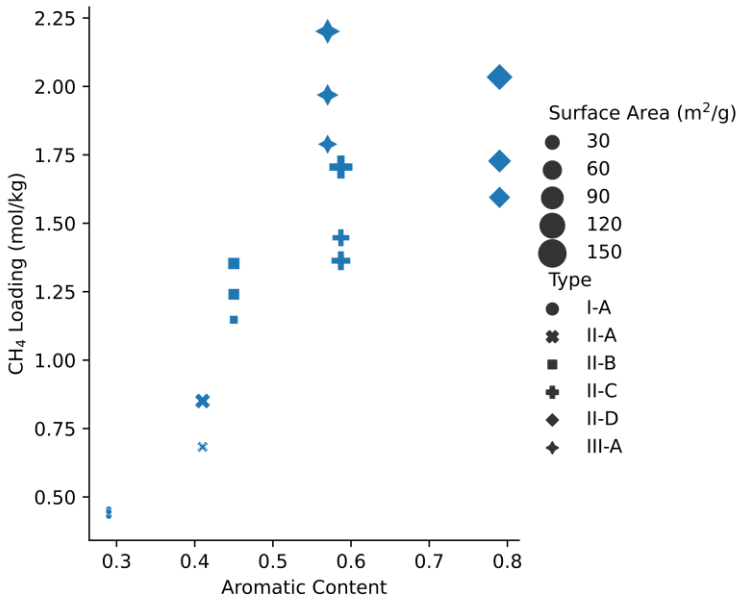

Figure 4.5: The amount of CH_4 loading versus the surface area of 3D kerogen models of various types and the fraction of its aromatic carbon content. The size of the data points corresponds with the surface area of the kerogen matrices.

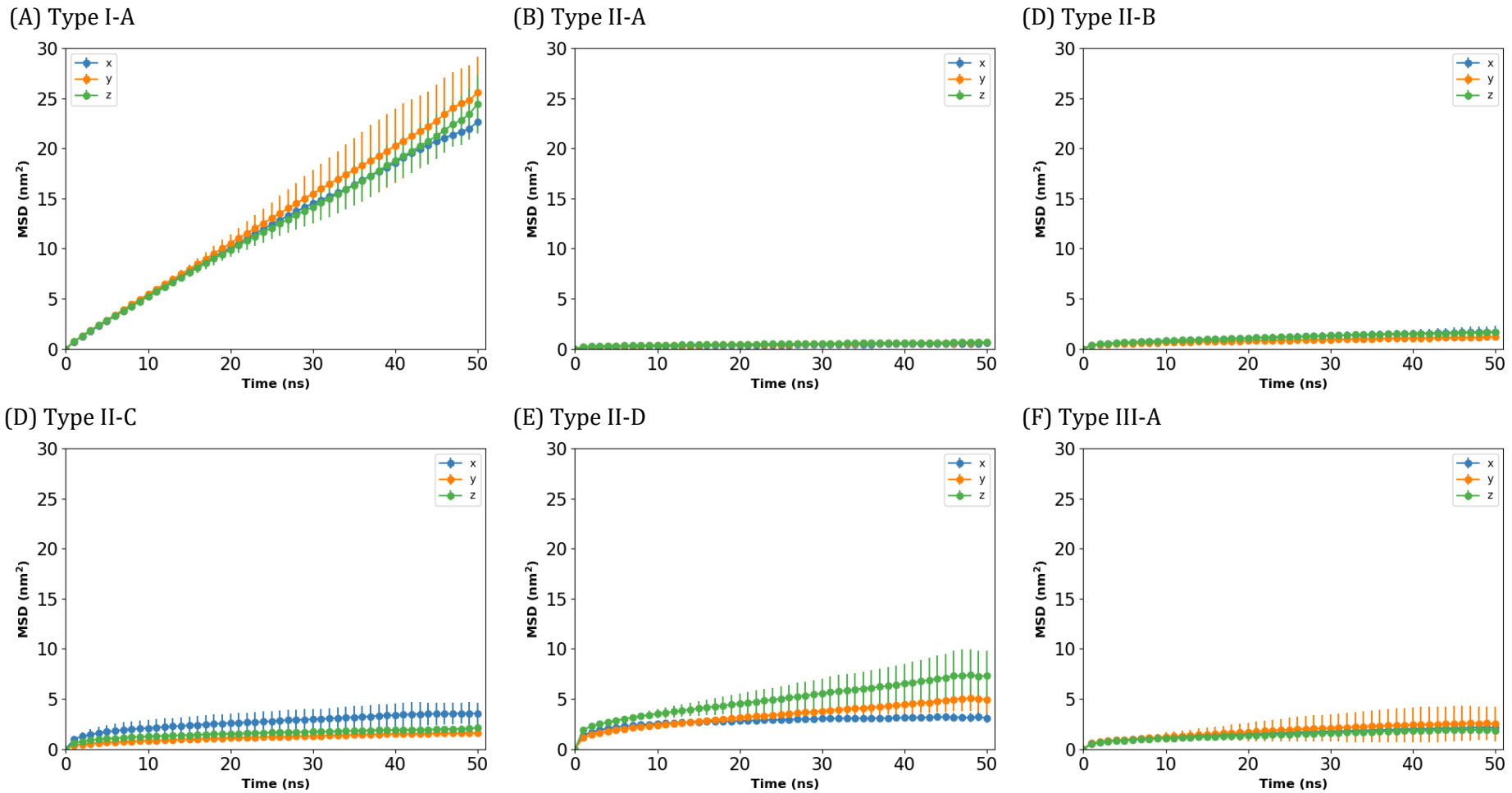

Figure 4.6: The averaged MSD plots of CH_4 in the x, y and z directions from five independent *NPT* ensemble MD simulations in six kerogen types at 365 K and 275 bar. Refer to Figure B4 for an unscaled version of each plot and Figure B7 for analysis of anisotropy in MSD of methane molecules.

4.3.3 Methane Self-Diffusivity

Diffusion is the primary mode of gas transport in shale rocks, making diffusion rates crucial for understanding hydrocarbon recovery and the factors that influence it. Anisotropic behaviour of shale rocks as a result of shale bedding has been found to influence permeability. A number of recent studies[179,182] have reported anisotropy in Type-II kerogen structures. To improve our understanding of shale gas transport mechanisms (i.e., mainly CH_4), we computed the MSD of pure CH_4 along all three Cartesian directions in kerogen matrices of different types and maturity levels. Isolated and connected pores exist in kerogen and will almost certainly affect methane uptake and mobility; thus, we randomly inserted CH_4 into the selected kerogen matrices to evaluate the effect or pore network accessibility on CH_4 self-diffusivity. For each kerogen type, five CH_4-loaded matrix configurations were generated such that each configuration had different initial positions of CH_4. A total of 30 EMD simulations were performed, i.e., five for each kerogen type. Figure 4.6 displays the averaged MSD plots for CH_4 in various kerogen matrices over the last 50 ns in the NPT ensemble at 365 K and 275 bar. Similar to the earlier observation, Type I-A kerogens exhibit isotropic behaviour with no appreciable difference in the MSD in any direction (Figure B7). Looking at the MSD plots for Type II-A and Type II-B kerogens, there appears to be 2D planar regions where the diffusion rate is similar and differs from that perpendicular to the plane. MSD plots of Type II-C show a large standard deviation for the x-component but a low standard deviation for their y-component, suggesting a more uniform interconnected pore structure such as a channel in the y-direction. Both MSD plots for the Type II-D and Type III-A kerogen models show a similar behaviour to that of Type II-C kerogen. Figure B8 displays the MSD of bulk CH_4 subjected to at the same EMD simulation settings. From the plots, we can see that it is at least three order of magnitude higher than CH_4 adsorbed within the kerogen matrices. Furthermore, radial distribution function plots of CH_4 with atoms of different functional groups present in kerogen models (Figure B6) show that predominant methane binding sites may vary from one kerogen model to another. Due to the specific composition of the model and the specific conformations limiting access to certain types of sites for some models. But overall,

it appears that sulphur, nitrogen, and oxygen atoms of different functional groups provide the majority of preferred binding sites.

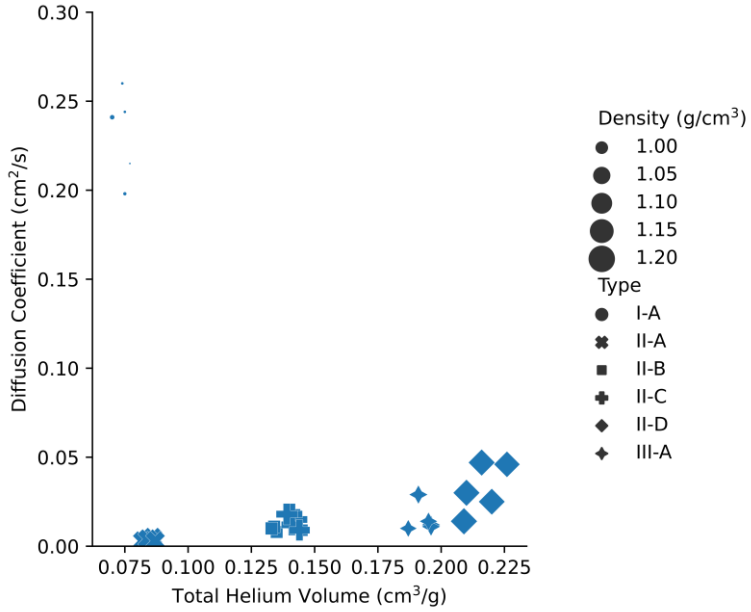

Figure 4.7: Diffusion coefficients of CH_4 in kerogen matrices of various types versus its density and helium accessible pore volume. The size of the data points corresponds to the density of the emptied and swollen kerogen matrices.

Figure 4.7 presents the scatter plot of the relationship between the diffusion coefficients of CH_4 and the density and pore volume of the swollen kerogen matrices. The most interesting aspect of this graph is that, apart from Type I-A kerogens, a positive correlation is found between the diffusion coefficients of CH_4 and the pore volume of kerogens. The most unexpected result is the anomalous CH_4 diffusion rate in Type I-A kerogens, which suggests that there are other factors at play that affect the CH_4 diffusion in kerogen matrices. The observed increase in CH_4 diffusion could be attributed to the lack of aromatic carbon in Type I-A kerogens, where less stacking could potentially create more diffusion paths. Moreover, the highly branched nature of the model unit of Type I-A could have created additional channels, such that CH_4 could permeate easily in all three directions, i.e., isotropic diffusion. The percentage of aromatic groups in kerogen molecules increases from Type I to Type III kerogen, with the highest in Type II-D kerogen.

Table 4.4: Properties of six kerogen models before and after five MD simulation runs.

Property	Kerogen Type	Initial	Final*	Change (%)
Volume (nm^3)	I-A	328.58	330.06 ± 0.97	0.45
	II-A	289.11	290.30 ± 0.91	0.41
	II-B	262.33	265.13 ± 1.25	1.07
	II-C	250.45	253.56 ± 0.54	1.24
	II-D	161.04	165.25 ± 0.77	2.62
	III-A	249.08	252.08 ± 0.74	1.20
Pore limiting diameter (Å)	I-A	1.580	1.578 ± 0.183	-0.13
	II-A	1.540	1.542 ± 0.098	0.13
	II-B	1.890	1.892 ± 0.190	0.11
	II-C	2.460	2.460 ± 0.284	0.00
	II-D	2.930	2.932 ± 0.544	0.07
	III-A	2.960	2.956 ± 0.445	-0.14
Helium accessible pore volume (cm^3/g)	I-A	0.061	0.074 ± 0.002	21.64
	II-A	0.071	0.085 ± 0.002	19.72
	II-B	0.117	0.137 ± 0.004	17.44
	II-C	0.118	0.142 ± 0.002	20.00
	II-D	0.176	0.216 ± 0.006	22.84
	III-A	0.167	0.193 ± 0.004	15.57

The increase in polyaromatic regions of the kerogen units and subsequent stacking of these regions may result in a matrix that is not amorphous and hence create a system with anisotropy. The MSD of CH_4 in Type I-A kerogen is an order of magnitude higher than the other kerogen types, which suggests that in Type I-A, CH_4 has the fastest diffusion rate compared to other kerogen types. This makes sense in light of the lower density of this material and the larger size of the molecular units, leading to a packed structure with greater pore volume and connectivity compared to the other packed models. The lowest diffusion rate is observed for the Type II-A kerogen. The results from the Type II kerogen series further support previous findings[179,182] that diffusion behaviour of CH_4 in Type II kerogens is anisotropic, although many of the observed differences occur within the error bars on each plot. The magnitude of the standard deviations can be attributed to different

pore space accessibility as a result of several factors outlined above. In general, the magnitude of the standard deviations is similar between different plots (typically fractions of a nm^2 at early stages of the simulations and roughly 2-4 nm^2 - after 50 ns) and is on the same order of magnitude for each direction.

4.3.4 Volume Changes Upon CH_4 Adsorption

Table 4.4 compares the structural properties of the kerogen matrices before and after MD simulations, showing that kerogens experience volumetric strain upon CH_4 adsorption. This is consistent with other literature data.[175,178] In addition, the pore limiting diameter of all kerogen matrices appears to be smaller than the methane molecular diameter in the TraPPE-UA force field, i.e., 3.73 Å. This suggests methane should not be able to diffuse through the percolated pore network. Yet some diffusion is observed, most notably in the Type I-A model (Figure 4.6). This finding is consistent with the trend reported in an earlier study[181] for Type II-D kerogen. Diffusion of CH_4 through pores that are too small to permit methane motion suggests that the CH_4 molecules themselves may actively change pore accessibility, opening up micropores that were previously inaccessible. Indeed, pore size distribution analyses of kerogen models before and after the MD simulations suggest that methane imbibition has caused a shift of pore size distribution from the initial peak at approx. 3.2 Å to 3.8 Å, which is about the size of a TraPPE united atom methane molecule (Figure B5). Slow diffusion observed in kerogen types other than Type I-A could be due to CH_4 molecules being confined and localized in small nanospaces, i.e., isolated pores with no diffusion pathways. Finally, total helium volume of the kerogen matrices appears to have increased after CH_4 adsorption, which suggest that CH_4 adsorption increases the porosity of the matrices, consistent with the hypothesis that CH_4 actively opens diffusion pathways. Additional studies that can provide energetic insight into this process are warranted. Vasileiadis et al.[182] reported that the self-diffusion coefficient has a positive correlation with the pore limiting diameter. However, the findings of this study do not support their results. However, the findings of this study do not support their results. In any case, construction of 3D kerogen matrices from relatively low molecular weight

kerogen macromolecules should be handled with care as the lack of cross-linking between kerogen units may allow increased flexibility which is not present in real kerogen.[177]

4.4 Conclusions

The primary motivation of this study was to examine CH_4 diffusion in 3D kerogen matrices built from model kerogen molecules that span the recognized types and maturity levels of natural kerogens. The MD and GCMC simulation results reported here show that swelling of the 3D kerogen matrix occurs upon CH_4 adsorption. Methane adsorption also induces other changes in the pore network such as variations in the pore limiting diameter and accessibility between pores in the network. Importantly, all kerogen structures exhibit some degree of anisotropy in the CH_4 diffusion behaviour with the exception of Type I-A kerogen (Figure B7), the least mature and lowest density model. As has been observed for fluid diffusion in other microporous to nanoporous materials, the diffusion of CH_4 in kerogen matrices is slow compared to bulk CH_4.

This study has many broader implications for understanding CH_4 diffusion and recovery in kerogens and shales. The scientific community already knows that kerogens contain a significant fraction of the methane in shale-gas reservoirs[217–219] and that the recovery of methane from shale-gas reservoirs is low compared to other types of gas reservoirs (a few 10s of %).[220,221] What is less clear is why the recovery is so low and what can be done about it. The solutions to both of these questions rely on a detailed molecular-scale understanding of CH_4 behaviour in shales and all shale components, including kerogen. The ability to extract kerogen and know the extracted kerogen has the same physical and chemical characteristics as kerogen in the native rocks is currently limited. Thus, computational approaches are likely key to developing a molecular-scale understanding of what is happening in shale-gas reservoirs and will also be needed to help verify experimental data once the community at large is able to collect detailed molecular-scale experimental data for methane adsorption and dynamics in kerogens. Thus, there is a pressing need to have good computational models of kerogens, to understand how to build realistic computational

models of kerogens, and to do both of these for a broad range of kerogen types. Due to the scope of the kerogen models examined in this study and the clear procedures for generating kerogen matrices, one of the more important broader implications of the present study is that it forms an important baseline data set for future research into gas recovery from kerogen. These results also highlight several operational considerations that must go into creating computational models of kerogen and interpreting and comparing the associated molecular modelling data sets. Operationally, the annealing procedure employed when creating a 3D kerogen matrix from small representative model molecules plays an important role in determining the final pore characteristics of the dense kerogen structures. More research is needed to understand the relationship between the annealing method and the pore accessibility of the resulting packed structures. To improve consistency between modelling studies and applicability to the field, our results and those in the literature also suggest that more experimental data are required regarding the pore network and network connectivity and that future modelling studies must map the model kerogen matrix pore network to match these data. Based on the volume expansion and potential active role of CH_4 in the pore network, future work should be conducted under NPT conditions to enable swelling of the kerogen matrix. Likewise, additional modelling studies that estimate the energetics of methane adsorption and kerogen matrix swelling are warranted to improve our understanding of CH_4 transport thermodynamics in this important phase of shale gas reservoirs. The results presented here make it possible to conduct new and much needed modelling calculations of thermodynamic parameters regarding methane adsorption in a broad array of kerogen types, transport calculations, and computational models of methane/water and methane/carbon dioxide competition for binding sites in kerogens. The results presented here show that mature kerogens have more anisotropic diffusion pathways than immature kerogens and that it should be easier to recover methane from kerogen types with higher methane diffusivities and when the kerogens have the physical space required to swell since the flexibility of the kerogen network seems key to enabling methane diffusion. The latter point is particularly important given the known volume expansion of shales due to water uptake by clay minerals, which may alter the pore

network and kerogen density/porosity.[4] Ultimately, a detailed molecular-scale understanding of methane-kerogen interactions from this and future studies using similar methods of constructing kerogen models will contribute to practical in-field solutions for increasing the methane recovery from kerogens in shales.

Chapter 5 Supercritical Carbon Dioxide Enhanced Natural Gas Recovery from Kerogen Micropores

The material presented in this Chapter was published in 2022 in Volume 62 of Journal of CO2 Utilization. Available online via: https://doi.org/10.1016/j.jcou.2022.102105.

5.1 Introduction

A net-zero emission future is vital in controlling global heating and preventing adverse climate disasters to come. Despite the increasing demand for renewable energy, it is projected that fossil fuels will remain the largest share in the global energy portfolio for many years. Of all the fossil fuels, natural gas consisting of mainly methane (CH_4) is considered the cleanest, generating less air pollution and greenhouse gas emissions when burnt in the same quantity as coal and petroleum. In recent years, significant effort has gone into exploring unconventional sources of natural gas such as shale gas, tight gas, and coalbed methane (CBM).[2,3] To date, a significant amount of source rock reserves have been discovered, of which 647.95 trillion m^3 of shale gas are technically recoverable,[6] and successful commercial exploitation could help to alleviate a potential energy crisis. The combination of both horizontal drilling and hydraulic fracturing techniques has accelerated the production of shale gas and coal seam gas, however, unconventional gas production still faces a low recovery rate of 20% or less and CH_4 emissions are at least 30% higher than that of conventional natural gas reserves.[19,155,222,223] To reach these yields, chemical additives are introduced into hydraulic fracturing fluids in the amount of 0.05-1.5 wt% of the total hydraulic fracturing fluid. Though these are seemingly small quantities, a substantial amount of additives are used over the full lifetime of a well (150-600 m^3). There is very little published data regarding the composition or identity of the chemical additives used owing to trade secret protection. The US EPA has identified over 1000 chemical substances that have been used as chemical additives between 2005 and 2013.[224] The FracFocus database[225] indicates that chemical additives that may eventually break down to perfluoroalkyl and polyfluoroalkyl substances (PFAS), also known as “forever

chemicals", have been used commercially since 2011. The impacts of these additives on human health and biodiversity in the environment remain largely unknown, through preliminary studies suggest those additives can cause developmental and reproductive harm to mammals.[20,21] In order to achieve a long-term safe and sustainable production whilst achieving global climate targets over the coming decades, i.e., net-zero emissions, it is vital to eliminate or replace the toxic chemical additives used in hydrofracking fluids.

One method that could eliminate the use of water-based fluids and the additives they require is the use of supercritical CO_2 as a means of enhanced gas recovery (EGR) that may or may not be coupled with geological CO_2 sequestration (GCS).[41–45] Techniques such as CO_2 injection[226–229] and liquid CO_2 fracturing[230] can be used to deliver CO_2 into unconventional reservoirs. The latter has shown great promise with an increased extraction efficiency by up to 50%, whereas traditional hydraulic fracturing extraction is often hindered by the formation of ordered water in the micro and mesopores, causing low gas productivity.[11,12] Thus far, CO_2 injection-based EGR has yet to be developed to its fullest potential, and doing so requires that we learn more about the molecular-scale behaviours that influence gas recovery and the gas recovery mechanisms; a vital step towards achieving economic viability of a CO_2-based process.[231]

Methane exists in various dynamic fluid states within the shale micropores, i.e., free (in fractures and pores), adsorbed (surfaces of shale matrix), and dissolved (absorbed within organic matter like kerogen) states.[22,177,232] It has been established that the adsorbed gas dominates the total gas in place (GIP) – up to 85% of the GIP is adsorbed CH_4.[233,234] Adsorbed gas is located mainly in the organic parts of the shale matrix that are dominated by waxy substances known as kerogen.[216,235–239] A comprehensive introduction to kerogens can be found in **Chapter 4**. Several experimental and theoretical studies have demonstrated that kerogen or proxies of it (e.g., carbon nanotubes (CNTs), graphite, and etc.) preferentially adsorb CO_2 over CH_4,[26–40] though the mechanisms that underpin gas recovery are not fully understood. Probing the phase behaviour of fluids in confined kerogen

micropores poses a challenge for experimental studies, as do the length and time scale involved for time-dependent dynamic processes such as competitive adsorption and gas displacement at the nanoscale. Molecular simulations have become one of the most popular methods to provide molecular-scale insight into fluid–kerogen interactions, complementing experimental observations.[28,240] In recent years, atomistic simulation techniques such as grand canonical Monte Carlo (GCMC)[178,184,241] and molecular dynamics (MD)[176,181,182,187,242] have been used to study fluid adsorption and diffusion/transport in model shale matrices. The hybrid GCMC/MD simulations[175,186,243] has advanced our understanding of adsorption in shale by taking into account sorption-induced strain. A great deal of literature has been reviewed in our recent study[244] examining various packing procedures to generate kerogen matrices of different maturity levels and the effects the packing procedure has on the CH_4 diffusion behaviour. In the remainder of this introduction, we will focus on recent progress made modelling CO_2-EGR in kerogen systems.

In 2017, Sun et al.[29] offered molecular insights into CH_4 displacement by CO_2 injection in a 21 Å wide slit-shaped nanopore of mature kerogen developed by Collell et al.[245] They reported higher CO_2 adsorption capacities compared to CH_4 in kerogen. They also show that the fluid diffusion rate is slowest for pores within the kerogen matrix < internal surface of slit pore < central pore region due the varying degree of fluid interactions with the kerogen pore surfaces. CH_4 and CO_2 adsorption energies on the surface of the kerogen fragments showed that CH_4 has a weaker interaction with the kerogen surfaces compared to that of CO_2. In addition, the former has been shown to adsorb relatively uniformly across the kerogen surface, whereas the latter adsorbs more strongly to hydroxyl groups. Through *NVT* MD simulations at varying bulk CO_2 pressures between 6–20 MPa, they demonstrated that the higher the bulk pressure, the higher the CH_4 recovery rate, reporting a maximum recovery of 84% at 20 MPa. Importantly, their result shows that a small amount of CH_4 adsorbed within the matrix remained unrecoverable. Through simulated annealing, Pathak et al.[242] showed the sorption induced volumetric strain of a kerogen matrix made up of 15 Type II-C kerogen molecules when exposed to a total of 750 molecules of CH_4 and/or CO_2

at 400 K and 300 atm. They found that the diffusion coefficient of CH_4 is an order of magnitude higher than that of CO_2 and that CH_4 imbibition resulted in swelling of the kerogen matrices. However, replacing the CH_4 with CO_2 led to shrinkage of the kerogen matrix volume of 75% or higher. They suggested that a greater volume of CO_2 must be injected than the GIP to ensure the kerogen matrix does not deform. More recently, Babatunde et al.[246] modelled CH_4/CO_2 adsorption in shale through GCMC simulations using a slit-shaped nanocomposite made of 60% clay minerals (montmorillonite and illite), 10% Type II-D kerogen and 30% quartz. The proposed shale model was found to have a superior adsorption capacity and surface area compared to that of its individual components. Their results also match those observed in earlier studies where CO_2 exhibits a stronger affinity for adsorption than CH_4 on the kerogen components and confined fluids are predominantly in adsorbed state rather than as free gases. In the same vein, Huang et al.[247] studied the fluid states (adsorbed, dissolved, and free) of CH_4 and CO_2 in a confined wet shale environment using an organic-inorganic nanocomposite consisting of Na-montmorillonite sheets and Type I-A kerogen clusters made up of three kerogen molecules. Through hybrid GCMC-MD simulations at 338 K, they quantitatively determined the dynamic distributions of the fluid states of CH_4 and CO_2 during a three-stage shale gas recovery process (initial pressure depletion from 200 to 96 atm, subsequent CO_2 injection at 113 atm, and final pressure depletion from 113 to 96 atm) whilst permitting structure relaxation of the nanocomposite. They uncovered the trend that pressure depletion stages produce mainly free CH_4 whereas CO_2 injection mostly displaces the CH_4 adsorbed within the kerogen. Zhang et al.[248] investigated the competitive adsorption of CO_2 and CH_4 in both silicalite-1 (zeolite) and Type II-D kerogen (organic matter) using GCMC simulations between 300-425 K and fluid pressures up to 45 MPa. They showed that both adsorbents exhibit high affinity towards CO_2, with kerogen showing the largest preference for CO_2 and the highest CO_2/CH_4 selectivity. In a follow up study,[249] they reported that the adsorption of CH_4 and CO_2 becomes less favourable in the presence of water, however, the strong interactions between CO_2 and kerogen allow the CH_4/CO_2 replacement process to proceed.

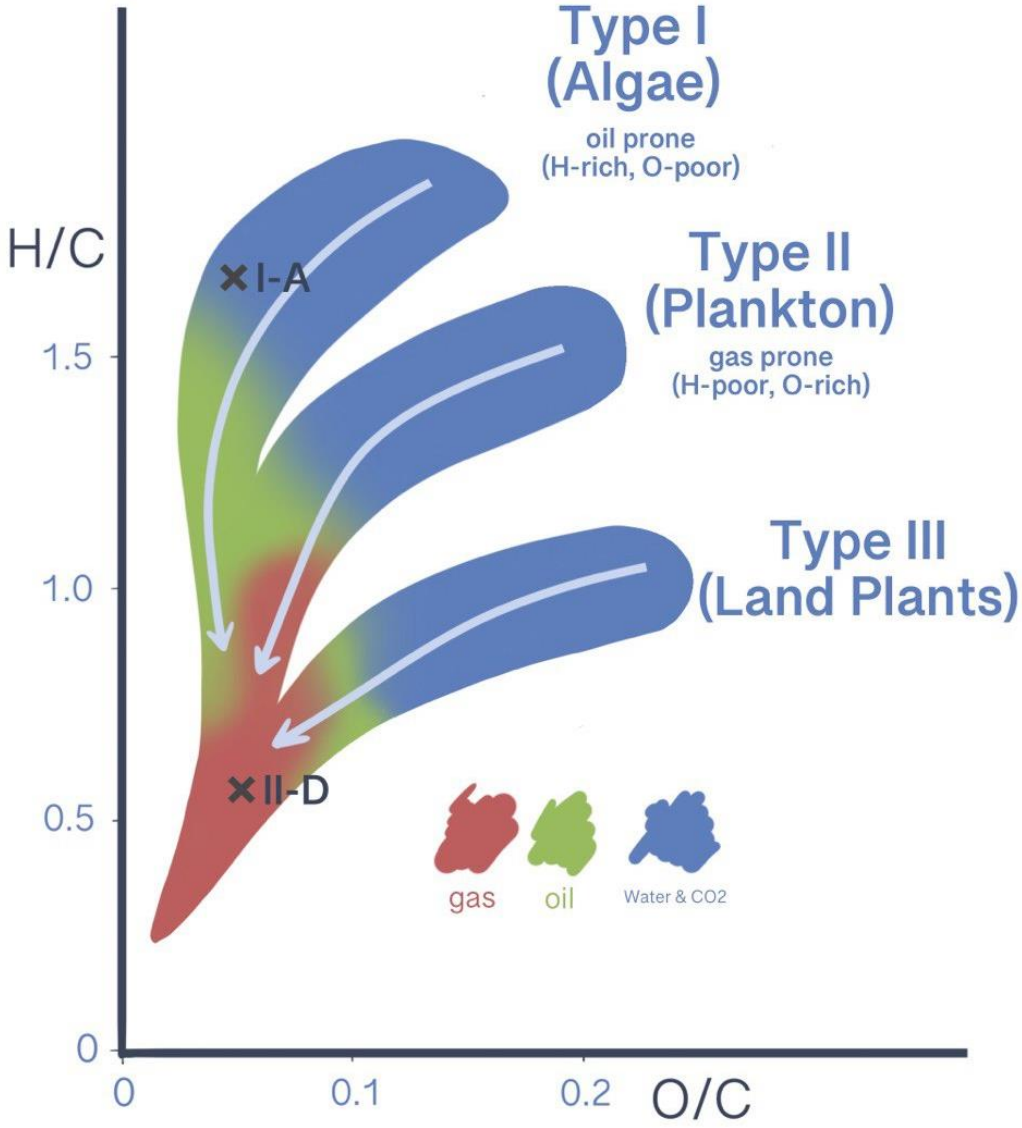

Figure 5.1: van Krevelen diagram.[25] The crosses mark the kerogen types investigated in this work. Adapted with permission from Yu et al.[244] Copyright 2022 American Chemical Society.

Using graphite and a model Type II-D kerogen matrix, Li et al.[250,251] utilised GCMC simulations to probe the adsorption behaviours of pure CH_4 and binary mixture of CH_4/CO_2 in environments with varying salinity (up to 6 mol/L NaCl), moisture content (up to 5 wt% H_2O) and ethane (up to 5 wt% C_2H_6). They noted that the presence of other compounds inhibits the adsorption of CH_4, with the greatest inhibition at the highest C_2H_6 concentration. Despite the negative impacts on CH_4 loading, the presence of said compounds improves the CO_2/CH_4 selectivity, which could facilitate EGR. More recently, Zhou et al.[252] presented the wettability transition mechanisms on the surface of model Type II-D kerogen (low oxygen content) through 5 ns long MD simulations in *NVT* ensemble and the supporting DFT calculations. They outlined that at low CO_2 pressures, the kerogen surface is likely to be water-wet and the transition into CO_2-wet state occurs at high CO_2 pressures, hindering capillary trapping of CO_2, which makes CO_2-EGR favourable.

Overall, these studies offer valuable insights into the adsorption process as well as the CO_2 for CH_4 gas displacement to a certain degree. However, they do not offer a detailed picture describing the CH_4 displacement mechanisms during the CO_2 injection process. Stochastic non-physical moves are sampled during GCMC simulations, such as particle deletion and reinsertion. While these enable equilibrium to be reached quickly at a given bulk chemical potential, they do not allow the system to evolve over time, meaning that time-dependent properties such as diffusion and displacement/replacement kinetics cannot be quantified. Furthermore, some of the MD studies that do capture time-dependent behaviour suffer from a short simulation time that may not represent the equilibrium state of the system. We investigated CH_4 adsorption and diffusion in kerogens of different types and maturity levels using GCMC and equilibrium MD methods in **Chapter 4**.[244] The results show that each individual kerogen matrix exhibits unique physical characteristics such as CH_4 loading, pore size distribution, and helium accessible volume. In addition, this work shows that CH_4 diffuses faster in both immature Type I-A (high H/C ratio) and overmature Type II-D (low H/C ratio) kerogens as compared to the other kerogen types.

In this study, we set out to gain a better understanding of the mechanisms and kinetics of in-situ replacement of CH_4 by CO_2 in model kerogen systems using a constant chemical potential molecular dynamics (CμMD) approach. CμMD works by employing self-adjusting bi-directional bias forces to control the chemical potential of fluids in designated volumes. This way non-equilibrium modelling of concentration-driven processes can be carried out. The CμMD method was first demonstrated to study crystal growth/dissolution at constant solution concentration.[253,254] Then it was extended to research gas transport and separation in porous membranes. This was achieved by maintaining two control volumes of different fluid concentrations at the feed and permeate sides, thereby creating a concentration gradient across a membrane that facilitates the diffusion of molecules.[255,256] Using CμMD, Loganathan and co-workers[257] showcased adsorption of CH_4 and CO_2 onto the surfaces of Na-montmorillonite when exposed to fluids external to the slit-pore at constant reservoir composition. In this work, we used the CμMD technique to understand the recovery mechanisms of CH_4 from organic matter (kerogen) when it is injected with supercritical CO_2. In the CμMD simulations, kerogen slabs pre-adsorbed with CH_4 were exposed to supercritical CO_2. This allowed adsorption kinetics of CO_2 and the consequent desorption of CH_4 to be quantified at constant thermodynamic driving force. In addition, we also provided a contrast between the recovery rate of CH_4 in both immature (Type I-A) and overmature (Type II-D) kerogens (see Figure 5.1) by mimicking the real ERG process via CO_2 injection.

5.2 Methods

5.2.1 Construction of Kerogen Slabs

The kerogen slabs used in this study were based on bulk kerogen matrices created in our earlier study.[244] Type I-A (M_w = 3805.1 g/mol, ρ = 0.964 ± 0.004 g/cm^3) and Type II-D (M_w = 2468.8 g/mol, ρ = 1.119 ± 0.060 g/cm^3) kerogen macromolecules were designed by Ungerer et al.[171] based on Green River Shale and Duvernay Shales, respectively. Firstly, we used three matrix structures for Type I-A and Type II-D kerogens from our previous study. Then, we loaded the structures with CH_4 based on estimates from earlier GCMC

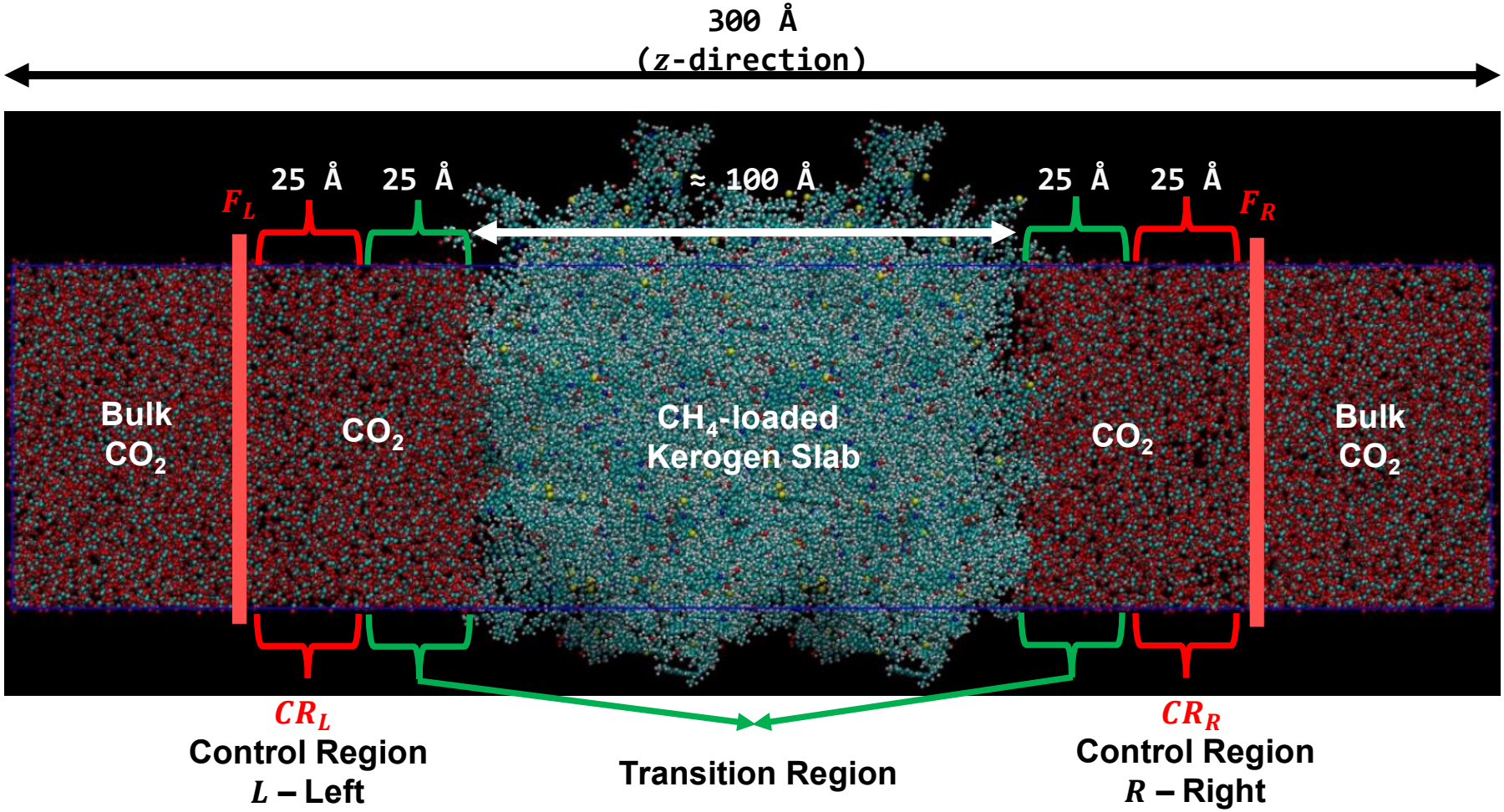

Figure 5.2: The initial configuration of the CH_4–CO_2 kerogen systems, where external forces (F_L and F_R) were applied on both sides to maintain constant chemical potential in the control regions (CR_L and CR_R).

simulations through the RASPA molecular simulation package.[200] In order to create the kerogen slabs, we first replicated the CH_4-loaded kerogen matrices two times in the z-direction, such that the resulting slabs were roughly 10 nm thick in the z-direction, while retaining their x and y dimensions. The kerogen slabs were then centred in a simulation box 30 nm-long in the z-direction, while maintaining the other directions to the same x and y-dimensions as the original kerogen matrices. The remaining void regions of the box were then filled with supercritical CO_2. Figure 5.2 shows the initial configuration of CH_4–CO_2 kerogen systems.

5.2.2 Simulation Settings

All MD simulations were performed using GROMACS 2020.4 molecular dynamics simulation software,[137] which was patched with a modified PLUMED version 2.7.1[258,259] to enable CμMD within the NVT ensemble. Newton's equations of motion were integrated with a time step of 1 fs via the leapfrog algorithm. To control the system temperature, Nosé–Hoover thermostat[57,58] with a coupling time of 0.5 ps was used. The interatomic potentials for the flexible kerogen slabs were obtained from CVFF.[195] The CH_4 and CO_2 molecules were represented by the TraPPE-UA[134] and EPM2-based[260] models, respectively. Short-range non-bonded interactions were described through Lennard–Jones (LJ) potentials. Lorentz-Berthelot mixing rules were used to calculate the LJ interactions of unlike atom pairs in different kerogen macromolecules or further than three bonds of the same macromolecule. Long ranged Coulombic interactions were calculated using a smooth particle mesh Ewald (PME) method[138] of a fourth order polynomial with a mesh width of 0.12 nm. In all simulations, periodic boundary conditions were imposed in all three directions. A cut-off radius of 1.4 nm was used for both the LJ interactions and the real part of the Ewald summation. Dispersion corrections for long range van der Waals interactions were not applied to energy or pressure. The width of the transition regions, control regions, and bias force regions, which are shown in Figure 5.2, were set to 2.5, 2.5 and 0.25 nm, respectively. The target density of CO_2 in the control regions was set to reproduce the density of CO_2 at 365 K and 275 bar, mimicking reservoir-relevant conditions, at roughly

9.0916 CO_2 molecules per nm^3. The target density of CO_2 in the control regions were maintained by using the force constants, $F_L = F_R = 10{,}000$ kJ nm^3 mol^{-1}, which were applied at the centre of the bias force regions (Figure 5.2). The concentration of CO_2 in the control regions were monitored over the course of the simulations at intervals of 0.5 ps to ensure the density of CO_2 remains close to the target value. To prevent any shift of the kerogen slabs, we defined a freeze region of 0.5 nm thick in the middle of the simulation box, in which the motion of the kerogen atoms was frozen in the z-direction only. This setup allows the simulation of a symmetric adsorption/desorption process, where the in-place CH_4 is being extracted and replaced by the injection of CO_2. All simulations were carried out at 365 K and for 200 ns in the case of Type I-A and 400 ns for Type II-D kerogen systems. Sample input files, including force field parameters and initial configurations, can be obtained online. Details on how to incorporate the CμMD method within PLUMED is available on GitHub (via https://github.com/mme-ucl/CmuMD).

5.2.3 Adsorption/Desorption Kinetics and Diffusion of CH_4 and CO_2 in Kerogen

Adsorption is a three-step process, which first involves two mass transport steps external to the adsorption surface (film diffusion and subsequently intraparticle diffusion) and finally surface reaction on the internal surface of the adsorbent. The adsorption rate is the sum of all three steps.[261] In order to describe the enhanced gas recovery process, kinetics modelling was applied to predict the rate of CO_2 adsorption and CH_4 desorption from kerogens as a function of time. Classical kinetics models, namely, pseudo-first order (PFO) and pseudo-second order (PSO) were used to fit the uptake and desorption profiles of CO_2 and CH_4, respectively.[262,263] The linearised forms of the models were provided in Ho and McKay's work.[264] A linear fit can be obtained by plotting $\ln\frac{Q_e}{Q_e - Q(t)}$ vs t and $\frac{t}{Q(t)}$ vs t for PFO and PSO, respectively, where $Q(t)$ is the adsorbate adsorbed at given time, t, or at equilibrium, Q_e. The rate coefficient, k, and equilibrium loading, Q_e, can then be estimated through the slope and intercept of the line of best fit. There is very little consensus regarding the validity of the PFO model, some[265,266] argued it is valid at the initial stage, where the initial concentration is high, while others[267,268] at the final stage of adsorption

(near equilibrium). In the case of the PSO model, its superiority compared to the PFO model and wide applicability during adsorption has been reported in the literature.[261] In this study, we compared both the PFO and the PSO models to assess the quality of the fits through the coefficient of determination, R^2, and estimated the adsorption kinetics and/or equilibrium loading amount of CH_4 and CO_2 in Type I-A and Type II-D kerogens.

Gas transport in shale primarily occurs through diffusion, which influences gas recovery as well as the kinetics of the recovery process.[22] In order to improve our understanding of gas transport, we calculated the mean square displacement (MSD) of adsorbed CO_2 in both Type I-A and Type II-D kerogens in the last 50 ns of the simulations. Moreover, the MSD for inaccessible and recovered CH_4 were calculated at the initial (50-100 ns) and final (last 50 ns) stages for Type II-D kerogen systems. The final frames of each simulation were analysed, only CO_2 molecules that have penetrated deeper than 10 Å from the outermost atoms belonging to the kerogen slab at both ends are considered to be in an adsorbed state. In the same way, any remaining CH_4 molecules in Type II-D kerogens are deemed to be in isolated pores or otherwise recovered.

5.3 Results and Discussion

5.3.1 Kerogen Swelling

An earlier study by Pathak et al.[242] suggested that CH_4 replacement with an insufficient amount of CO_2 may lead to kerogen deformation. To assess sorption induced volumetric strain upon CH_4 displacement, Figure 5.3 compares the z-density profiles of kerogen slabs before and after simulation in various runs. The z-density profiles of Type I-A and Type II-D kerogen show that Type I-A swells in the z direction more than Type II-D as CH_4 is displaced by CO_2. Initially, the CH_4-loaded Type I-A kerogen slabs have smooth density profiles, whereas the density profiles of CH_4-loaded Type II-D kerogen slabs show large fluctuations indicative of a less homogenous structure in Type II-D (Figure 5.3, orange lines). Swelling in the z-direction is observed in the width of the density profile for both kerogen types after CO_2 adsorption and CH_4 desorption (Figure 5.3, green lines). The

swelling is more significant in Type I-A kerogen and is reflected in both the density and the slab width. Comparing the density profiles of CH_4 and CO_2 in the *z*-direction in Type

(A) Type I-A

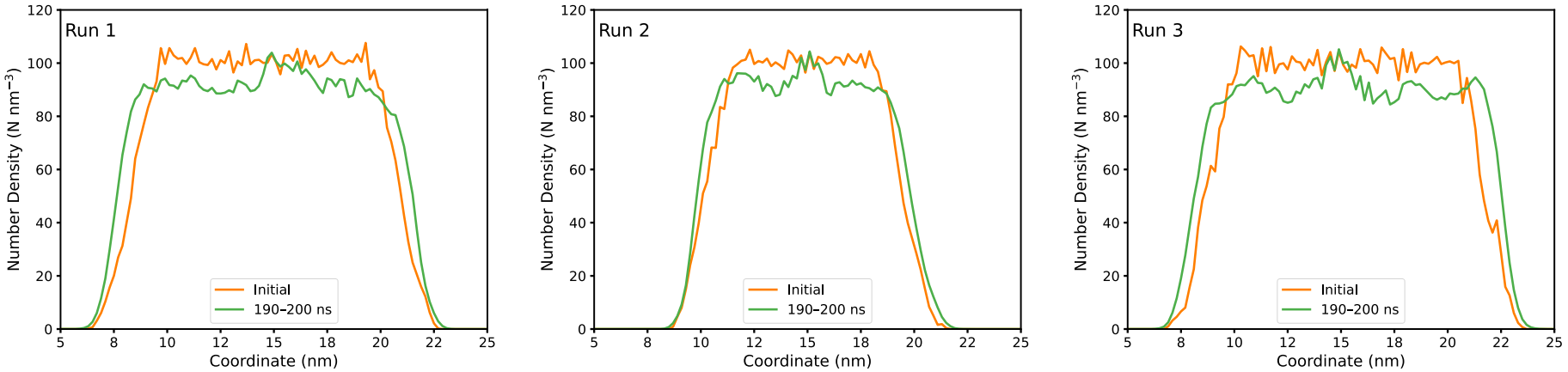

(B) Type II-D

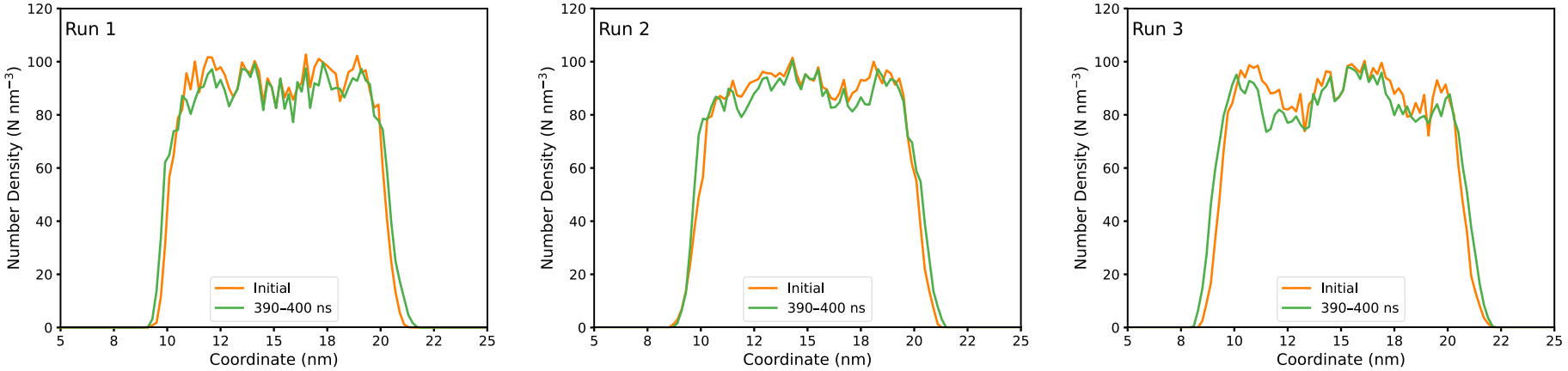

Figure 5.3: Density profiles (z-direction) of kerogen slabs in various simulation runs for a) Type I-A and b) Type II-D kerogens.

Type I-A

(A) CO_2

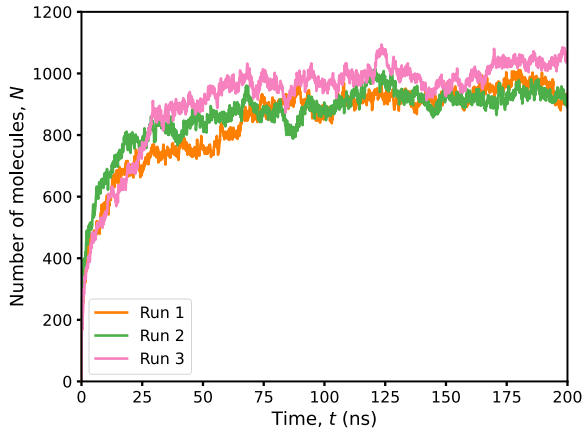

(B) CH_4

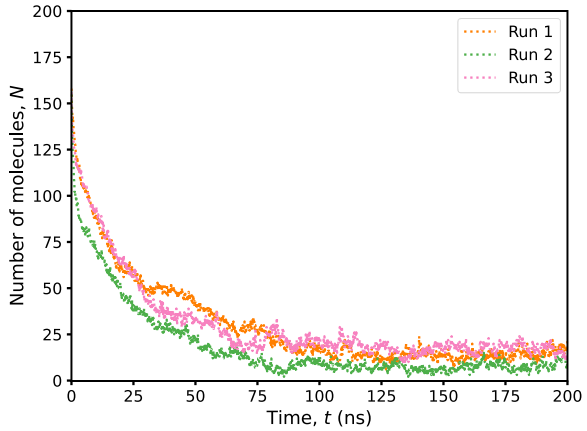

Type II-D

(C) CO_2

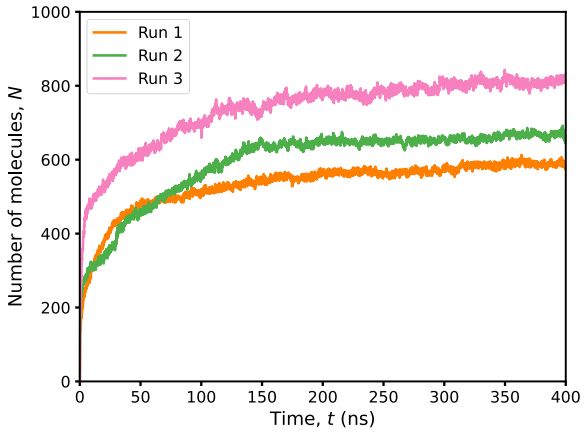

(D) CH_4

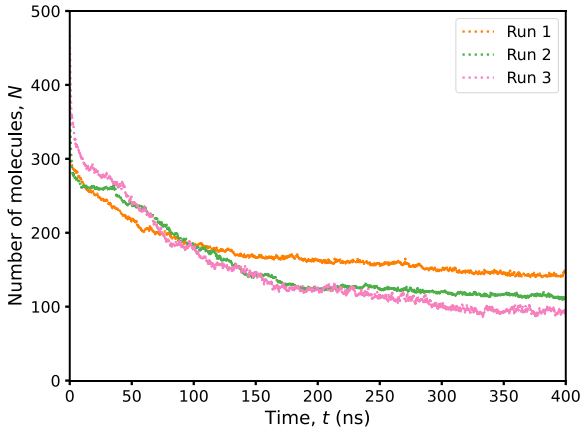

Figure 5.4: CH_4 and CO_2 loadings over time in various kerogen slab samples

Adsorbed CO_2

(A) Type I-A (150 – 200 ns)

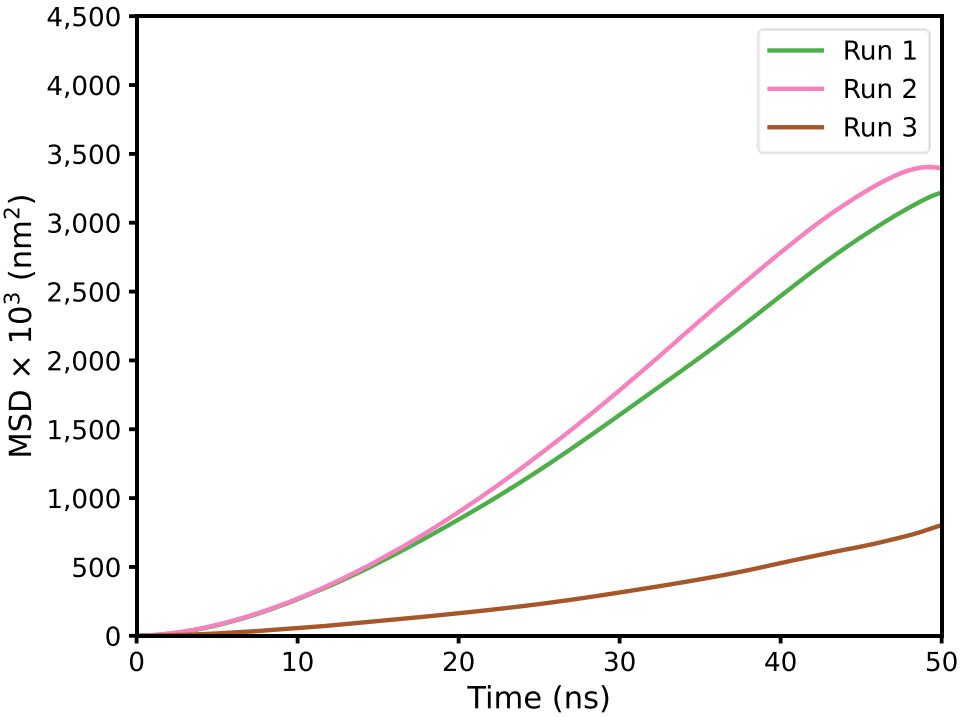

(B) Type II-D (350 – 400 ns)

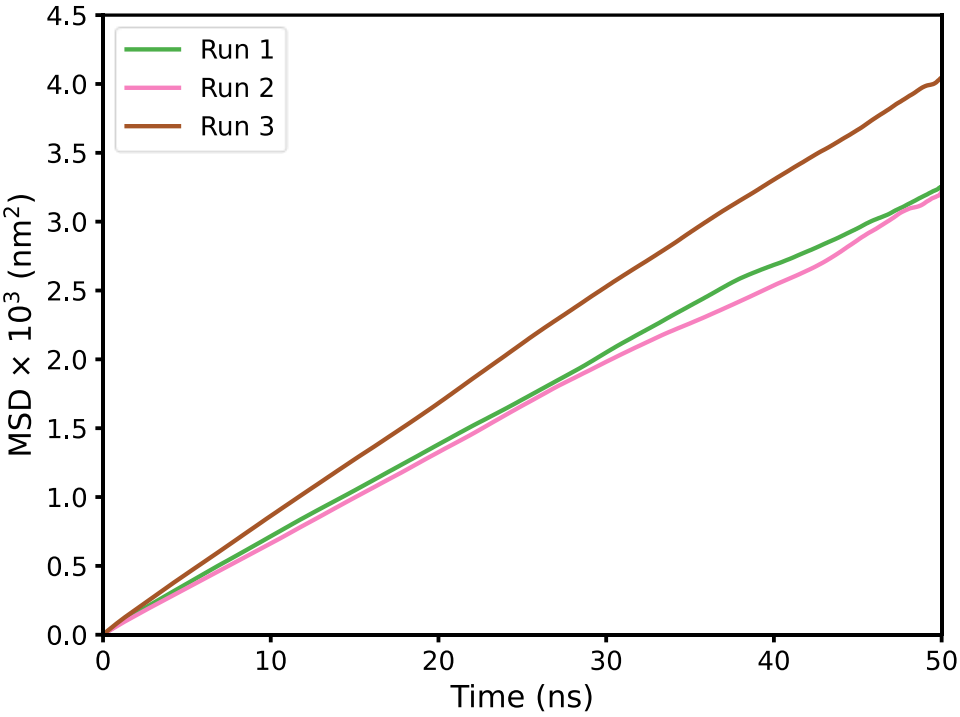

Figure 5.5: The MSD plots of adsorbed CO_2 in Type I-A and Type II-D kerogens in the last 50 ns of various simulation runs.

I-A and Type II-D kerogens shows that the CH_4 density in the kerogen slabs decreases over time while the CO_2 density increases (Figures Figure C1 and Figure C2). The final density profiles for CO_2 in Type I-A kerogen slabs appear similar and have final CO_2 densities that fluctuate around 5 CO_2 molecules/nm^3. The huge variations in density across the z-direction for Type II-D kerogens highlight the structural heterogeneity, which could arise from the preferential parallel stacking arrangement of Type-D kerogen macromolecules.[189] We also observe that, up on CO_2 adsorption, Type II-D kerogens retain more CH_4 than that of Type I-A, suggesting that CO_2 either cannot access or cannot effectively compete with CH_4 for some adsorption sites in the kerogen structures.

5.3.2 CH_4 Recovery in Kerogen Through Supercritical CO_2 Exposure

Figure 5.4 shows the evolution of CO_2 and CH_4 loadings in Type I-A and Type II-D kerogens as a function of the simulation time. In general, CO_2 is adsorbed more quickly than the CH_4 is desorbed, with the system attaining equilibrium in approx. 100 and 150 ns for Type I-A and Type II-D kerogens, respectively. Looking at Figure 5.4, it is apparent that there are two distinct stages for CO_2 uptake, an initial rapid increase and followed by a more gradual uptake before reaching a plateau. Together, the data suggest that the kinetics of CO_2 adsorption is faster in Type I-A than in Type II-D kerogen. Indeed, MSDs of adsorbed CO_2 molecules in Type I-A and Type II-D computed in the last 50ns of the simulations show that CO_2 diffuses two to three orders of magnitude faster in Type I-A kerogens compared to that of in Type II-D kerogens (Figure 5.5). This suggests that in Type I-A kerogens pores are better connected compared to in Type II-D kerogens. In the case of CH_4 desorption, there is a gradual continuous decrease in CH_4 loading over time, which asymptotically approaches a very low equilibrium loading. Indeed, when the number of CH_4 molecules that remain in Type I-D and Type II-D kerogens at the end of the simulations are compared against the initial number of CH_4 molecules, one can see that in Type I-A kerogen, almost all CH_4 molecules are replaced by the adsorbed CO_2 molecules; whereas, in Type II-D kerogen a significant fraction of the CH_4 molecules still remain

adsorbed. This clearly indicates that in Type II-D kerogens, there are CH_4 molecules in isolated pores that are inaccessible to diffusing CO_2 molecules.

Table 5.1 provides a summary of CH_4 recovery when the kerogen slabs of different maturity levels were exposed to supercritical CO_2. While both kerogens take up more CO_2 molecules than the methane molecules they release, Type I-A kerogen takes up much more CO_2 per initially adsorbed methane than Type II-D. We observe that the inaccessible CH_4 molecules; i.e, those not replaced by CO_2, in Type II-D are an order of magnitude more than the same in Type I-A kerogen. According to the date in Table 1, one CH_4 molecule was replaced by two CO_2 molecules in Type II-D kerogen, whereas in Type I-A kerogens, the replacement ratio is approximately six CO_2 molecules for one CH_4 molecule. Further analysis also shows that CO_2 is most effective at recovering CH_4 in Type I-A with a recovery factor of at least 90%. For Type II-D kerogen, the recovery factor is in between 65-83%.

Table 5.1: Number of CH_4 and CO_2 molecules in the kerogen slabs in various simulation runs and the corresponding CH_4 recovery factor and replacement ratio.

Kerogen	Run	CH_4			CO_2	CH_4 Replacement Ratio
		Initial	Final*	Recovery Factor (%)	Final*	
Type I-A	**1**	170	15	91.18	958	6.18
	2	170	8	95.29	932	5.75
	3	164	17	89.63	1040	7.07
Type II-D	**1**	394	142	63.96	588	2.33
	2	426	114	73.24	668	2.14
	3	502	93	81.47	810	1.98

* Averaged over the last 5 ns

Table 5.2: Parameters of the linear fit for the PSO kinetic model.

Run	Q_e (mmol/g) *				k_2 (g (mmol ns)$^{-1}$)			
	Type I-A		Type II-D		Type I-A		Type II-D	
	CH_4	CO_2	CH_4	CO_2	CH_4	CO_2	CH_4	CO_2
1	0.0313	2.6317	0.5620	2.4618	-1.4057	0.0351	-0.0816	0.0255
2	0.0160	2.5130	0.4344	2.8573	-3.3487	0.0720	-0.0765	0.0162
3	0.0392	2.8012	0.3550	3.4152	-1.3601	0.0414	-0.0673	0.0172

* To convert no. of mmol of fluid per g kerogen to no. of fluid molecules per kerogen slab, which contains 100 kerogen macromolecules, one needs to multiply the Q_e value by $\frac{M_w}{10}$, where M_w is the molecular weight of the respective kerogen macromolecules.

This inconsistency may be due to the random packing procedure we used to prepare the underlying kerogen matrix, where structural heterogeneity may emerge.[244] We also observe that the rate of CH_4 desorption in Type II-D systems is at least 3 times faster than CO_2 adsorption rate. It is widely accepted that CO_2 has a higher affinity towards kerogen than CH_4. The lower adsorption rate of CO_2 when compared to CH_4 suggests that diffusion might play a more important role in setting the overall rate than the actual adsorption process at the surface. It can thus be suggested that the CH_4/CO_2 replacement process could be a diffusion-controlled process. The low statistical noise for Type II-D methane desorption is a result of the comparatively small numbers of residual methane molecules in Type I-A kerogen, leading to large fluctuations in the curve at longer times. Furthermore, we applied the PFO model to obtain the 1st order rate coefficient (k_1) for CO_2 adsorption in kerogens as shown in Figure C5. It can be seen from Figure C5 that the quality of fit for the PFO model are subpar as compared to the PSO model (Figure C4). Since the R^2 values for the fits were all below 0.5, it can be concluded that the PFO model is not suitable for modelling adsorption kinetics for the systems we investigated. CH_4 displacement being well-fit by a PSO process suggests that the rate limiting step in the displacement mechanism is a bimolecular process, though it is unclear what specific species are involved (e.g., two CH_4 molecules vs. one CH_4 and one CO_2).

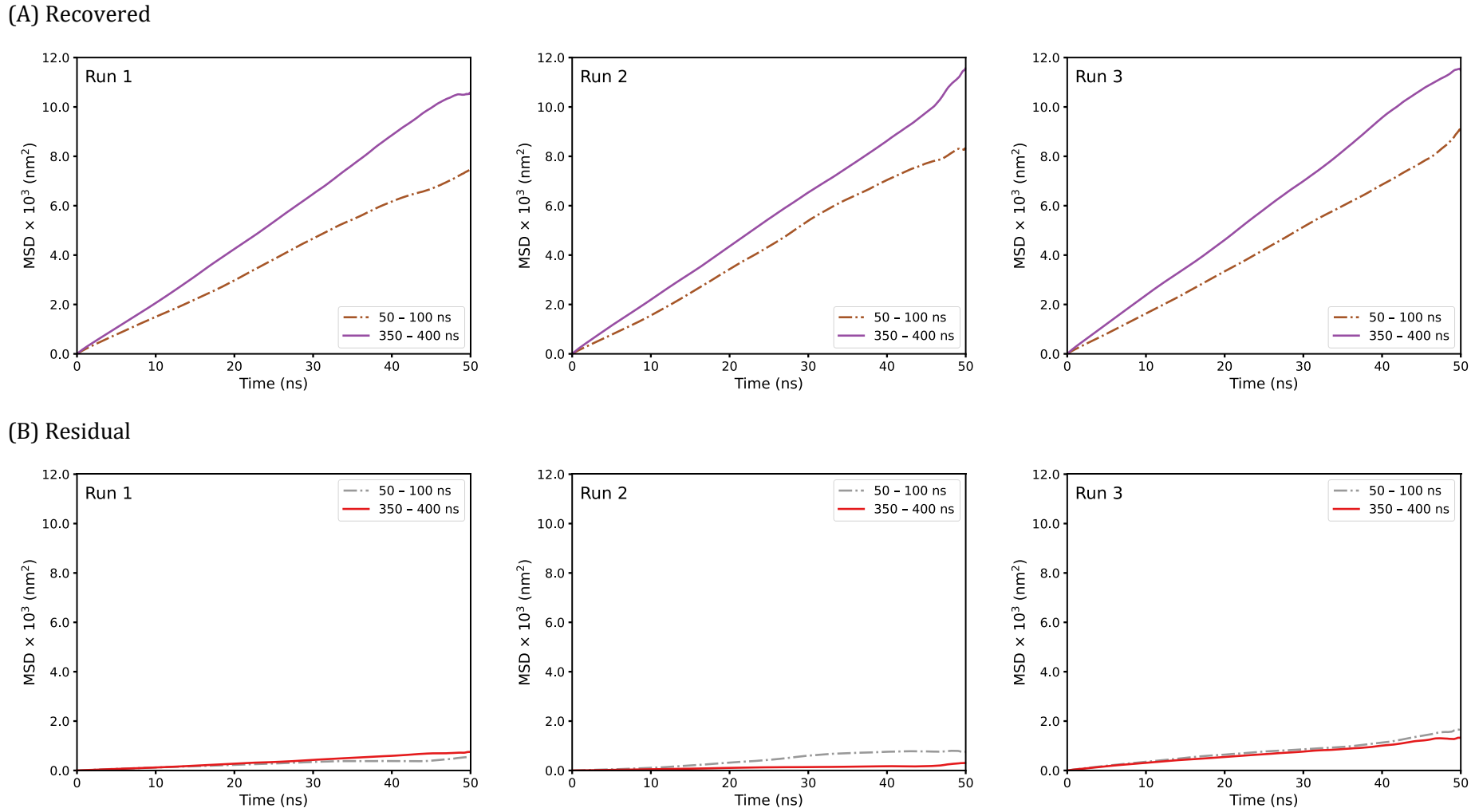

Figure 5.6: The MSD plots of recovered and isolated CH_4 in Type II-D kerogen at the initial (50-100 ns) and final (350-400 ns) stages of various simulation runs.

5.3.3 Analysis of Inaccessible CH_4 in Type II-D Kerogen

We earlier mentioned that in Type II-D kerogens a fraction of the CH_4 molecules remain trapped despite being exposed to supercritical CO_2. To provide a contrast between recovered and trapped CH_4 molecules in Type II-D kerogens, we computed their used MSD profiles separately. We did this by assigning different labels to the CH_4 molecules that remain in and outside the kerogen slabs at the end of the simulations; i.e. recovered and residual, respectively. It is worth pointing out that the initially adsorbed CH_4 molecules in Type I-A kerogens were almost completely replaced by CO_2 molecules and hence not included in this analysis. Figure 5.6 compares the MSDs of CH_4 molecules in Type II-D kerogen systems. There are two important differences between the recovered and residual CH_4. One, the recovered CH_4 molecules display about an order of magnitude faster diffusion rate as compared to residual CH_4 molecules in the kerogen slabs of Type II-D at any stage of the simulations; and two, at the beginning of the simulations (50-100 ns), where the adsorbed CH_4 content is still high, the MSD of recovered CH_4 is lower than that of recovered CH_4 towards the end of the simulations (350-400 ns), where all recovered CH_4 molecules are outside the kerogen. This is because at the earlier stages, the recovered CH_4 molecules are still in the kerogen matrix where the diffusion is slower compared to that of outside the kerogen. On the other hand, the MSDs of residual CH_4 molecules offer a consistent pattern with no significant differences in magnitude regardless of the progression of the simulations. These observations imply that the residual CH_4 is in a highly constrictive environment, i.e., in narrowly confined pores, thereby inaccessible, and that CO_2 could only displace accessible CH_4 and that inaccessible CH_4 would remain unrecoverable in isolated pores. Comparing the MSDs of both adsorbed CO_2 and trapped CH_4 within Type II-D kerogen slabs, in Figure 5.5 and Figure 5.6, respectively, it is clear that the MSD profiles of the former is higher than that of the latter.

5.4 Conclusions

In this study, we investigated the kinetics associated with the use of supercritical CO_2 as a means of EGR and GCS through injection into CH_4-bearing organic matter, i.e., kerogen.

Kerogen in the environment exists at many maturity levels, and it is essential to assess the recovery of CH_4 at the start (immature) and end (overmature) of their lifecycle. This paper offers a comprehensive picture of how kerogen maturity and heterogeneity may impact gas recovery and also the challenges that may arise due to the difference in sorption kinetics. Through CμMD simulations carried out under reservoir-relevant conditions (365 K and 275 bar), this study shows that CO_2 injection can theoretically achieve 90% and 65% CH_4 recovery in Type I-A and Type II-D kerogens, respectively. For every CH_4 molecule being replaced, approx. 2-3 and 6-7 CO_2 molecules are being stored in Type II-D and Type I-A kerogens, respectively, where a minute swelling can also be observed during this process. The relatively large number of unrecovered CH_4 in Type II-D kerogens is due to the higher density and relatively low pore connectivity of the kerogen slabs, which contain CH_4 in isolated pores that remains trapped within those pores and therefore inaccessible by CO_2. The CO_2 adsorption process is well modelled by a PSO rate law, which is superior to the PFO model at fitting the CO_2 adsorption kinetics. Overall, rapid replacement kinetics can be observed in immature Type I-A kerogens, primarily as a result of fast fluid diffusion through the more porous and flexible slabs, whereas in Type II-D, the kinetics are considerably slower. To the best of our knowledge, this is the first study to quantify the kinetics of the replacement process, i.e., adsorption of CO_2 and the consequent desorption of CH_4, in kerogens. These kinetic models are tools of industrial importance, especially in process engineering, and can be used for predicting and optimising the EGR process, thereby improving performance, CH_4 yield, and process efficiency. A key strength of this study is the ability to monitor the replacement process in real time while maintaining a constant thermodynamic driving force. The present study lays the groundwork for future molecular level modelling research that can aid improve our understanding of EGR via CO_2 injection into kerogen to achieve net-zero emissions.

Chapter 6 Conclusions and Future Work

In this Chapter, the overall findings of this Thesis are presented as well as possible research trends that may arise due to the work presented.

6.1 Conclusions

This thesis is focused on understanding the unique properties of porous sedimentary environments found in natural systems, which have been shown to facilitate gas and energy storage in enormous quantities at the molecular scale. This research builds upon the concept of nature-inspired design, which draws lessons from natural systems to create innovative solutions to the UCL Grand Challenges. By investigating the potential of these porous environments for artificial energy and gas storage, this thesis aims to contribute to developing sustainable and efficient energy solutions inspired by nature. The peculiarity of confined fluids deviating from their bulk properties is a common observation. Unearthing the insights on the behaviour of fluids under confinement in natural settings could help the development of new and efficient industrial processes involving porous media, including but not limited to adsorption, catalysis, and separation. This Thesis set out to better understand the structure and dynamics of various fluids confined within the pore channel/network commonly found in nature via molecular modelling.

Natural CH_4, the primary component of natural gas, is poised to be the cleanest of all fossil fuels when combusted completely, resulting in 40% less CO_2 emissions. The abundant quantities of CH_4 are stored in the form of gas hydrates in porous sedimentary rocks deposited across the globe. By mimicking nature, the main goal of this study is to improve the understanding of CH_4 storage capacity in nanoporous solids via formation of artificial CH_4 hydrates, similar to those found deep-under-sea. In **Chapter 3**, *NPT*-EMD simulations were conducted to study CH_4 hydrate growth within a 50 Å wide slit-shaped hydroxylated silica pore at 2 °C, at varying pressures of up to 100 bar, mimicking . By utilising a direct phase coexistence approach, CH_4 hydrate phase was allowed to grow or dissociate,

depending on the pressure imposed, over 6 μs simulations from a three-phase configuration, consisting of a CH_4 hydrate crystal, liquid H_2O and CH_4 vapour slabs. While methane hydrate growth is typically unfavourable at low pressures, confinement can actually promote growth under milder conditions. Specifically, we observed that confinement enhances the concentration of CH_4 in water, which can facilitate the formation of hydrate clusters and ultimately lead to the growth of larger hydrate structures. In this case, the effect of pressure plays a part in determining the kinetics of hydrate growth, where the higher the pressure, the faster the growth of CH_4 hydrates. These findings have important implications for understanding the behaviour of CH_4 hydrates in natural gas hydrate deposits found in various geological formations. This observation could be particularly crucial in the exploration of natural gas reserves, where CH_4 hydrates could be present under low-pressure conditions. By understanding confinement conditions, it may be possible to extract CH_4 more efficiently and cost-effectively or even consider them as a potential storage solution for other greenhouse gases. Moreover, the study could also have implications for the development of hydrate-based gas storage and transportation systems that rely on CH_4 hydrates. Our findings could help inform the design of these systems and improve their performance by better understanding how CH_4 hydrates behave under confinement. Overall, this study provides valuable insights into the fundamental properties and behaviour of CH_4 hydrates under confinement and may help to inform future research in this area.

Apart from CH_4 hydrates, kerogens are known to contain a significant fraction of the CH_4 in shale-gas reservoirs and that the recovery of CH_4 from shale-gas reservoirs is quite low (~10%). What is unclear is why the recovery is so low and what we can do improve the recovery process. The solutions to both of these questions rely on a detailed molecular-scale understanding of CH_4 behaviour in shales and all shale components, including kerogen. The ability to extract kerogen and know the extracted kerogen has the same physical and chemical characteristics as kerogen in the native rocks is limited. Thus, computational approaches are likely key to developing a molecular-scale understanding of

what is happening in shale-gas reservoirs and will also be needed to help verify experimental data once the community at large is able to collect detailed experimental data for CH_4 adsorption and dynamics in kerogens. Thus, there is a pressing need to have good computational models of kerogens, to understand how to build realistic computational models of kerogens, and to do both of these for a broad range of kerogen types. In **Chapter 4**, EMD simulations were utilised to build realistic 3D kerogen matrices of six kerogen types of different maturity levels through simulated annealing. Our results showed that the densities of the packed structures are in good agreement with experimental data. The amount of in-place CH_4 adsorbed within the micropores of kerogen matrices was estimated via GCMC simulations at reservoir-relevant conditions, i.e., 365 K and 275 bar. Moreover, we also noted that the amount of CH_4 loading correlates positively with the aromatic content of the kerogen units. Our *NPT*-MD results show that CH_4 self-diffusivity exhibits some degree of anisotropy in all kerogen types examined here except for Type I-A kerogens, where diffusion is the fastest and isotropic diffusion is observed. In addition, CH_4 self-diffusivity appears to correlate positively with pore volume for Type II kerogens, where diffusivity increases with increasing maturity. Swelling of the kerogen matrices can also be observed upon CH_4 adsorption. This Chapter presents key operational rules for conducting such simulations and the first molecular-scale comparison of CH_4 dynamics in a broad array of kerogen types. We showed that mature kerogens are more anisotropic than immature kerogens and that it should be easier to recover methane from kerogen types with higher CH_4 diffusivities. Ultimately, a detailed molecular-scale understanding of CH_4-kerogen interactions will contribute to practical in-field solutions for increasing the CH_4 recovery from kerogens in shales. The insights gained from this study may assist in creating consistent calculations of thermodynamic and transport properties of fluids in a broad array of kerogen types after taking the model creation step into account, which can dramatically affect the physical properties (pore characteristics) of the resulting matrix structures.

In **Chapter 5**, we set out to assess the feasibility of recovering shale gas via CO_2 injection into CH_4-bearing immature (Type I-A) and overmature (Type II-D) kerogens using CμMD.

Supercritical CO_2 was injected into the kerogen slabs at a constant chemical potential mimicking reservoir-relevant conditions (365 K and 275 bar). This study has identified that, through kinetics modelling, the pseudo-second order (PSO) rate law can be used to describe the kinetics of the CH_4 recovery and CO_2 uptake in kerogens. The kinetics of sorption are rapid in Type I-A kerogen due to better connected pore volume facilitating fluid diffusion, whereas in Type II-D kerogen, its structural heterogeneity hinders fluid diffusion. Estimated second order rate coefficients reveal that CO_2 adsorption and CH_4 desorption in Type I-A are about two times and an order of magnitude faster, respectively, compared to those of in Type II-D. Furthermore, we reported up to 90 % and 65 % CH_4 recovery in Type I-A and Type II-D kerogens, respectively. Kinetics modelling demonstrated here could serve as a starting point for developing a highly accurate EGR model, incorporating more parameters, such as a wide range of operating conditions. Engineers can then simulate the behaviour of an EGR process through the use of process design and optimisation software. By inputting the relevant parameters (temperature, pressure or initial CH_4 loading) into such software, the model would be able to identify the optimal operating conditions, such as those that maximise CH_4 yield (including CO_2 storage), minimise energy consumption or reduce undesirable byproducts, such as gas hydrates from clogging the wellbore and preventing CH_4 recovery. Our in-depth analysis revealed that overmature kerogen contains inaccessible micropores, which prevent the full recovery of CH_4. In general, therefore, it seems that more CO_2 is required to recover a given amount of CH_4 whilst maintaining the structural integrity of kerogen slabs. These findings have important implications for the development of more efficient and sustainable methods for natural gas recovery from shale formations. The use of supercritical CO2 could potentially reduce the environmental impact of natural gas recovery by reducing the need for hydraulic fracturing, which has been associated with environmental concerns such as water pollution and seismic activity. Overall, this study should help with the development of CO_2-EGR processes as well as the potential use of shale as a medium for CO_2 sequestration.

6.2 Outlook

In **Chapter 3**, CH_4 hydrate growth under confinement was observed under a slit-shaped pore of approx. 50 Å wide, which is in the mesopore range. A natural progression of this work is to analyse the effect of the pore size, e.g., in the micropore range (< 20 Å) to uncover the impact of ultra-confinement or at a larger pore size until which the confinement effects become small and negligible. In addition, instead of a slit-pore, further modelling work will have to be conducted in order to determine the effect of pore geometry (cylindrical, tubular, etc.) on the behaviour of confined CH_4 hydrates. It is also essential to decouple the contribution of surface chemistry on CH_4 hydrate growth, i.e., the strength of water-substrate interactions, by using different functional groups of varying degrees of hydrophilicity, which has an indirect impact on the hydrate formation yield. Whilst these three parameters (size, shape, and surface chemistry) are the key parameters defining CH_4 hydrate formation in confined nanospace, future studies should also include comprehensive cage analysis to supplement the understanding of the formation mechanisms. Furthermore, more research is needed to reproduce the pore-confined phase behaviour of other gas hydrates of different guest molecules (hydrate formers), especially, CO_2 and H_2 as an essential step towards developing gas hydrate-based technology for carbon and energy storage, respectively. A future study investigating gas hydrate dissociation in confinement through the addition of additives like hydrate inhibitors would be very interesting. This will provide us with important insights regarding the feasibility of using artificial gas hydrate as a medium for natural gas transportation. Ultimately, a real-time CH_4/CO_2 replacement model using CμMD described in this Thesis would serve as a basis for understanding the recovery of CH_4 from natural gas hydrate whilst saturating the hydrate-bearing rocks with CO_2, forming artificial CO_2 hydrates for long-term CO_2 sequestration purposes.

The main goal of **Chapter 4** was to develop representative 3D kerogen models. However, in shale environments, kerogens co-exist with other inorganic compounds forming a complex heterogenous shale matrix. A further study could incorporate minerals like illite during the

annealing procedure and thus creating a representative 3D shale matrix, comparable to experimental data. It would be interesting to see how much of the diffusion behaviour of CH_4 would be affected. Similarly, there are many types of compounds entrapped in a shale matrix. By expanding the list of fluids of interest, e.g., H_2O, ethane (C_2H_6), propane (C_3H_8), and etc., we could accurately predict the amount of adsorbed fluids in shale matrices of varying mineral content. Furthermore, the chemo-mechanical coupling between adsorbed shale gas and the shale matrix because of sorption-induced strain can also be assessed. These suggestions also apply to our proof-of-concept study in **Chapter 5**, which showed that fast kinetics and high recovery of CH_4 can be obtained through supercritical CO_2 injection into pure kerogens. A number of possible future studies using the same modelling set up are apparent. For example, initially one could attempt to repeat the simulations and kinetics modelling over a wide range of possible operating conditions. As a result, a new EGR model can then be further developed to incorporate parameters, such as temperature and pressure. Furthermore, a kerogen slab located within a slit-shaped pore of illite could be used to as a proxy for a real shale matrix. It would be interesting to see how CO_2 would interact with the illite surfaces and the implication on CH_4 recovery in such a set up. Moreover, extracted shale often contains H_2O and NaCl in varying amount and it is still unclear how this would affect the CO_2-enchanced recovery process. More information on representative models of shale matrix would help us to establish a greater degree of accuracy on this matter. Ultimately, a commercially valuable EGR model capable of predicting gas recovery/storage over a wide range of distinctive reservoirs across the globe can be developed. Further studies are needed to better understand the potential environmental and economic impacts of this approach.

Appendix A

Supporting Information for Chapter 3

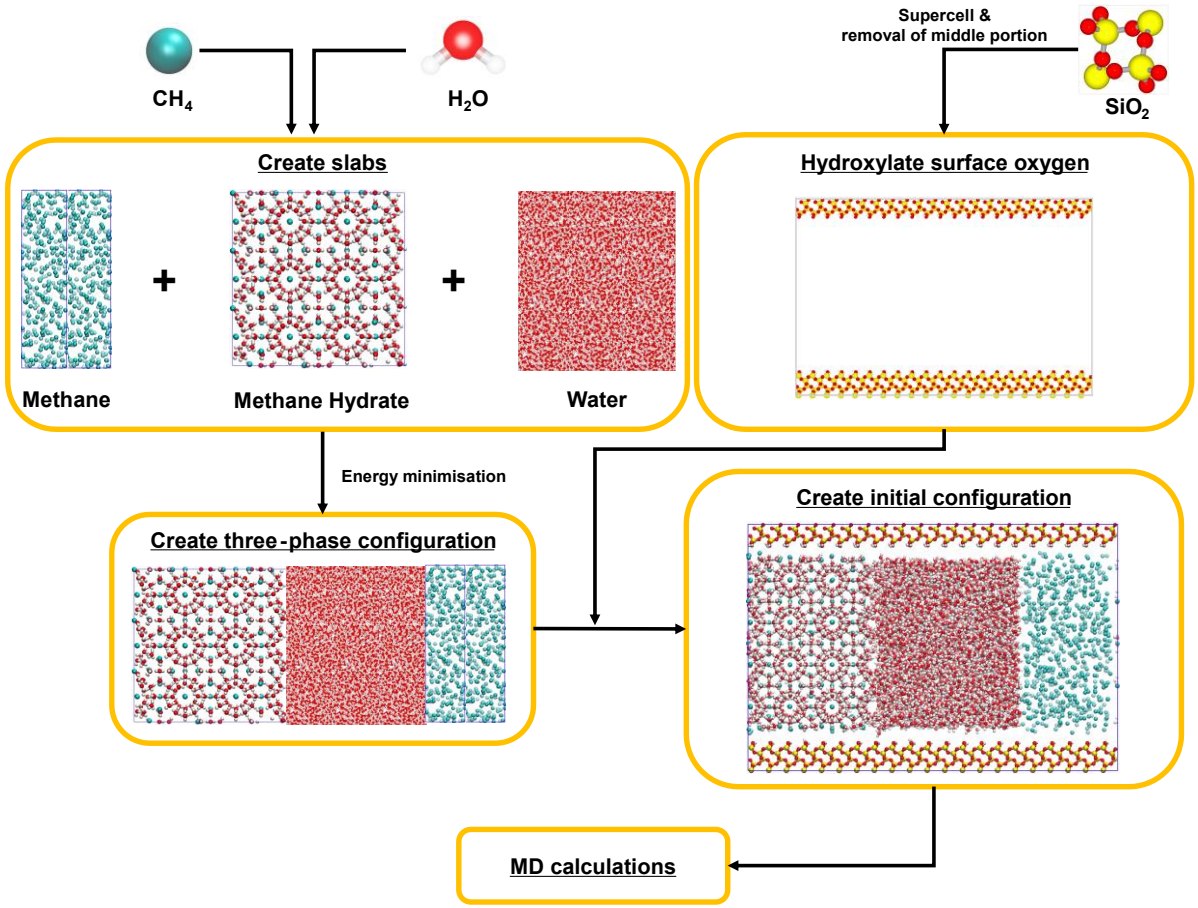

Figure A1: Main procedures of MD simulation for confined systems.

(A) 2 μs

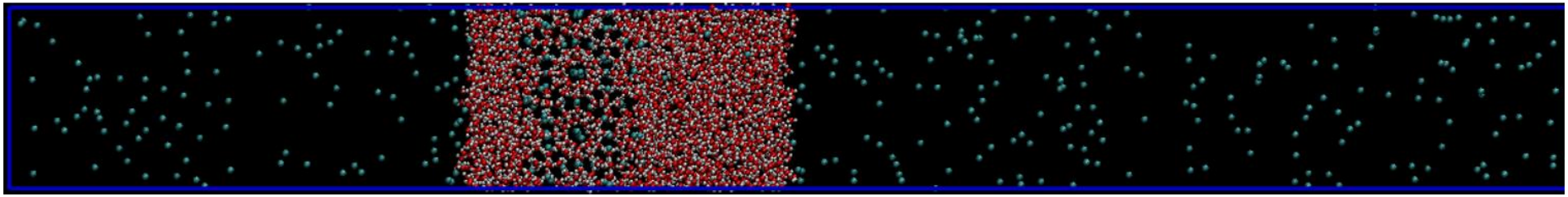

(B) 4 μs

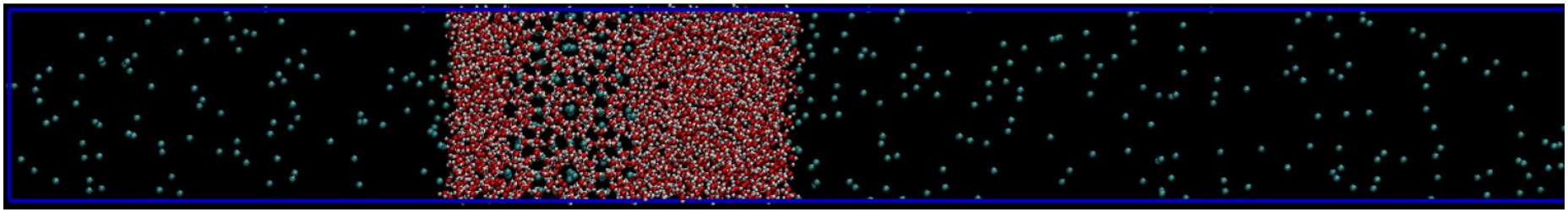

(C) 6 μs

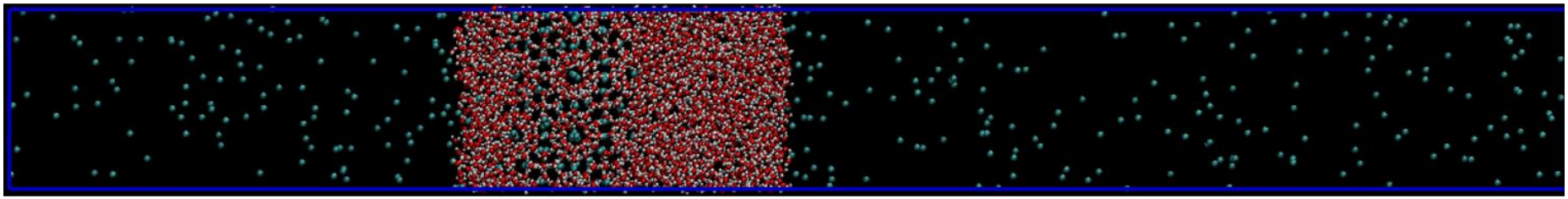

Figure A2: Snapshots from the bulk system simulation at 40 bar.

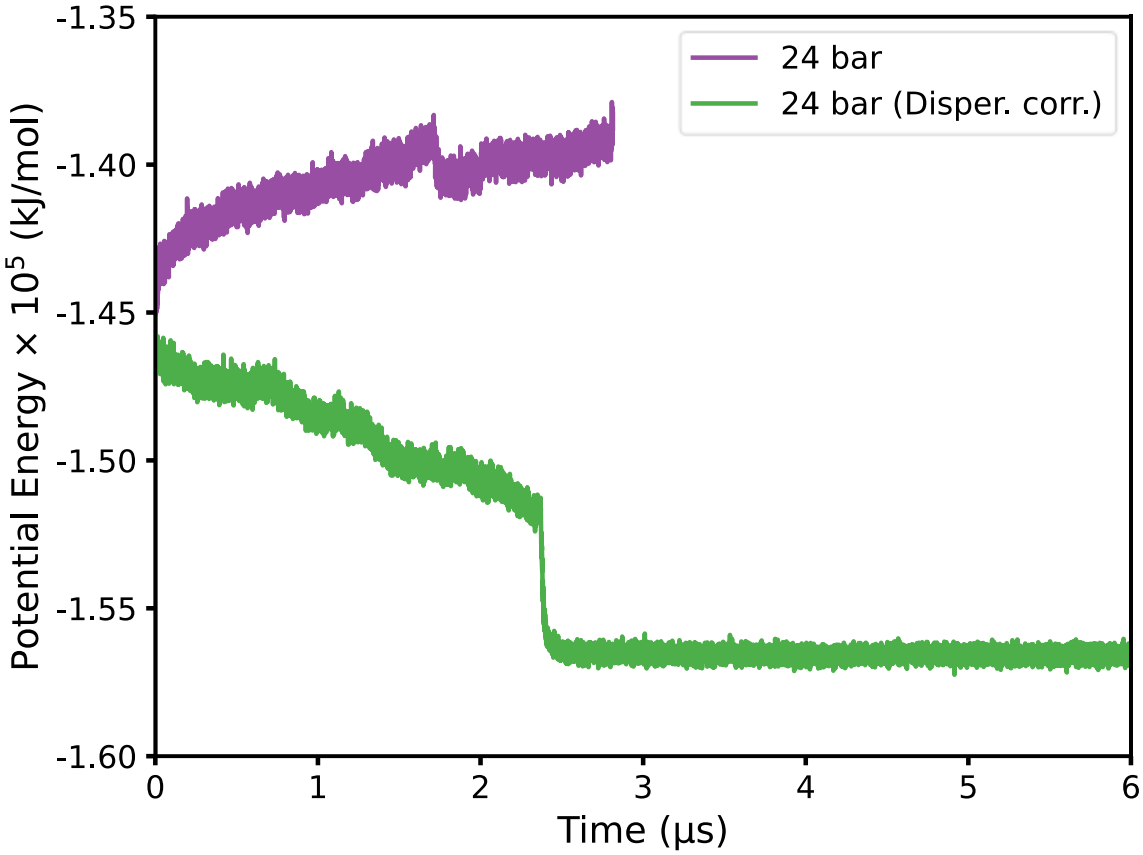

Figure A3: Variation of the potential energy of the bulk systems as a function of the *NPT*-MD simulation time with and without dispersion corrections at 24 bar and 271.65 K.

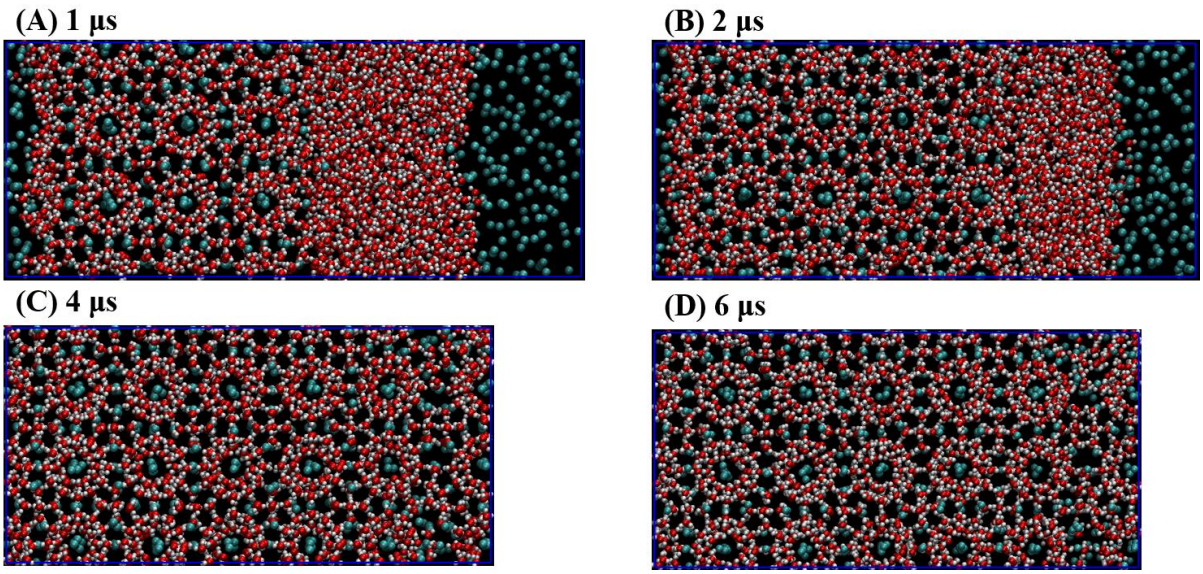

Figure A4: Snapshots from the bulk system simulation with dispersion corrections applied at 24 bar.

(A) 1 bar

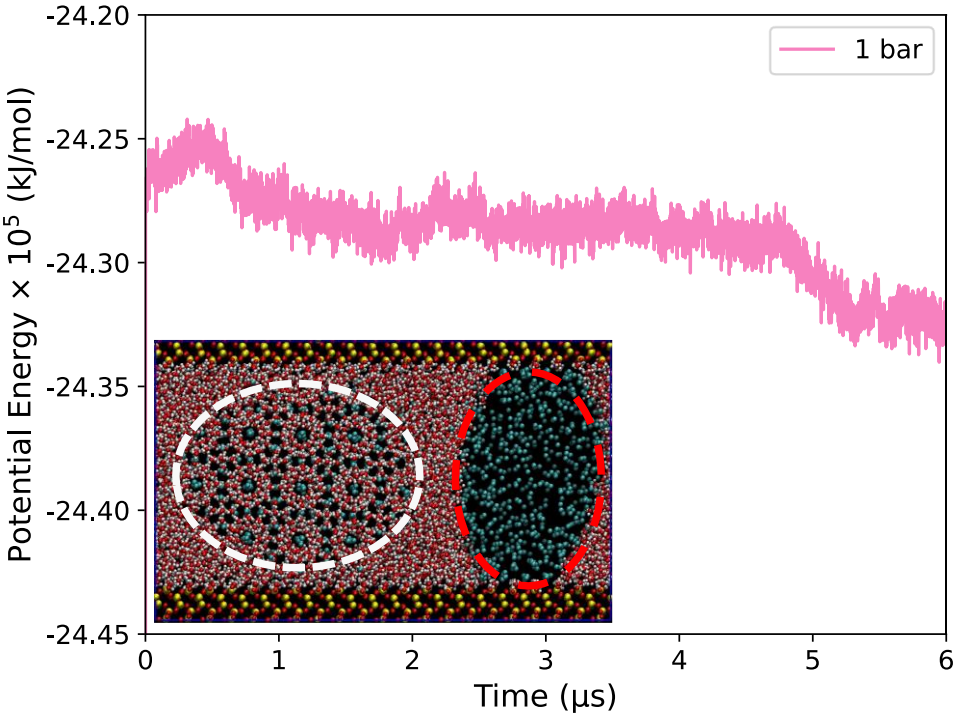

(B) 24 bar

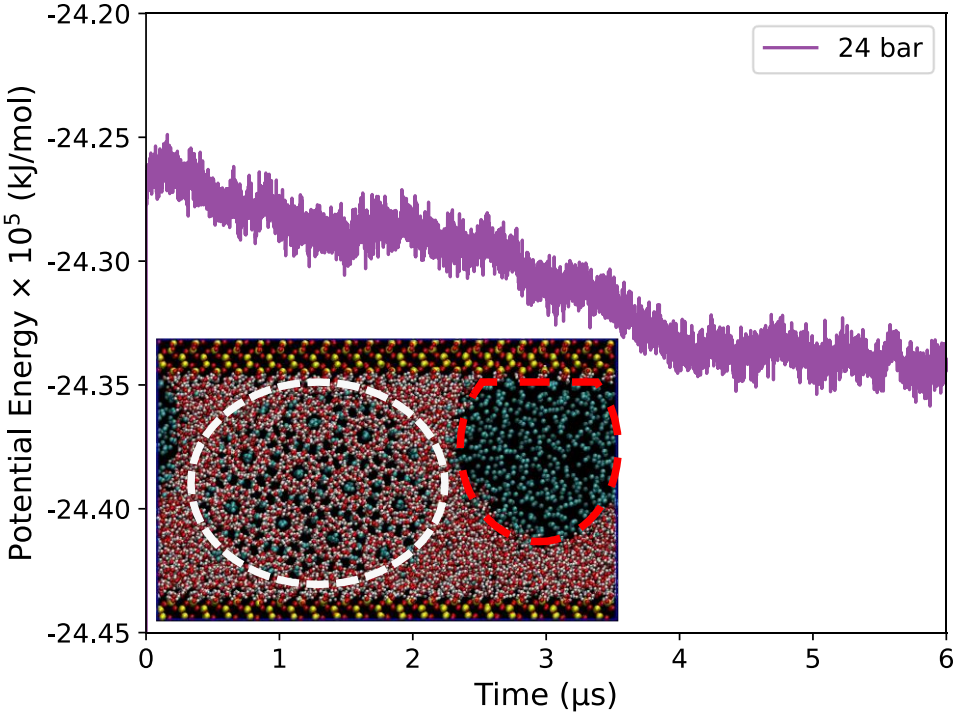

Figure A5: Final snapshots and the potential energy profiles of the confined systems at (A) 1 bar and (B) 24 bar.

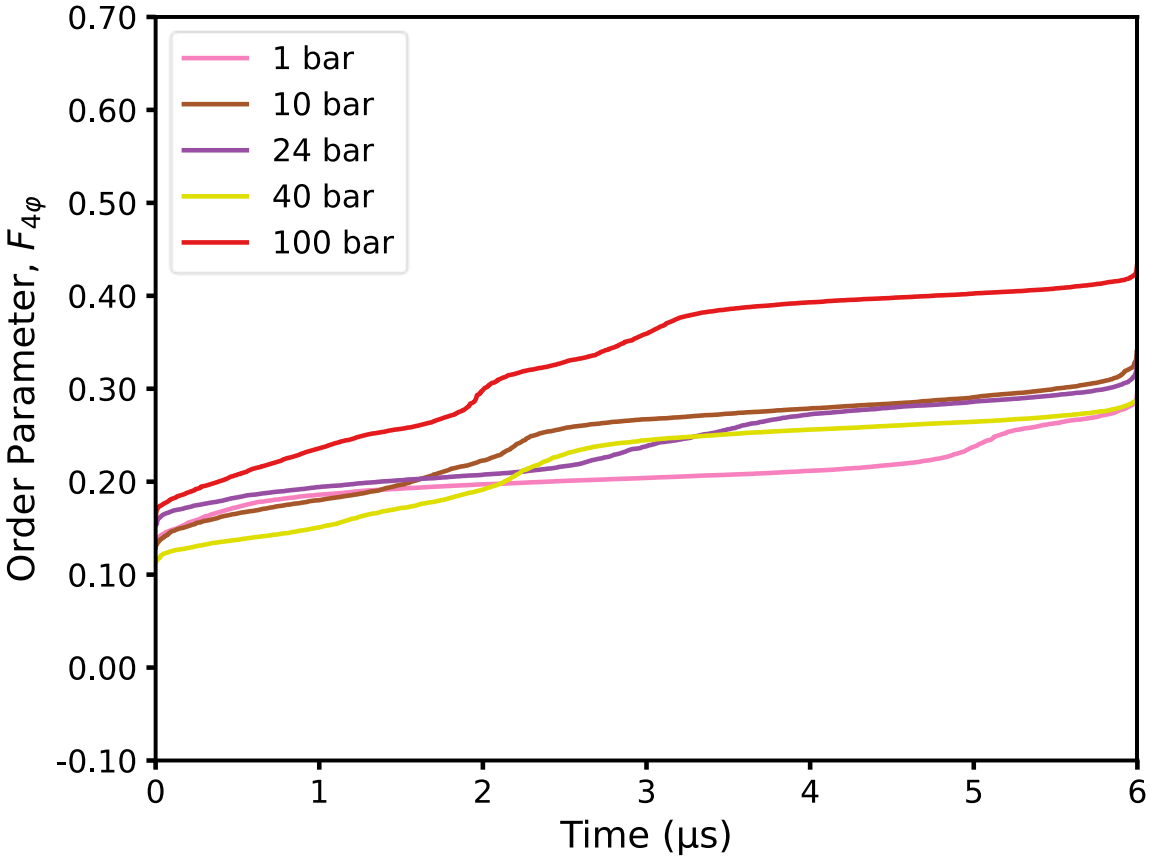

Figure A6: The evolution of $F_{4\varphi}$ order parameter of the confined systems over the course of the simulations.

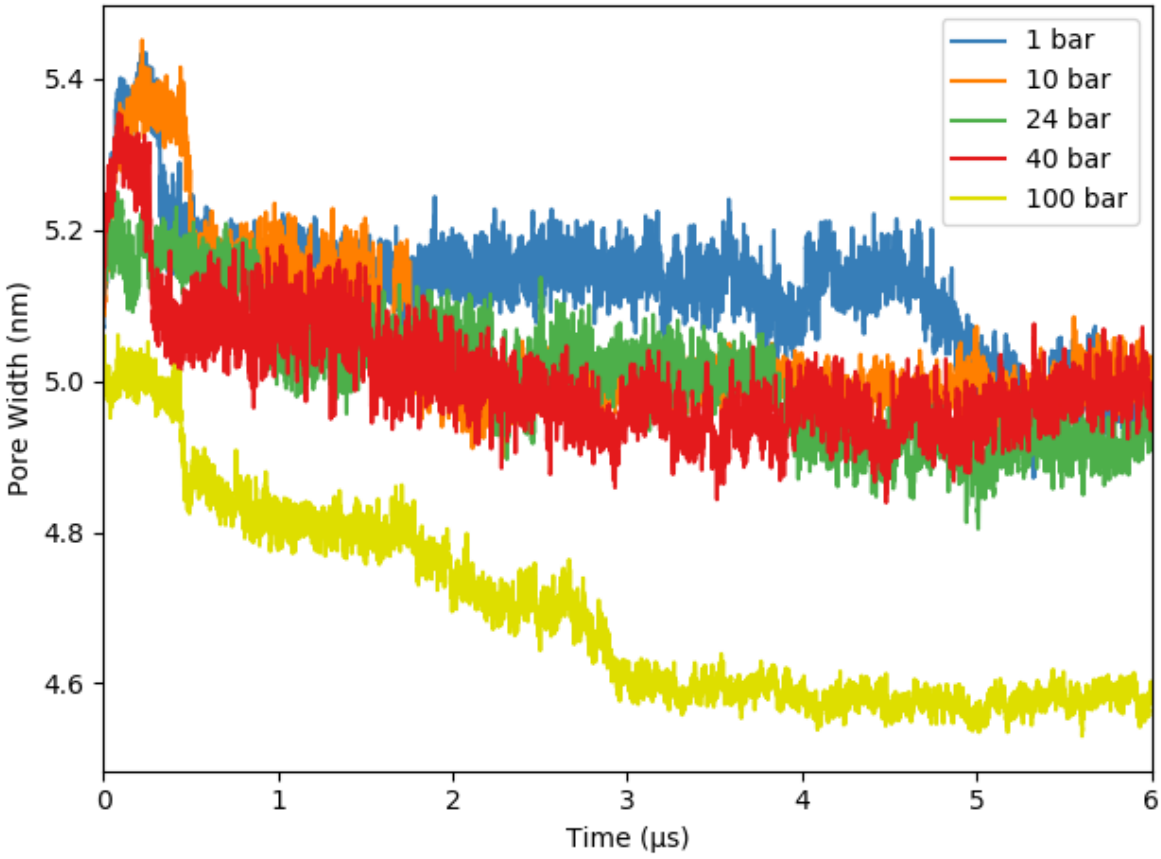

Figure A7: Variation of the pore width of the confined systems as a function of the *NPT*-MD simulation time at various pressures and 271.65 K.

Appendix B

Supporting Information for Chapter 4

(A) Type I-A ($C_{251}H_{385}O_{13}N_7S_3$)

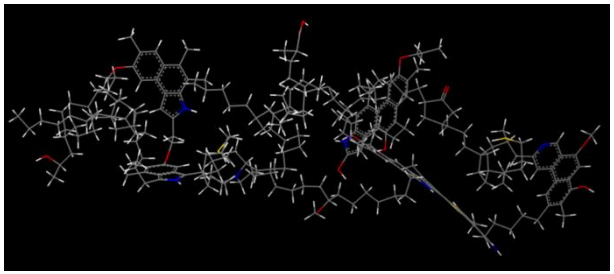

(B) Type II-A ($C_{252}H_{294}O_{24}N_6S_3$)

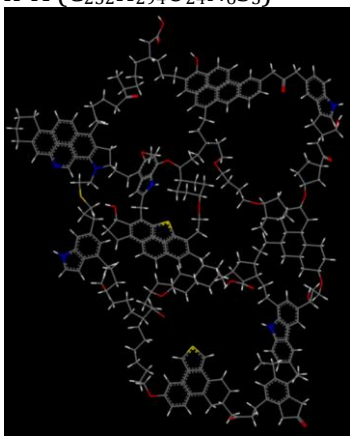

(C) Type II-B ($C_{234}H_{263}O_{14}N_5S_2$)

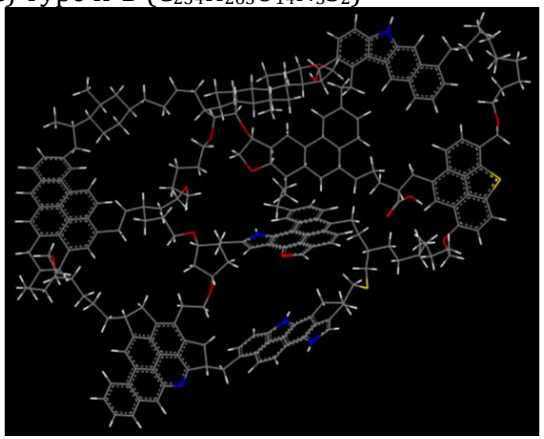

(D) Type II-C ($C_{242}H_{219}O_{13}N_5S_2$)

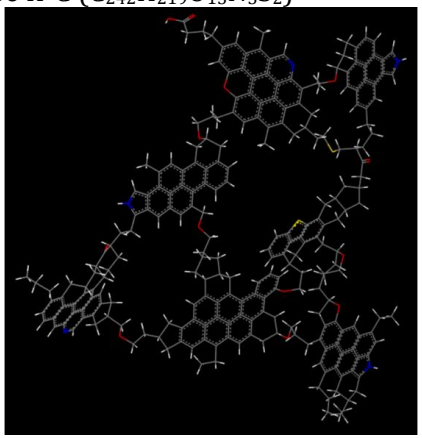

(E) Type II-D ($C_{175}H_{102}O_9N_4S_2$)

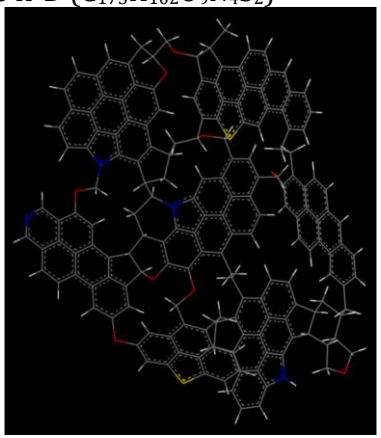

(F) Type III-A ($C_{233}H_{204}O_{27}N_4$)

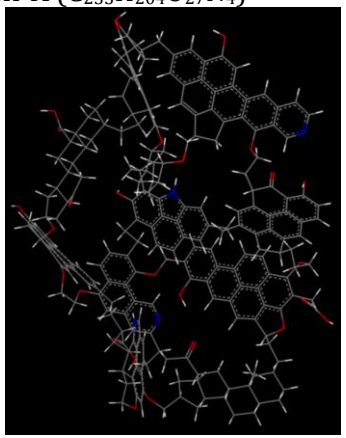

Figure B1: The kerogen model units of various types and maturity developed by Ungerer et al.[171] Kerogen types are illustrated on the van Krevelen Diagram (see Figure 4.1) with respect to their maturity levels. Red, blue, grey, white, and yellow lines refer to oxygen, nitrogen, carbon, hydrogen, and sulphur connected bonds, respectively.

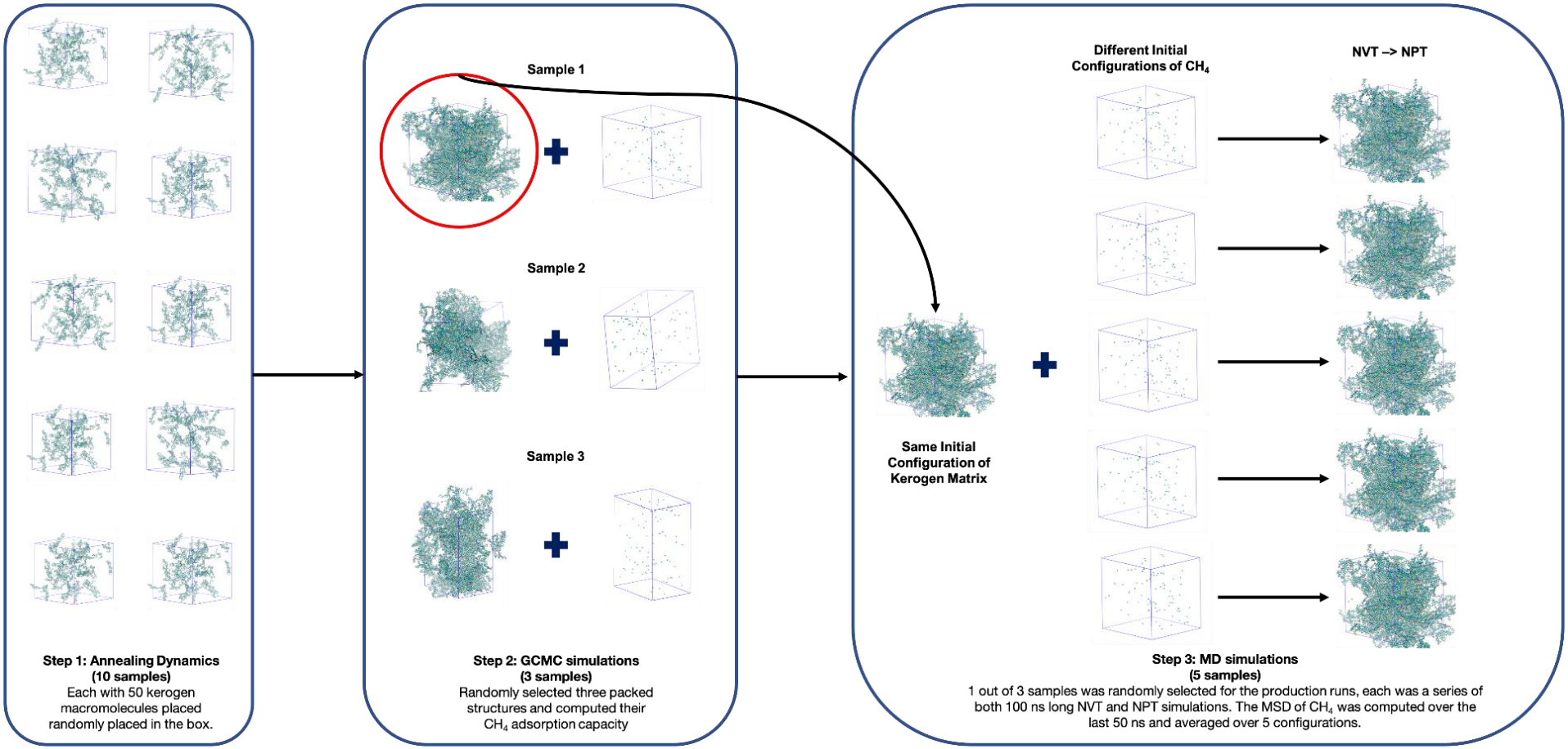

Figure B2: A workflow diagram of the simulation set up procedure.

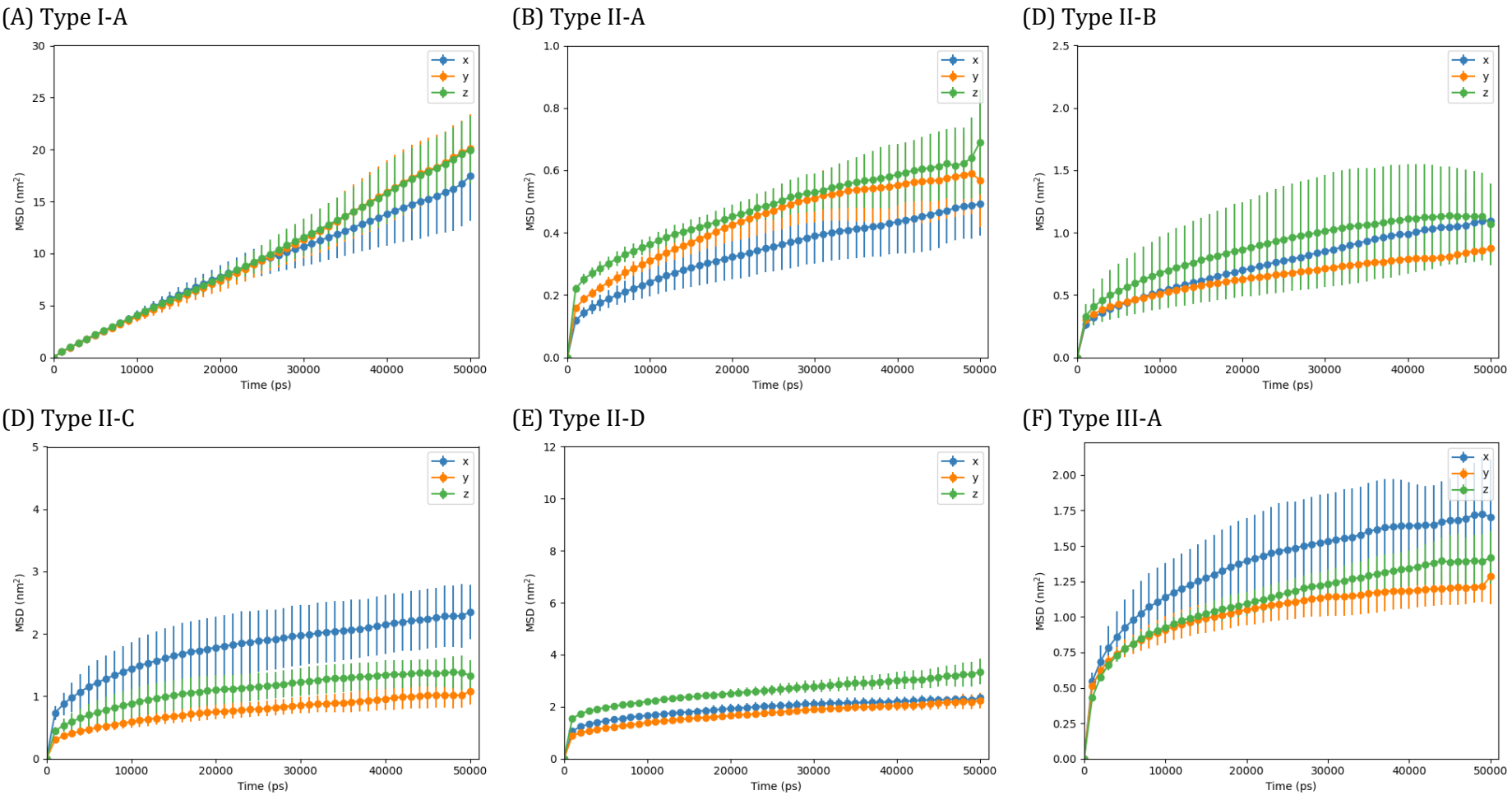

Figure B3: The average MSD of CH_4 in the x, y and z directions in six kerogen types in *NVT* ensemble at 365 K.

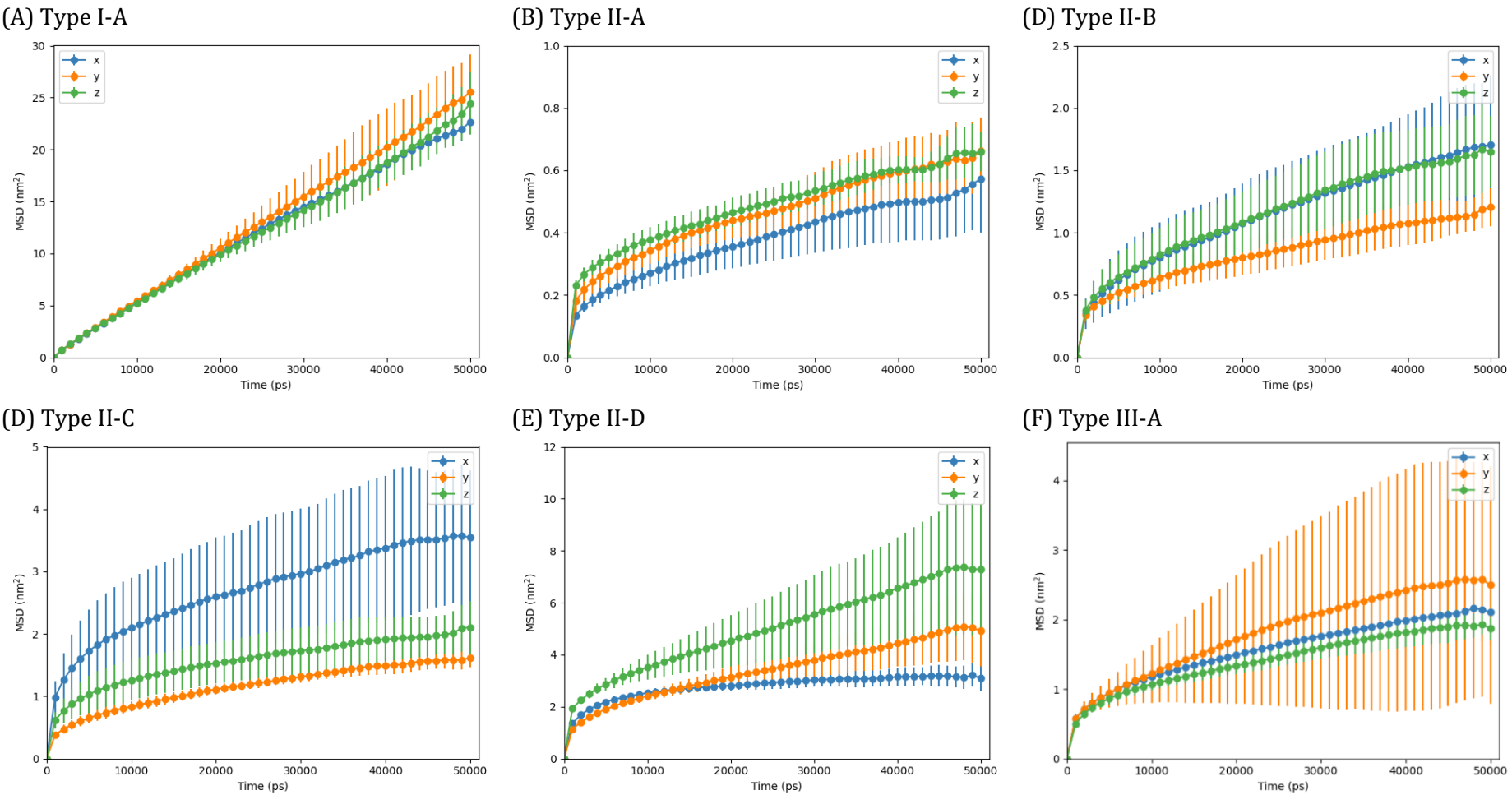

Figure B4: The average MSD of CH_4 in the x, y and z directions in six kerogen types in NPT ensemble at 365 K and 275 bar.

(A) Type I-A

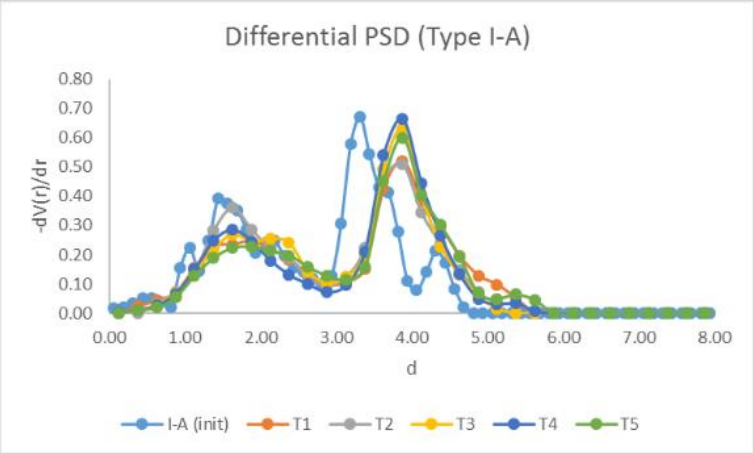

(B) Type II-A

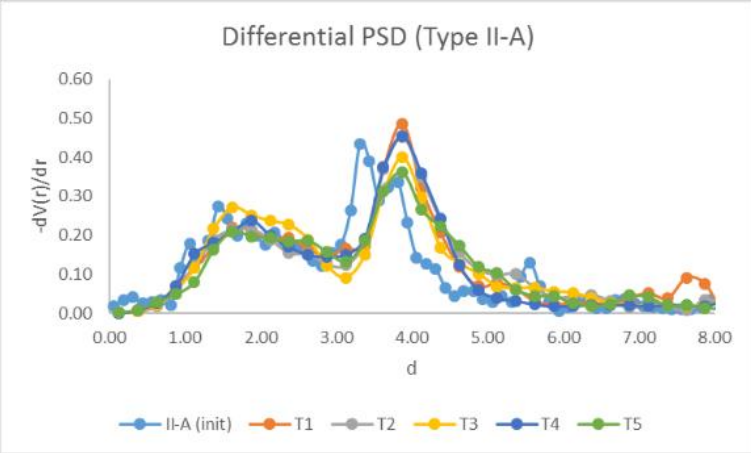

(C) Type II-B

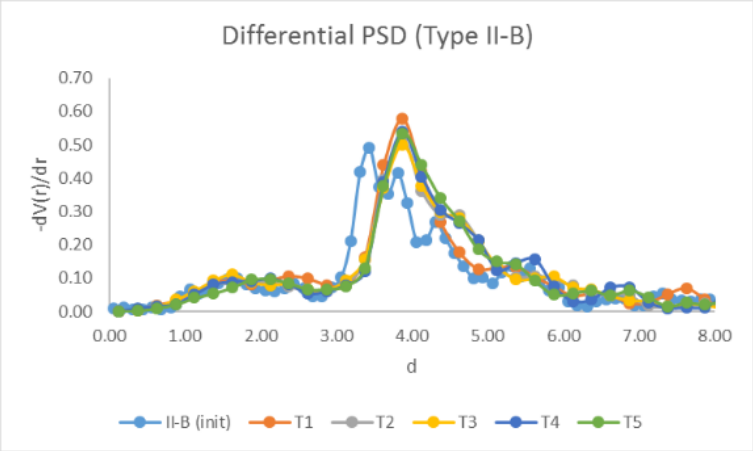

(D) Type II-C

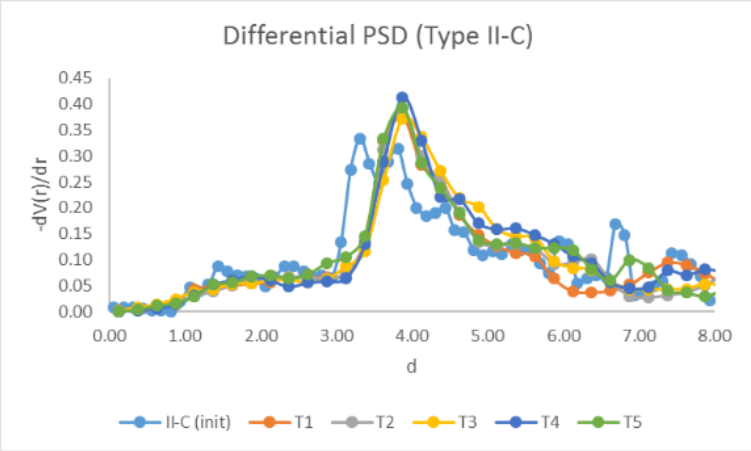

(figure continued on next page)

(E) Type II-D

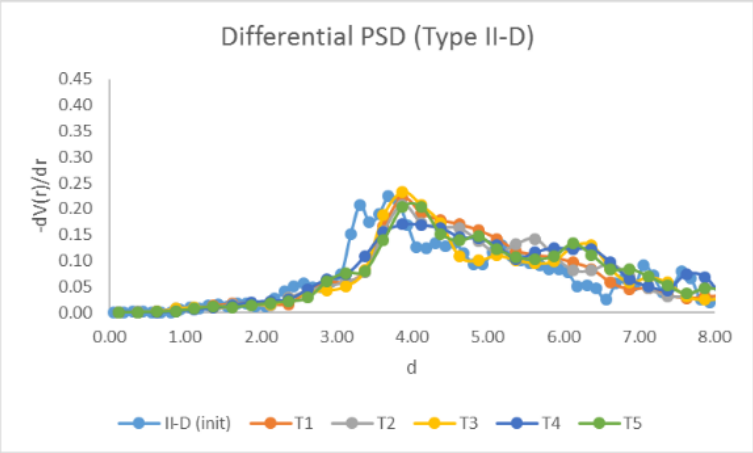

(F) Type III-A

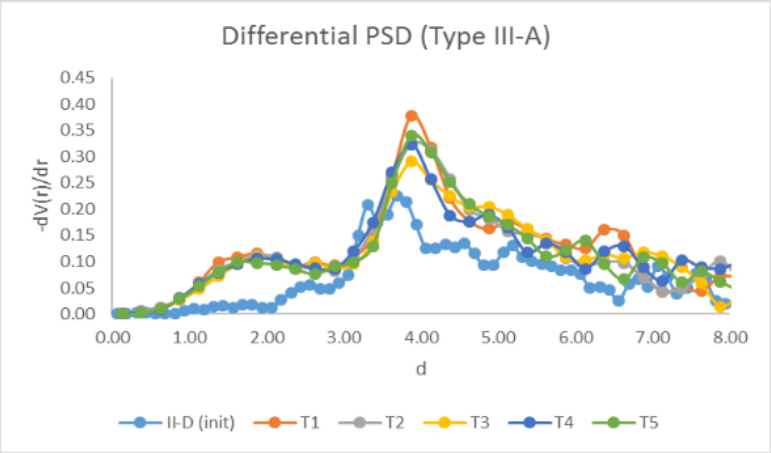

Figure B5: Pore size distributions of kerogens, before (initial) and after methane loading in five independent runs (T1, T2, T3, T4, and T5).

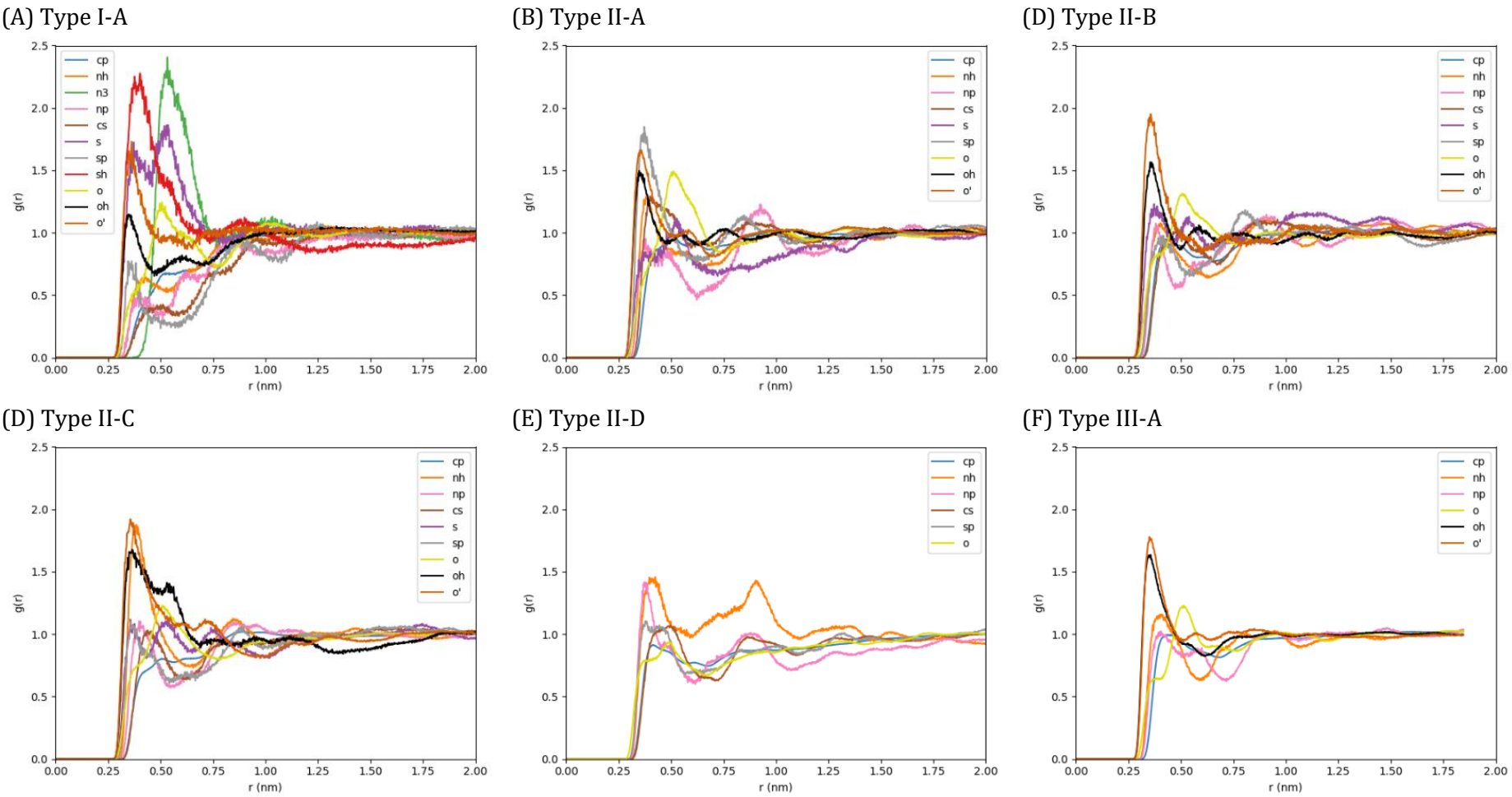

Figure B6: RDFs between CH_4 and atoms of different functional groups in kerogen macromolecules of various types at 365 K and 275 bar obtained from *NPT* MD simulations. Atom types defined by the CVFF force field and included in the above RDF plots are as follows: (cp) sp2 aromatic carbon, (cs) sp2 carbon involved in thiophene, (nh) sp2 nitrogen in 5-or 6- membered ring with hydrogen attached, (np) sp2 aromatic nitrogen (partial double bonds), (n3) sp3 nitrogen with three substituents, (o) sp3 oxygen in ether or ester groups, (oh) oxygen in hydroxyl (OH) group, (o') oxygen in carbonyl (C=O) group, (s) sulphur in methionine (C-S-C) group, (sh) sulphur in sulfhydryl (-SH) group, and (sp) sulphur in thiophene.

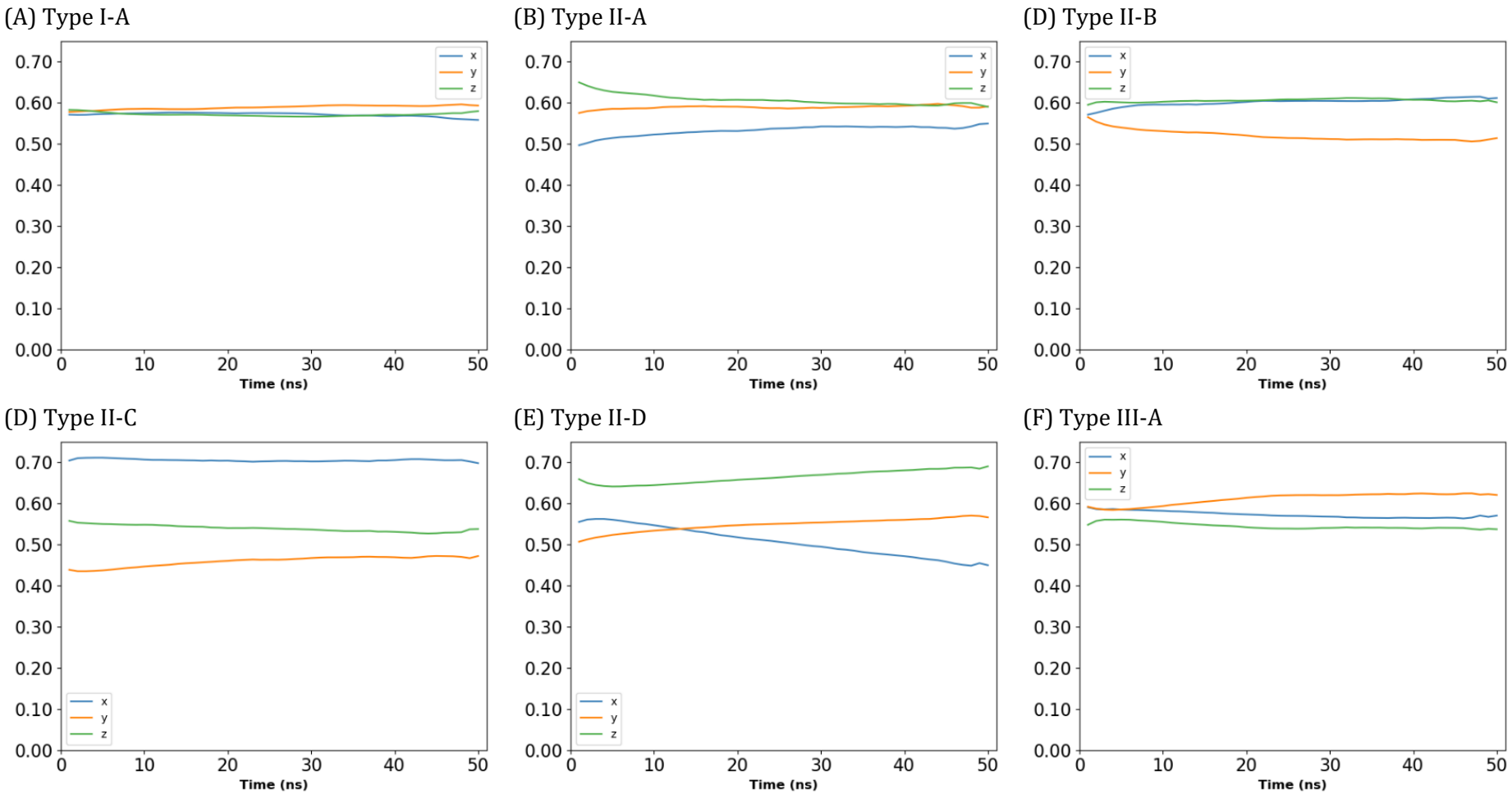

Figure B7: Normalized MSD over time using the formula $\sqrt{\langle i^2 \rangle} / \sqrt{\langle x^2 \rangle + \langle y^2 \rangle + \langle z^2 \rangle}$, where i is one of the three directions on the Cartesian space.

(A) NVT

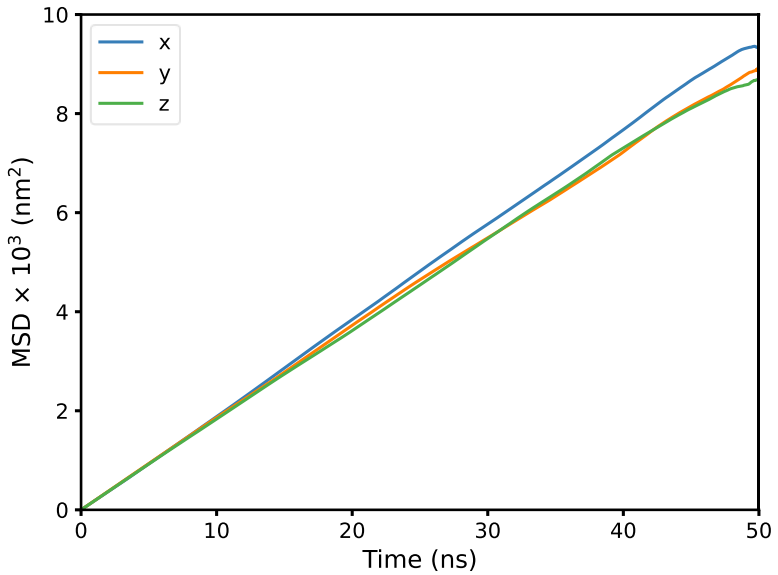

(B) NPT

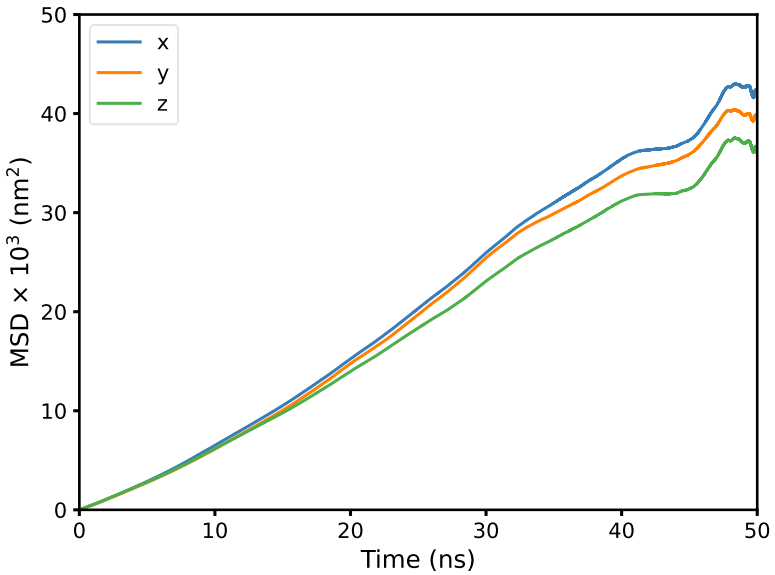

Figure B8: The MSD of bulk CH_4 in the x, y and z directions in *NVT* and *NPT* ensembles at 365 K and 275 bar.

Appendix C

Supporting Information for Chapter 5

Type I-A

CH_4

CO_2

(A) Run 1

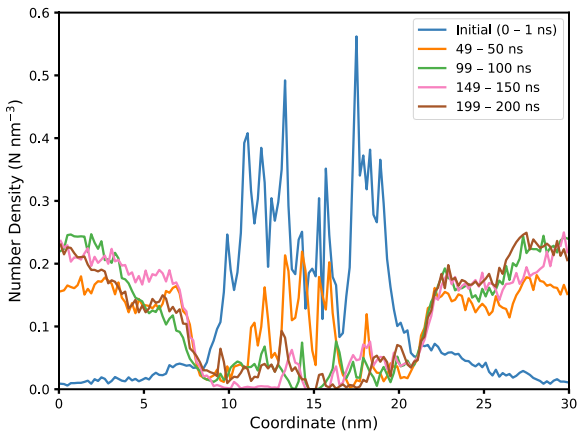

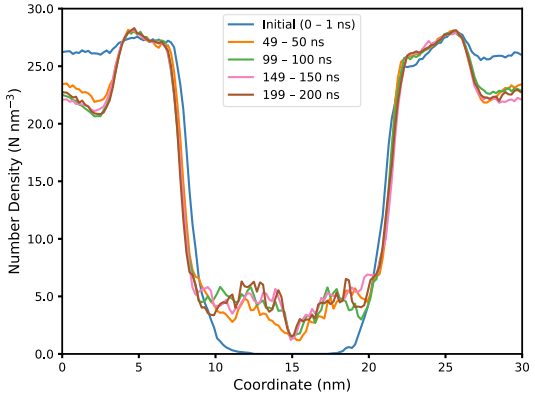

(B) Run 2

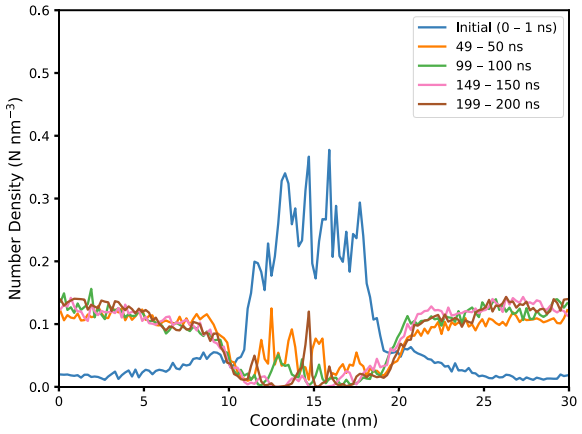

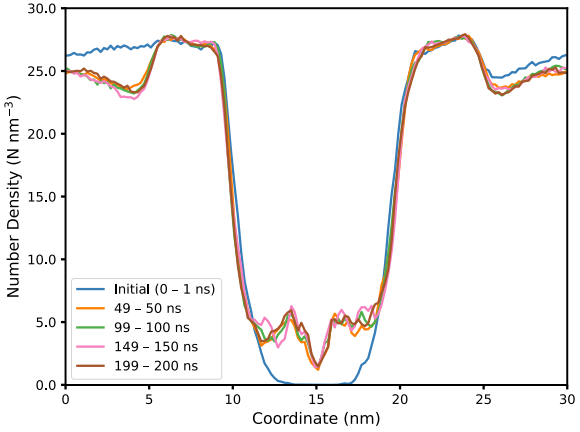

(figure continued on next page)

(C) Run 3

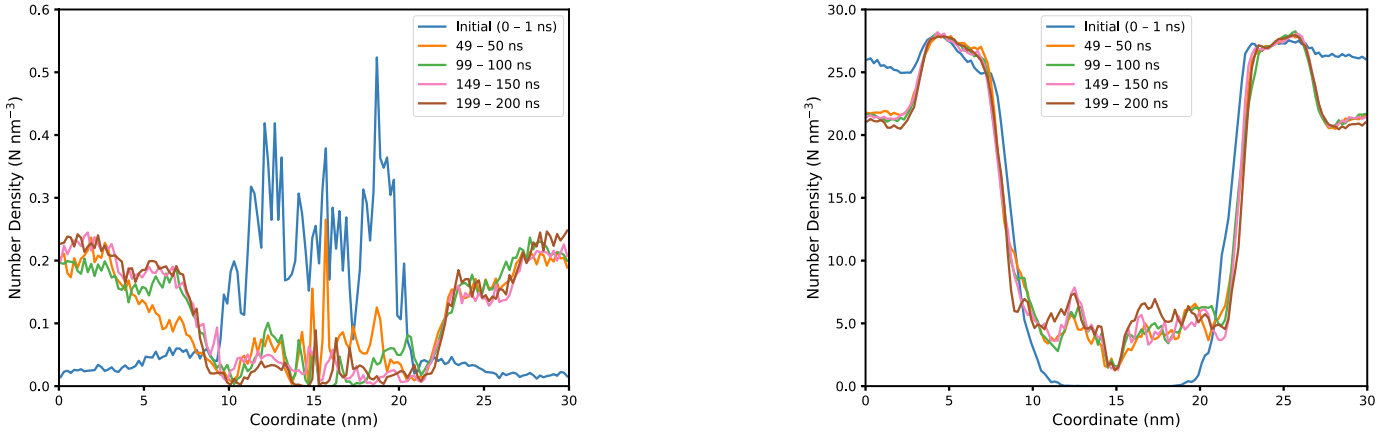

Figure C1: Density profiles (z-direction) of CH_4 and CO_2 in Type I-A kerogens at various time intervals. The kink located near the centre of simulation box is because the kerogen atoms at very centre of the slabs were not allowed to move in the z-direction to prevent the kerogen macromolecules from reorienting themselves.

Type II-D

CH_4

CO_2

(A) Run 1

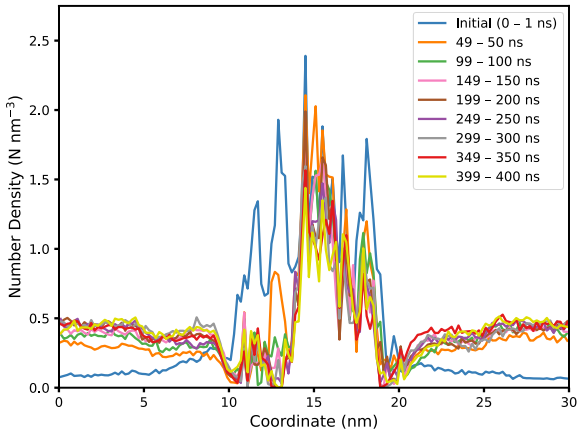

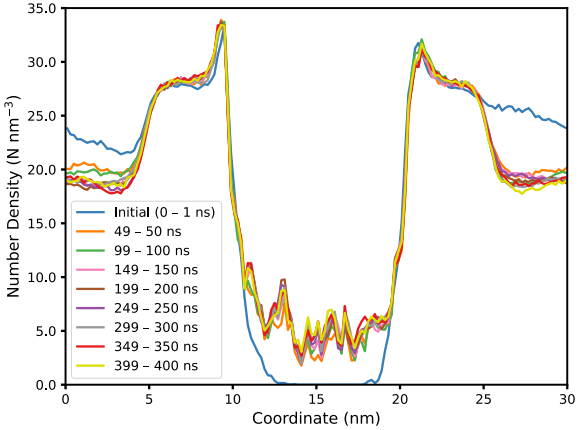

(B) Run 2

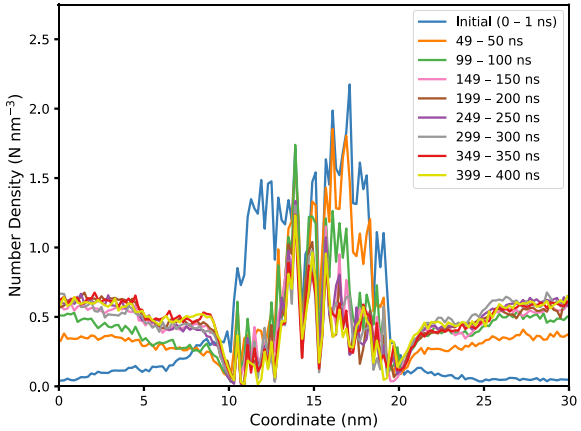

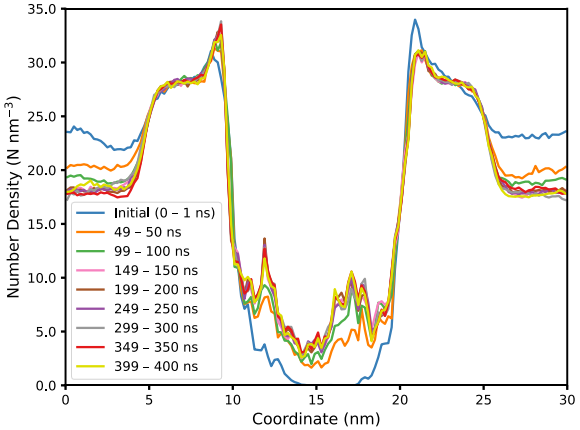

(figure continued on next page)

(C) Run 3

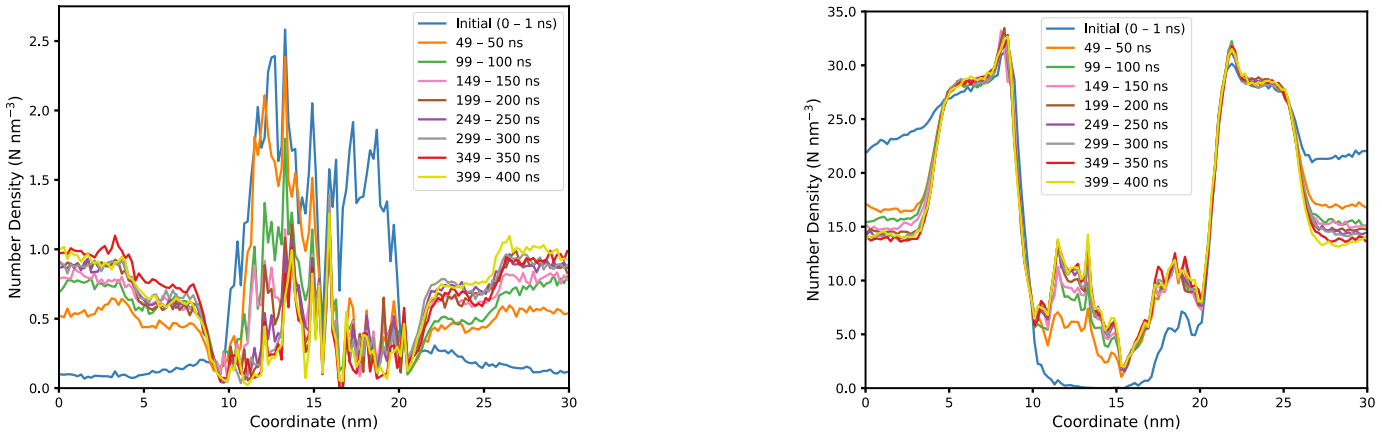

Figure C2: Density profiles (z-direction) of CH_4 and CO_2 in Type II-D kerogens at various time intervals. The kink located near the centre of simulation box is because the kerogen atoms at very centre of the slabs were not allowed to move in the z-direction to prevent the kerogen macromolecules from reorienting themselves. As a result, less CO_2 molecules were able to diffuse to the very centre of the slabs.

Type I-A

CH_4

CO_2

(A) Run 1

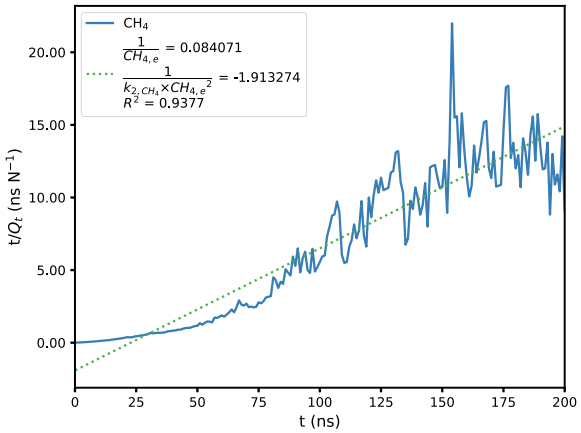

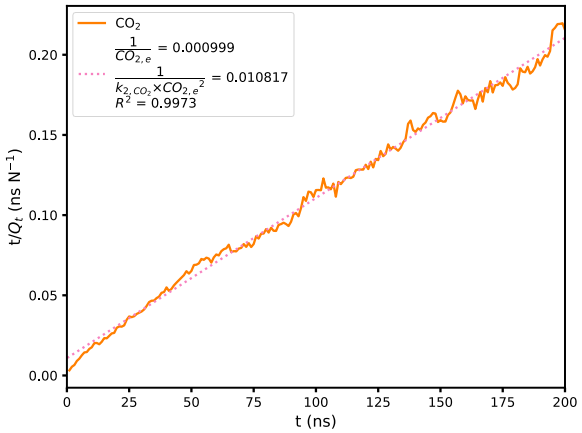

(B) Run 2

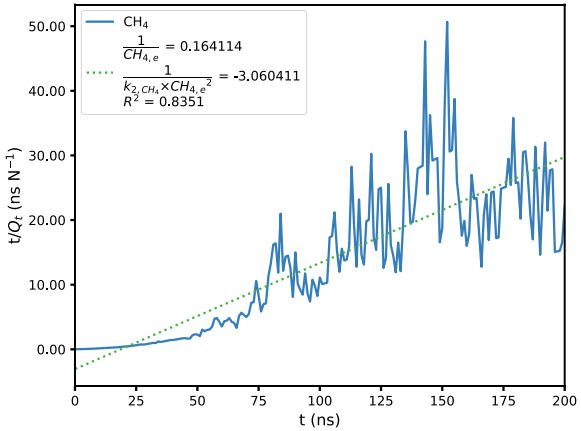

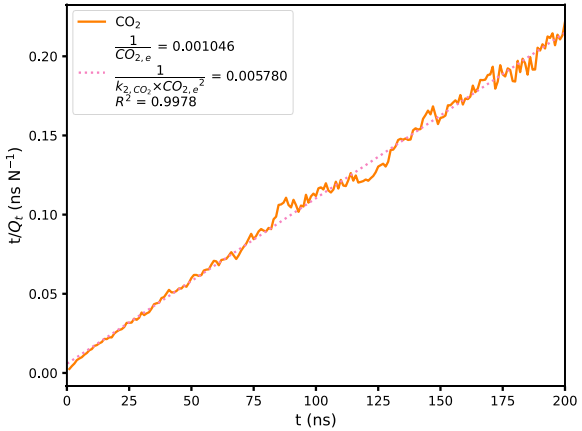

(figure continued on next page)

(C) Run 3

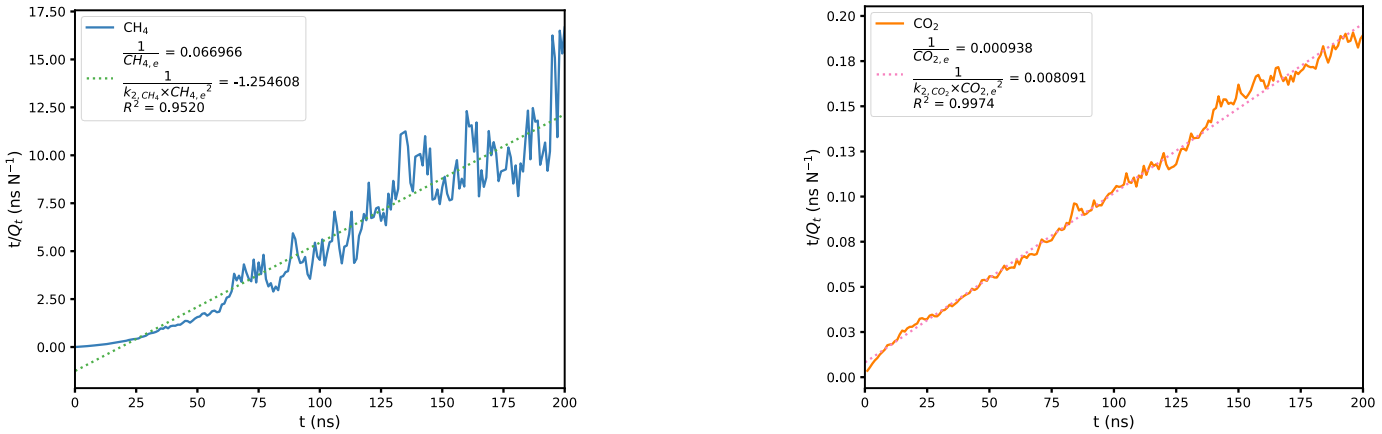

Figure C3: PSO sorption kinetics of CH_4 and CO_2 in Type I-A kerogens. Note the unit of the adsorbed amount, N, is number of molecules per kerogen slab, which contains 100 Type I-A kerogen macromolecules.

Type II-D

CH_4

CO_2

(A) Run 1

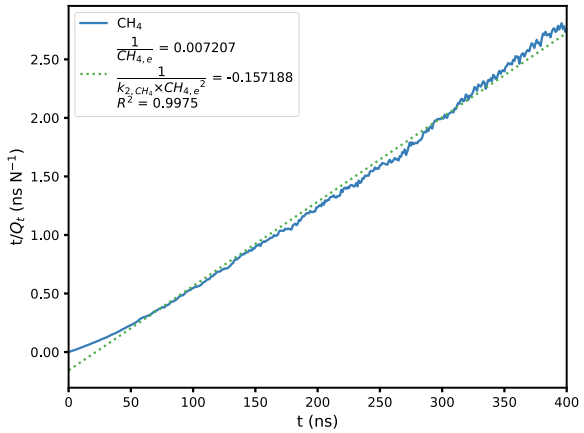

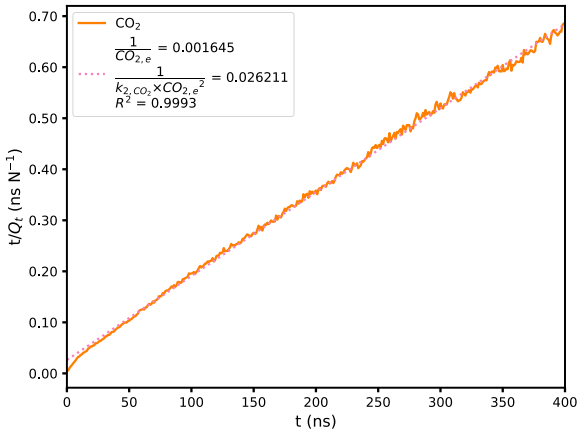

(B) Run 2

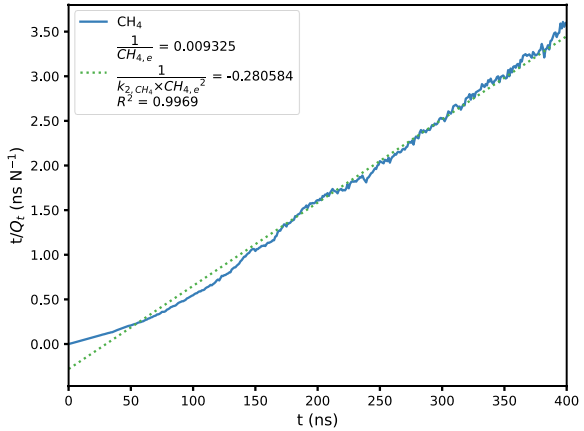

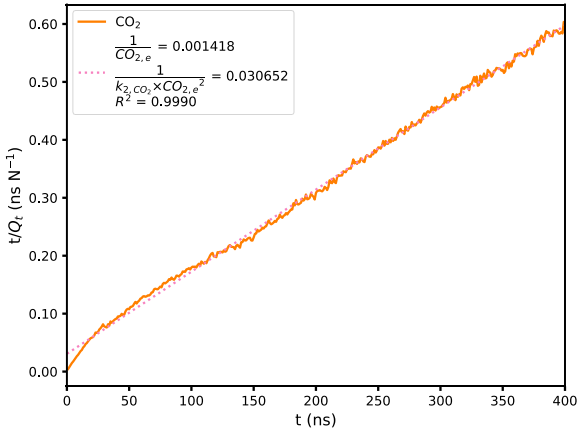

(figure continued on next page)

(C) Run 3

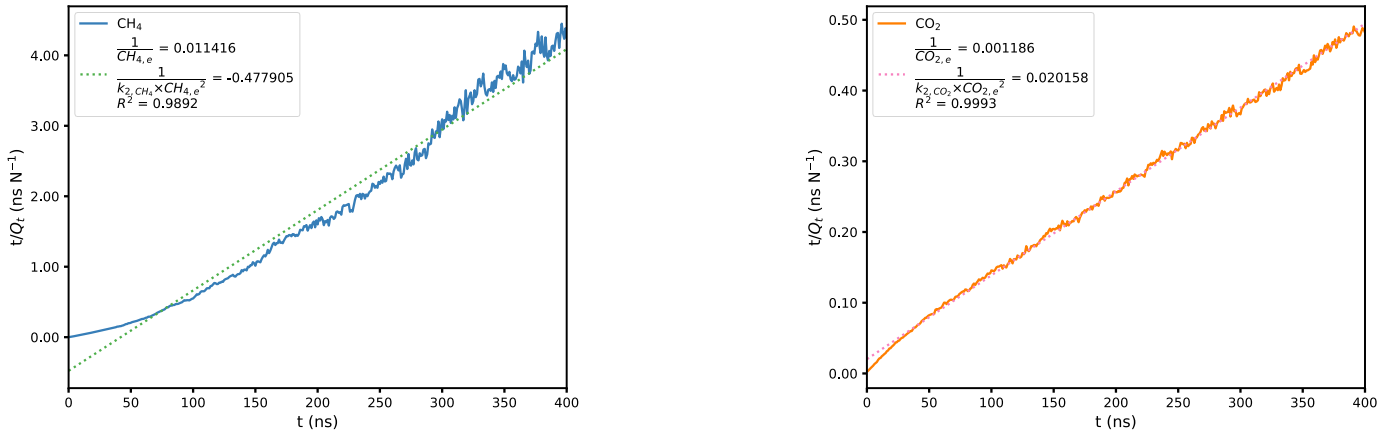

Figure C4: PSO sorption kinetics of CH_4 and CO_2 in Type II-D kerogens. Note the unit of the adsorbed amount, N, is number of molecules per kerogen slab, which contains 100 Type II-D kerogen macromolecules.

CO_2 **Type I-A** **Type II-D**

(A) Run 1

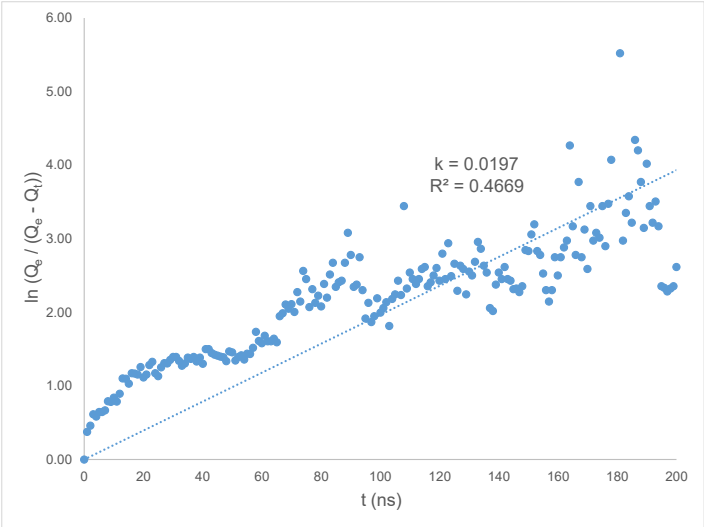

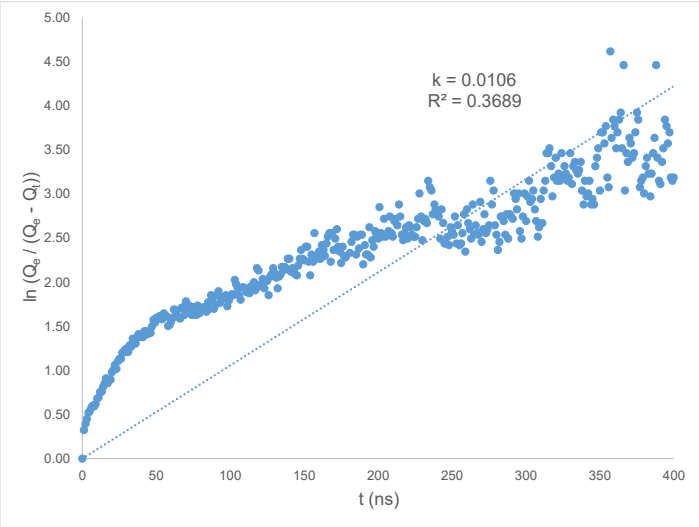

(B) Run 2

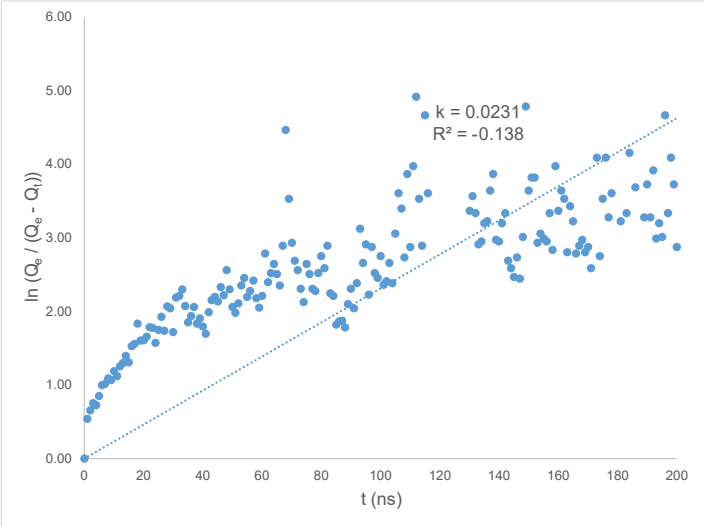

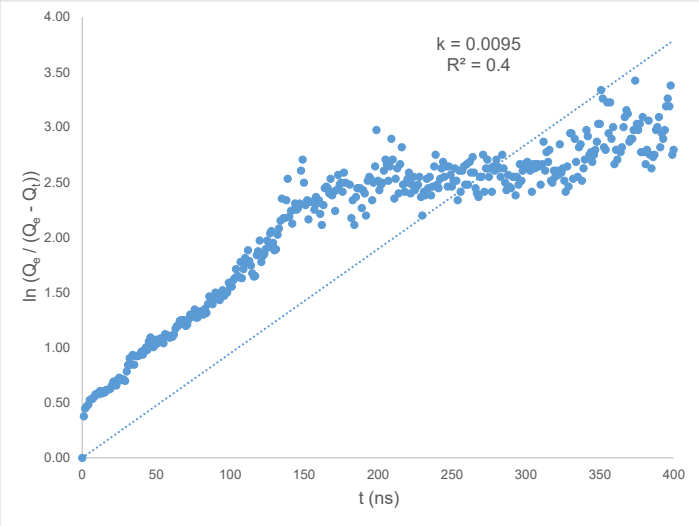

(figure continued on next page)

(C) Run 3

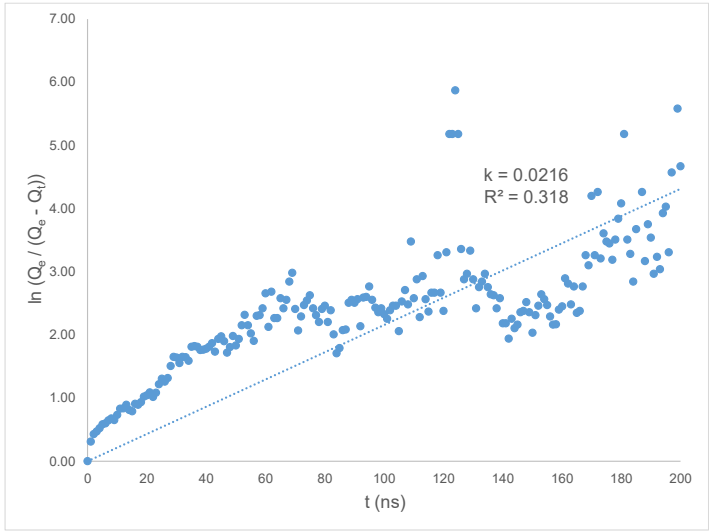

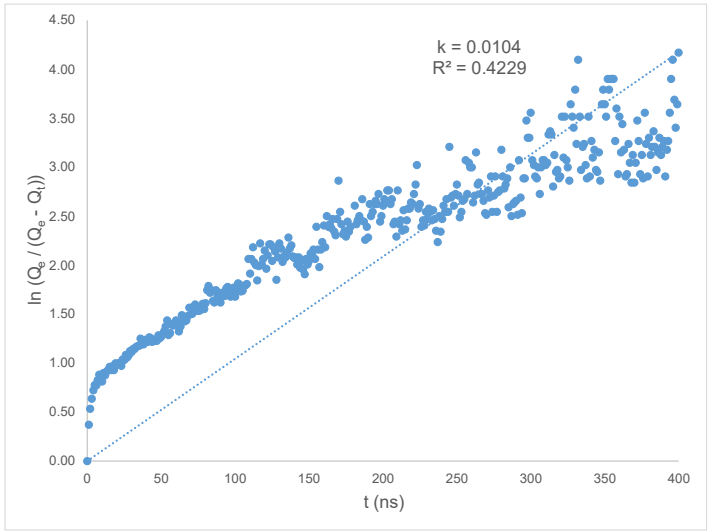

Figure C5: PFO adsorption kinetics of CO_2 in Type I-A and Type II-D kerogens.

References

(1) Sloan, E. D.; Koh, C. *Clathrate Hydrates of Natural Gases, Third Edition*; 2007; Vol. 20074156. https://doi.org/10.1201/9781420008494.

(2) Zhang, H. R.; Li, S.; Kelly, K. E.; Eddings, E. G. Underground in Situ Coal Thermal Treatment for Synthetic Fuels Production. *Prog Energy Combust Sci* **2017**, *62*, 1–32. https://doi.org/10.1016/j.pecs.2017.05.003.

(3) Mahzari, P.; Mitchell, T. M.; Jones, A. P.; Westacott, D.; Striolo, A. Direct Gas-in-Place Measurements Prove Much Higher Production Potential than Expected for Shale Formations. *Sci Rep* **2021**, *11* (1), 10775. https://doi.org/10.1038/s41598-021-90160-3.

(4) Konno, Y.; Fujii, T.; Sato, A.; Akamine, K.; Naiki, M.; Masuda, Y.; Yamamoto, K.; Nagao, J. Key Findings of the World's First Offshore Methane Hydrate Production Test off the Coast of Japan: Toward Future Commercial Production. *Energy and Fuels* **2017**, *31* (3), 2607–2616. https://doi.org/10.1021/acs.energyfuels.6b03143.

(5) Sloan, E. D. Fundamental Principles and Applications of Natural Gas Hydrates. *Nature* **2003**, *426* (6964), 353–359. https://doi.org/10.1038/nature02135.

(6) U.S. EIA. *Technically Recoverable Shale Oil and Shale Gas Resources : An Assessment of 137 Shale Formations in 41 Countries Outside the United States*; 2013; Vol. 2013.

(7) Cole, D.; Grszkiewicz, M. S.; Simonson, J.; Chialvo, A.; Melnichenko, Y.; Wignall, G.; Lynn, G.; Lin, J.; Habenschuss, A.; Gu, B.; Library, M.; Burchell, T.; Striolo, A.; Leng, Y.; Cummings, P.; Cooper, W.; Schilling, M.; Gubbins, K.; Frielinghaus, H. Influence of Nanoscale Porosity on Fluid Behavior; 2004; pp 740–753.

(8) Zang, J.; Konduri, S.; Nair, S.; Sholl, D. S. Self-Diffusion of Water and Simple Alcohols in Single-Walled Aluminosilicate Nanotubes. *ACS Nano* **2009**, *3* (6), 1548–1556. https://doi.org/10.1021/nn9001837.

(9) Pérez-Hernández, N.; Luong, T. Q.; Febles, M.; Marco, C.; Limbach, H. H.; Havenith, M.; Pérez, C.; Roux, M. V.; Pérez, R.; Martín, J. D. The Mobility of Water Molecules

through Hydrated Pores. *Journal of Physical Chemistry C* **2012**, *116* (17), 9616–9630. https://doi.org/10.1021/jp301323c.

(10) Koh, C. a. Towards a Fundamental Understanding of Natural Gas Hydrates. *Chem Soc Rev* **2002**, *31* (3), 157–167. https://doi.org/10.1039/b008672j.

(11) Iiyama, T.; Nishikawa, K.; Suzuki, T.; Kaneko, K. Study of the Structure of a Water Molecular Assembly in a Hydrophobic Nanospace at Low Temperature with in Situ X-Ray Diffraction. *Chem Phys Lett* **1997**, *274* (1–3), 152–158. https://doi.org/10.1016/S0009-2614(97)00664-7.

(12) Han, J.; Bogomolov, A. K.; Makarova, E. Y.; Yang, Z.; Lu, Y.; Li, X. Molecular Simulations on Adsorption and Diffusion of CO2 and CH4 in Moisture Coals. *Energy and Fuels* **2017**, *31* (12), 13528–13535. https://doi.org/10.1021/acs.energyfuels.7b02898.

(13) Borchardt, L.; Casco, M. E.; Silvestre-Albero, J. Methane Hydrate in Confined Spaces: An Alternative Storage System. *ChemPhysChem* **2018**, *19* (11), 1298–1314. https://doi.org/10.1002/cphc.201701250.

(14) Casco, M. E.; Silvestre-Albero, J.; Ramírez-Cuesta, A. J.; Rey, F.; Jordá, J. L.; Bansode, A.; Urakawa, A.; Peral, I.; Martínez-Escandell, M.; Kaneko, K.; Rodríguez-Reinoso, F. Methane Hydrate Formation in Confined Nanospace Can Surpass Nature. *Nat Commun* **2015**, *6*. https://doi.org/10.1038/ncomms7432.

(15) Casco, M. E.; Jordá, J. L.; Rey, F.; Fauth, F.; Martinez-Escandell, M.; Rodríguez-Reinoso, F.; Ramos-Fernández, E. V.; Silvestre-Albero, J. High-Performance of Gas Hydrates in Confined Nanospace for Reversible CH4/CO2Storage. *Chemistry - A European Journal* **2016**, *22* (29), 10028–10035. https://doi.org/10.1002/chem.201600958.

(16) Borchardt, L.; Nickel, W.; Casco, M.; Senkovska, I.; Bon, V.; Wallacher, D.; Grimm, N.; Krause, S.; Silvestre-Albero, J. Illuminating Solid Gas Storage in Confined Spaces – Methane Hydrate Formation in Porous Model Carbons. *Phys. Chem. Chem. Phys.* **2016**, *18* (30), 20607–20614. https://doi.org/10.1039/C6CP03993F.

(17) Cuadrado-Collados, C.; Fauth, F.; Such-Basañez, I.; Martínez-Escandell, M.; Silvestre-Albero, J. Methane Hydrate Formation in the Confined Nanospace of Activated Carbons in Seawater Environment. *Microporous and Mesoporous Materials* **2018**, *255*, 220–225. https://doi.org/10.1016/j.micromeso.2017.07.047.

(18) Horsfield, B.; Rullkötter, J. Diagenesis,Catagenesis, and Metagenesis of Organic Matter. *The Petroleum System—From Source to Trap*. American Association of Petroleum Geologists January 1, 1994, p 0. https://doi.org/10.1306/M60585C10.

(19) Kuuskraa, V. A.; Stevens, S. H.; Moodhe, K. Shale Gas Resources: An Assessment of 137 Shale Formations in 41 Countries Outside the United States. *Washington: Independent Statistics & Analysis and US Department of Energy* **2013**, No. June.

(20) Elliott, E. G.; Ettinger, A. S.; Leaderer, B. P.; Bracken, M. B.; Deziel, N. C. A Systematic Evaluation of Chemicals in Hydraulic-Fracturing Fluids and Wastewater for Reproductive and Developmental Toxicity. *J Expo Sci Environ Epidemiol* **2017**, *27* (1), 90–99. https://doi.org/10.1038/jes.2015.81.

(21) Yao, Y.; Chen, T.; Shen, S. S.; Niu, Y.; DesMarais, T. L.; Linn, R.; Saunders, E.; Fan, Z.; Lioy, P.; Kluz, T.; Chen, L. C.; Wu, Z.; Costa, M. Malignant Human Cell Transformation of Marcellus Shale Gas Drilling Flow Back Water. *Toxicol Appl Pharmacol* **2015**, *288* (1), 121–130. https://doi.org/10.1016/j.taap.2015.07.011.

(22) Etminan, S. R.; Javadpour, F.; Maini, B. B.; Chen, Z. Measurement of Gas Storage Processes in Shale and of the Molecular Diffusion Coefficient in Kerogen. *Int J Coal Geol* **2014**, *123*, 10–19. https://doi.org/10.1016/j.coal.2013.10.007.

(23) Clarkson, C. R.; Solano, N.; Bustin, R. M.; Bustin, A. M. M.; Chalmers, G. R. L.; He, L.; Melnichenko, Y. B.; Radliński, A. P.; Blach, T. P. Pore Structure Characterization of North American Shale Gas Reservoirs Using USANS/SANS, Gas Adsorption, and Mercury Intrusion. *Fuel* **2013**, *103*, 606–616. https://doi.org/10.1016/j.fuel.2012.06.119.

(24) Berthonneau, J.; Obliger, A.; Valdenaire, P. L.; Grauby, O.; Ferry, D.; Chaudanson, D.; Levitz, P.; Kim, J. J.; Ulm, F. J.; Pellenq, R. J. M. Mesoscale Structure, Mechanics,

and Transport Properties of Source Rocks' Organic Pore Networks. *Proc Natl Acad Sci U S A* **2018**, *115* (49), 12365–12370. https://doi.org/10.1073/pnas.1808402115.

(25) Krevelen, D. W. van. *Coal : Typology, Physics, Chemistry, Constitution*, 3rd ed.; Elsevier: Amsterdam , 1993.

(26) Huang, L.; Ning, Z.; Wang, Q.; Qi, R.; Zeng, Y.; Qin, H.; Ye, H.; Zhang, W. Molecular Simulation of Adsorption Behaviors of Methane, Carbon Dioxide and Their Mixtures on Kerogen: Effect of Kerogen Maturity and Moisture Content. *Fuel* **2018**, *211* (September 2017), 159–172. https://doi.org/10.1016/j.fuel.2017.09.060.

(27) Huang, L.; Ning, Z.; Wang, Q.; Ye, H.; Chen, Z.; Sun, Z.; Sun, F.; Qin, H. Enhanced Gas Recovery by CO2 Sequestration in Marine Shale: A Molecular View Based on Realistic Kerogen Model. *Arabian Journal of Geosciences* **2018**, *11* (15), 1–9. https://doi.org/10.1007/s12517-018-3762-5.

(28) Li, J.; Wang, Y.; Chen, Z.; Rahman, S. S. Simulation of Adsorption–Desorption Behavior in Coal Seam Gas Reservoirs at the Molecular Level: A Comprehensive Review. *Energy & Fuels* **2020**, *34* (3), 2619–2642. https://doi.org/10.1021/acs.energyfuels.9b02815.

(29) Sun, H.; Zhao, H.; Qi, N.; Li, Y. Molecular Insights into the Enhanced Shale Gas Recovery by Carbon Dioxide in Kerogen Slit Nanopores. *Journal of Physical Chemistry C* **2017**, *121* (18), 10233–10241. https://doi.org/10.1021/acs.jpcc.7b02618.

(30) Mosher, K.; He, J.; Liu, Y.; Rupp, E.; Wilcox, J. Molecular Simulation of Methane Adsorption in Micro- and Mesoporous Carbons with Applications to Coal and Gas Shale Systems. *Int J Coal Geol* **2013**, *109–110*, 36–44. https://doi.org/10.1016/j.coal.2013.01.001.

(31) Heller, R.; Zoback, M. Adsorption of Methane and Carbon Dioxide on Gas Shale and Pure Mineral Samples. *Journal of Unconventional Oil and Gas Resources* **2014**, *8* (C), 14–24. https://doi.org/10.1016/j.juogr.2014.06.001.

(32) Huang, L.; Ning, Z.; Wang, Q.; Zhang, W.; Cheng, Z.; Wu, X.; Qin, H. Effect of Organic Type and Moisture on CO2/CH4 Competitive Adsorption in Kerogen with

Implications for CO2 Sequestration and Enhanced CH4 Recovery. *Appl Energy* **2018**, *210*, 28–43. https://doi.org/10.1016/j.apenergy.2017.10.122.

(33) Charoensuppanimit, P.; Mohammad, S. A.; Gasem, K. A. M. Measurements and Modeling of Gas Adsorption on Shales. *Energy and Fuels* **2016**, *30* (3), 2309–2319. https://doi.org/10.1021/acs.energyfuels.5b02751.

(34) Zhao, H.; Wu, T.; Firoozabadi, A. High Pressure Sorption of Various Hydrocarbons and Carbon Dioxide in Kimmeridge Blackstone and Isolated Kerogen. *Fuel* **2018**, *224*, 412–423. https://doi.org/10.1016/j.fuel.2018.02.186.

(35) Sanguinito, S.; Goodman, A.; Tkach, M.; Kutchko, B.; Culp, J.; Natesakhawat, S.; Fazio, J.; Fukai, I.; Crandall, D. Quantifying Dry Supercritical CO2-Induced Changes of the Utica Shale. *Fuel* **2018**, *226*, 54–64. https://doi.org/10.1016/j.fuel.2018.03.156.

(36) Wu, T.; Zhao, H.; Tesson, S.; Firoozabadi, A. Absolute Adsorption of Light Hydrocarbons and Carbon Dioxide in Shale Rock and Isolated Kerogen. *Fuel* **2019**, *235*, 855–867. https://doi.org/10.1016/j.fuel.2018.08.023.

(37) Zhao, H.; Lai, Z.; Firoozabadi, A. Sorption Hysteresis of Light Hydrocarbons and Carbon Dioxide in Shale and Kerogen. *Sci Rep* **2017**, *7* (1), 16209. https://doi.org/10.1038/s41598-017-13123-7.

(38) Gonciaruk, A.; Hall, M. R.; Fay, M. W.; Parmenter, C. D. J.; Vane, C. H.; Khlobystov, A. N.; Ripepi, N. Kerogen Nanoscale Structure and CO2 Adsorption in Shale Micropores. *Sci Rep* **2021**, *11* (1), 1–13. https://doi.org/10.1038/s41598-021-83179-z.

(39) Wang, S.; Yao, X.; Feng, Q.; Javadpour, F.; Yang, Y.; Xue, Q.; Li, X. Molecular Insights into Carbon Dioxide Enhanced Multi-Component Shale Gas Recovery and Its Sequestration in Realistic Kerogen. *Chemical Engineering Journal* **2021**, *425* (May), 130292. https://doi.org/10.1016/j.cej.2021.130292.

(40) Khosrokhavar, R.; Wolf, K. H.; Bruining, H. Sorption of CH4 and CO2 on a Carboniferous Shale from Belgium Using a Manometric Setup. *Int J Coal Geol* **2014**, *128–129*, 153–161. https://doi.org/10.1016/j.coal.2014.04.014.

(41) Hamza, A.; Hussein, I. A.; Al-Marri, M. J.; Mahmoud, M.; Shawabkeh, R.; Aparicio, S. CO2 Enhanced Gas Recovery and Sequestration in Depleted Gas Reservoirs: A

Review. *J Pet Sci Eng* **2021**, *196*, 107685. https://doi.org/10.1016/j.petrol.2020.107685.

(42) Bui, M.; Adjiman, C. S.; Bardow, A.; Anthony, E. J.; Boston, A.; Brown, S.; Fennell, P. S.; Fuss, S.; Galindo, A.; Hackett, L. A.; Hallett, J. P.; Herzog, H. J.; Jackson, G.; Kemper, J.; Krevor, S.; Maitland, G. C.; Matuszewski, M.; Metcalfe, I. S.; Petit, C.; Puxty, G.; Reimer, J.; Reiner, D. M.; Rubin, E. S.; Scott, S. A.; Shah, N.; Smit, B.; Trusler, J. P. M.; Webley, P.; Wilcox, J.; Mac Dowell, N. Carbon Capture and Storage (CCS): The Way Forward. *Energy Environ Sci* **2018**, *11* (5), 1062–1176. https://doi.org/10.1039/c7ee02342a.

(43) Liu, J.; Xie, L.; Yao, Y.; Gan, Q.; Zhao, P.; Du, L. Preliminary Study of Influence Factors and Estimation Model of the Enhanced Gas Recovery Stimulated by Carbon Dioxide Utilization in Shale. *ACS Sustain Chem Eng* **2019**, *7* (24), 20114–20125. https://doi.org/10.1021/acssuschemeng.9b06005.

(44) Middleton, R. S.; Carey, J. W.; Currier, R. P.; Hyman, J. D.; Kang, Q.; Karra, S.; Jiménez-Martínez, J.; Porter, M. L.; Viswanathan, H. S. Shale Gas and Non-Aqueous Fracturing Fluids: Opportunities and Challenges for Supercritical CO2. *Appl Energy* **2015**, *147*, 500–509. https://doi.org/10.1016/j.apenergy.2015.03.023.

(45) Dong, M.; Gong, H.; Sang, Q.; Zhao, X.; Zhu, C. Review of CO2-Kerogen Interaction and Its Effects on Enhanced Oil Recovery and Carbon Sequestration in Shale Oil Reservoirs. *Resources Chemicals and Materials* **2022**. https://doi.org/10.1016/j.recm.2022.01.006.

(46) Verlet, L. Computer "Experiments" on Classical Fluids. I. Thermodynamical Properties of Lennard-Jones Molecules. *Physical Review* **1967**, *159* (1), 98–103. https://doi.org/10.1103/PhysRev.159.98.

(47) Hockney, R. W.; Eastwood, J. W. *Computer Simulation Using Particles*; Adam Hilger: Bristol, 1988. https://doi.org/10.1887/0852743920.

(48) Swope, W. C.; Andersen, H. C.; Berens, P. H.; Wilson, K. R. A Computer Simulation Method for the Calculation of Equilibrium Constants for the Formation of Physical

Clusters of Molecules: Application to Small Water Clusters. *J Chem Phys* **1982**, *76* (1), 637–649. https://doi.org/10.1063/1.442716.

(49) Gear, C. W. *THE NUMERICAL INTEGRATION OF ORDINARY DIFFERENTIAL EQUATIONS OF VARIOUS ORDERS*; Argonne, IL (United States), 1966. https://doi.org/10.2172/4534813.

(50) Van Gunsteren, W. F.; Berendsen, H. J. C. Algorithms for Macromolecular Dynamics and Constraint Dynamics. *Mol Phys* **1977**, *34* (5), 1311–1327. https://doi.org/10.1080/00268977700102571.

(51) Hess, B.; Bekker, H.; Berendsen, H. J. C.; Fraaije, J. G. E. M. LINCS: A Linear Constraint Solver for Molecular Simulations. *J Comput Chem* **1997**, *18* (12), 1463–1472. https://doi.org/10.1002/(SICI)1096-987X(199709)18:12<1463::AID-JCC4>3.0.CO;2-H.

(52) Miyamoto, S.; Kollman, P. A. Settle: An Analytical Version of the SHAKE and RATTLE Algorithm for Rigid Water Models. *J Comput Chem* **1992**, *13* (8), 952–962. https://doi.org/10.1002/jcc.540130805.

(53) Hünenberger, P. H. Thermostat Algorithms for Molecular Dynamics Simulations. In *Advances in Polymer Science*; Dr. Holm, C., Prof. Dr. Kremer, K., Eds.; Springer Berlin Heidelberg: Berlin, Heidelberg, 2005; Vol. 173, pp 105–147. https://doi.org/10.1007/b99427.

(54) Braun, E.; Moosavi, S. M.; Smit, B. Anomalous Effects of Velocity Rescaling Algorithms: The Flying Ice Cube Effect Revisited. *J Chem Theory Comput* **2018**, *14* (10), 5262–5272. https://doi.org/10.1021/acs.jctc.8b00446.

(55) Harvey, S. C.; Tan, R. K.-Z.; Cheatham, T. E. The Flying Ice Cube: Velocity Rescaling in Molecular Dynamics Leads to Violation of Energy Equipartition. *J Comput Chem* **1998**, *19* (7), 726–740. https://doi.org/10.1002/(sici)1096-987x(199805)19:7<726::aid-jcc4>3.0.co;2-s.

(56) Berendsen, H. J. C.; Postma, J. P. M.; Van Gunsteren, W. F.; Dinola, A.; Haak, J. R. Molecular Dynamics with Coupling to an External Bath. *J Chem Phys* **1984**, *81* (8), 3684–3690. https://doi.org/10.1063/1.448118.

(57) Nosé, S. A Molecular Dynamics Method for Simulations in the Canonical Ensemble. *Mol Phys* **1984**, *52* (2), 255–268. https://doi.org/10.1080/00268978400101201.

(58) Hoover, W. G. Canonical Dynamics: Equilibrium Phase-Space Distributions. *Phys Rev A (Coll Park)* **1985**, *31* (3), 1695–1697. https://doi.org/10.1103/PhysRevA.31.1695.

(59) Andersen, H. C. Molecular Dynamics Simulations at Constant Pressure and/or Temperature. *J Chem Phys* **1980**, *72* (4), 2384–2393. https://doi.org/10.1063/1.439486.

(60) Nosé, S.; Klein, M. L. Constant Pressure Molecular Dynamics for Molecular Systems. *Mol Phys* **1983**, *50* (5), 1055–1076. https://doi.org/10.1080/00268978300102851.

(61) Hoover, W. G. Constant-Pressure Equations of Motion. *Phys Rev A (Coll Park)* **1986**, *34* (3), 2499–2500. https://doi.org/10.1103/PhysRevA.34.2499.

(62) Parrinello, M.; Rahman, A. Polymorphic Transitions in Single Crystals: A New Molecular Dynamics Method. *J Appl Phys* **1981**, *52* (12), 7182–7190. https://doi.org/10.1063/1.328693.

(63) Ewald, P. P. Die Berechnung Optischer Und Elektrostatischer Gitterpotentiale. *Ann Phys* **1921**, *369* (3), 253–287. https://doi.org/10.1002/andp.19213690304.

(64) Darden, T.; York, D.; Pedersen, L. Particle Mesh Ewald: An N·log(N) Method for Ewald Sums in Large Systems. *J Chem Phys* **1993**, *98* (12), 10089–10092. https://doi.org/10.1063/1.464397.

(65) Gbaruko, B. C.; Igwe, J. C.; Gbaruko, P. N.; Nwokeoma, R. C. Gas Hydrates and Clathrates: Flow Assurance, Environmental and Economic Perspectives and the Nigerian Liquified Natural Gas Project. *J Pet Sci Eng* **2007**, *56* (1–3), 192–198. https://doi.org/10.1016/j.petrol.2005.12.011.

(66) McElwain, J. C.; Wade-Murphy, J.; Hesselbo, S. P. Changes in Carbon Dioxide during an Oceanic Anoxic Event Linked to Intrusion into Gondwana Coals. *Nature* **2005**, *435* (7041), 479–482. https://doi.org/10.1038/nature03618.

(67) Bohannon, J. Energy: Weighing the Climate Risks of an Untapped Fossil Fuel. *Science (1979)* **2008**, *319* (5871), 1753. https://doi.org/10.1126/science.319.5871.1753.

(68) Biastoch, A.; Treude, T.; Rüpke, L. H.; Riebesell, U.; Roth, C.; Burwicz, E. B.; Park, W.; Latif, M.; Böning, C. W.; Madec, G.; Wallmann, K. Rising Arctic Ocean Temperatures Cause Gas Hydrate Destabilization and Ocean Acidification. *Geophys Res Lett* **2011**, *38* (8). https://doi.org/10.1029/2011GL047222.

(69) Kvenvolden, K. A. Potential Effects of Gas Hydrate on Human Welfare. *Proceedings of the National Academy of Sciences* **1999**, *96* (7), 3420–3426. https://doi.org/10.1073/pnas.96.7.3420.

(70) Maslin, M.; Owen, M.; Betts, R.; Day, S.; Dunkley Jones, T.; Ridgwell, A. Gas Hydrates: Past and Future Geohazard? *Philosophical Transactions of the Royal Society A: Mathematical, Physical and Engineering Sciences* **2010**, *368* (1919), 2369–2393. https://doi.org/10.1098/rsta.2010.0065.

(71) Eslamimanesh, A.; Mohammadi, A. H.; Richon, D.; Naidoo, P.; Ramjugernath, D. Application of Gas Hydrate Formation in Separation Processes: A Review of Experimental Studies. *J Chem Thermodyn* **2012**, *46*, 62–71. https://doi.org/10.1016/j.jct.2011.10.006.

(72) Makogon, Y. F. Natural Gas Hydrates - A Promising Source of Energy. *J Nat Gas Sci Eng* **2010**, *2* (1), 49–59. https://doi.org/10.1016/j.jngse.2009.12.004.

(73) Koh, C. A.; Sloan, E. D.; Sum, A. K.; Wu, D. T. Fundamentals and Applications of Gas Hydrates. *Annu Rev Chem Biomol Eng* **2011**, *2* (1), 237–257. https://doi.org/10.1146/annurev-chembioeng-061010-114152.

(74) Mimachi, H.; Takeya, S.; Gotoh, Y.; Yoneyama, A.; Hyodo, K.; Takeda, T.; Murayama, T. Dissociation Behaviors of Methane Hydrate Formed from NaCl Solutions. *Fluid Phase Equilib* **2016**, *413*, 22–27. https://doi.org/10.1016/j.fluid.2015.10.029.

(75) Abay, H.; Svartaas, T. On the Kinetics of Methane Hydrate Formation: A Time-Dependent Kinetic Rate Model. *7th International Conference on Gas Hydrates* **2011**.

(76) Mohammadi, A. H.; Richon, D. Phase Equilibria of Clathrate Hydrates of Tetrahydrofuran + Hydrogen Sulfide and Tetrahydrofuran + Methane. *Ind Eng Chem Res* **2009**, *48* (16), 7838–7841. https://doi.org/10.1021/ie900774v.

(77) Seo, Y. T.; Kang, S. P.; Lee, H. Experimental Determination and Thermodynamic Modeling of Methane and Nitrogen Hydrates in the Presence of THF, Propylene Oxide, 1,4-Dioxane and Acetone. *Fluid Phase Equilib* **2001**, *189* (1–2), 99–110. https://doi.org/10.1016/S0378-3812(01)00580-5.

(78) Schicks, J. M.; Ripmeester, J. A. The Coexistence of Two Different Methane Hydrate Phases under Moderate Pressure and Temperature Conditions: Kinetic versus Thermodynamic Products. *Angewandte Chemie - International Edition* **2004**, *43* (25), 3310–3313. https://doi.org/10.1002/anie.200453898.

(79) Ohno, H.; Strobel, T. A.; Dec, S. F.; Sloan, E. D.; Koh, C. A. Raman Studies of Methane-Ethane Hydrate Metastability. *Journal of Physical Chemistry A* **2009**, *113* (9), 1711–1716. https://doi.org/10.1021/jp8010603.

(80) Staykova, D. K.; Kuhs, W. F.; Salamatin, A. N.; Hansen, T. Formation of Porous Gas Hydrates from Ice Powders: Diffraction Experiments and Multistage Model. *J Phys Chem B* **2003**, *107* (37), 10299–10311. https://doi.org/10.1021/jp027787v.

(81) Kondori, J.; James, L.; Zendehboudi, S. Molecular Scale Modeling Approach to Evaluate Stability and Dissociation of Methane and Carbon Dioxide Hydrates. *J Mol Liq* **2020**, *297*, 111503. https://doi.org/10.1016/j.molliq.2019.111503.

(82) Kondori, J.; Zendehboudi, S.; James, L. New Insights into Methane Hydrate Dissociation: Utilization of Molecular Dynamics Strategy. *Fuel* **2019**, *249* (March), 264–276. https://doi.org/10.1016/j.fuel.2019.02.125.

(83) Kondori, J.; Zendehboudi, S.; Hossain, M. E. A Review on Simulation of Methane Production from Gas Hydrate Reservoirs: Molecular Dynamics Prospective. *J Pet Sci Eng* **2017**, *159* (March), 754–772. https://doi.org/10.1016/j.petrol.2017.09.073.

(84) Myshakin, E. M.; Jiang, H.; Warzinski, R. P.; Jordan, K. D. Molecular Dynamics Simulations of Methane Hydrate Decomposition †. *J Phys Chem A* **2009**, *113* (10), 1913–1921. https://doi.org/10.1021/jp807208z.

(85) Walsh, M. R.; Beckham, G. T.; Koh, C. A.; Sloan, E. D.; Wu, D. T.; Sum, A. K. Methane Hydrate Nucleation Rates from Molecular Dynamics Simulations: Effects of Aqueous Methane Concentration, Interfacial Curvature, and System Size. *Journal*

of Physical Chemistry C **2011**, *115* (43), 21241–21248. https://doi.org/10.1021/jp206483q.

(86) Zhang, Z.; Walsh, M. R.; Guo, G.-J. Microcanonical Molecular Simulations of Methane Hydrate Nucleation and Growth: Evidence That Direct Nucleation to SI Hydrate Is among the Multiple Nucleation Pathways. *Phys. Chem. Chem. Phys.* **2015**, *17* (14), 8870–8876. https://doi.org/10.1039/C5CP00098J.

(87) Geng, C. Y.; Wen, H.; Zhou, H. Molecular Simulation of the Potential of Methane Reoccupation during the Replacement of Methane Hydrate by CO2. *Journal of Physical Chemistry A* **2009**, *113* (18), 5463–5469. https://doi.org/10.1021/jp811474m.

(88) Walsh, M. R.; Koh, C. A.; Sloan, E. D.; Sum, A. K.; Wu, D. T. Microsecond Simulations of Spontaneous Methane Hydrate Nucleation and Growth. *Science (1979)* **2009**, *326* (5956), 1095–1098. https://doi.org/10.1126/science.1174010.

(89) Walsh, M. R.; Rainey, J. D.; Lafond, P. G.; Park, D. H.; Beckham, G. T.; Jones, M. D.; Lee, K. H.; Koh, C. A.; Sloan, E. D.; Wu, D. T.; Sum, A. K. The Cages, Dynamics, and Structuring of Incipient Methane Clathrate Hydrates. *Physical Chemistry Chemical Physics* **2011**, *13* (44), 19951–19959. https://doi.org/10.1039/c1cp21899a.

(90) Kim, D.; Ahn, Y. H.; Kim, S. J.; Lee, J. Y.; Lee, J.; Seo, Y. J.; Lee, H. Gas Hydrate in Crystalline-Swelled Clay: The Effect of Pore Dimension on Hydrate Formation and Phase Equilibria. *Journal of Physical Chemistry C* **2015**, *119* (38), 22148–22153. https://doi.org/10.1021/acs.jpcc.5b03229.

(91) Kim, D.; Lee, H. Phase Behavior of Gas Hydrates in Nanoporous Materials: Review. *Korean Journal of Chemical Engineering* **2016**, *33* (7), 1977–1988. https://doi.org/10.1007/s11814-016-0064-z.

(92) Cha, S. B.; Ouar, H.; Wildeman, T. R.; Sloan, E. D. A Third-Surface Effect on Hydrate Formation. *Journal of Physical Chemistry* **1988**, *92* (23), 6492–6494.

(93) Handa, Y. P.; Stupin, D. Yu. Thermodynamic Properties and Dissociation Characteristics of Methane and Propane Hydrates in 70-.ANG.-Radius Silica Gel Pores. *J Phys Chem* **1992**, *96* (21), 8599–8603. https://doi.org/10.1021/j100200a071.

(94) Uchida, T.; Ebinuma, T.; Ishizaki, T. Dissociation Condition Measurements of Methane Hydrate in Confined Small Pores of Porous Glass. *J Phys Chem B* **1999**, *103* (18), 3659–3662. https://doi.org/10.1021/jp984559l.

(95) Park, S. H.; Sposito, G. Do Montmorillonite Surfaces Promote Methane Hydrate Formation? Monte Carlo and Molecular Dynamics Simulations. *Journal of Physical Chemistry B* **2003**, *107* (10), 2281–2290. https://doi.org/10.1021/jp021427q.

(96) Cygan, R. T.; Guggenheim, S.; Van Koster Groos, A. F. Molecular Models for the Intercalation of Methane Hydrate Complexes in Montmorillonite Clay. *Journal of Physical Chemistry B* **2004**, *108* (39), 15141–15149. https://doi.org/10.1021/jp037900x.

(97) Martos-Villa, R.; Guggenheim, S.; Mata, M. P.; Sainz-Díaz, C. I.; Nieto, F. Interaction of Methane Hydrate Complexes with Smectites: Experimental Results Compared to Molecular Models. *American Mineralogist* **2014**, *99* (2–3), 401–414. https://doi.org/10.1515/am.2014.4570.

(98) Bai, D.; Chen, G.; Zhang, X.; Wang, W. Microsecond Molecular Dynamics Simulations of the Kinetic Pathways of Gas Hydrate Formation from Solid Surfaces. *Langmuir* **2011**, *27* (10), 5961–5967. https://doi.org/10.1021/la105088b.

(99) Nath Chakraborty, S.; Gelb, L. D. A Monte Carlo Simulation Study of Methane Clathrate Hydrates Confined in Slit-Shaped Pores. *J Phys Chem B* **2012**, *116* (7), 2183–2197. https://doi.org/10.1021/jp205241n.

(100) Bagherzadeh, S. A.; Englezos, P.; Alavi, S.; Ripmeester, J. A. Molecular Modeling of the Dissociation of Methane Hydrate in Contact with a Silica Surface. *Journal of Physical Chemistry B* **2012**, *116* (10), 3188–3197. https://doi.org/10.1021/jp2086544.

(101) Bagherzadeh, S. A.; Englezos, P.; Alavi, S.; Ripmeester, J. A. Influence of Hydrated Silica Surfaces on Interfacial Water in the Presence of Clathrate Hydrate Forming Gases. *Journal of Physical Chemistry C* **2012**, *116* (47), 24907–24915. https://doi.org/10.1021/jp305529d.

(102) Liang, S.; Rozmanov, D.; Kusalik, P. G. Crystal Growth Simulations of Methane Hydrates in the Presence of Silica Surfaces. *Physical Chemistry Chemical Physics* **2011**, *13* (44), 19856–19864. https://doi.org/10.1039/c1cp21810g.

(103) Liang, S.; Kusalik, P. G. The Nucleation of Gas Hydrates near Silica Surfaces. *Can J Chem* **2015**, *93* (8), 791–798. https://doi.org/10.1139/cjc-2014-0443.

(104) Yan, K. F.; Li, X. Sen; Xu, C. G.; Lv, Q. N.; Ruan, X. K. Molecular Dynamics Simulation of the Intercalation Behaviors of Methane Hydrate in Montmorillonite. *J Mol Model* **2014**, *20* (6). https://doi.org/10.1007/s00894-014-2311-8.

(105) Nguyen, N. N.; Nguyen, A. V.; Steel, K. M.; Dang, L. X.; Galib, M. Interfacial Gas Enrichment at Hydrophobic Surfaces and the Origin of Promotion of Gas Hydrate Formation by Hydrophobic Solid Particles. *Journal of Physical Chemistry C* **2017**, *121* (7), 3830–3840. https://doi.org/10.1021/acs.jpcc.6b07136.

(106) He, Z.; Linga, P.; Jiang, J. CH4 Hydrate Formation between Silica and Graphite Surfaces: Insights from Microsecond Molecular Dynamics Simulations. *Langmuir* **2017**, *33* (43), 11956–11967.

(107) Li, Y.; Chen, M.; Liu, C.; Song, H.; Yuan, P.; Zhang, B.; Liu, D.; Du, P. Effects of Layer-Charge Distribution of 2:1 Clay Minerals on Methane Hydrate Formation: A Molecular Dynamics Simulation Study. *Langmuir* **2020**. https://doi.org/10.1021/acs.langmuir.0c00183.

(108) Ladd, A. J. C.; Woodcock, L. V. Triple-Point Coexistence Properties of the Lennard-Jones System. *Chem Phys Lett* **1977**, *51* (1), 155–159. https://doi.org/10.1016/0009-2614(77)85375-X.

(109) Conde, M. M.; Vega, C. Determining the Three-Phase Coexistence Line in Methane Hydrates Using Computer Simulations. *Journal of Chemical Physics* **2010**, *133* (6). https://doi.org/10.1063/1.3466751.

(110) Costandy, J.; Michalis, V. K.; Tsimpanogiannis, I. N.; Stubos, A. K.; Economou, I. G. The Role of Intermolecular Interactions in the Prediction of the Phase Equilibria of Carbon Dioxide Hydrates. *Journal of Chemical Physics* **2015**, *143* (9). https://doi.org/10.1063/1.4929805.

(111) Michalis, V. K.; Costandy, J.; Tsimpanogiannis, I. N.; Stubos, A. K.; Economou, I. G. Prediction of the Phase Equilibria of Methane Hydrates Using the Direct Phase Coexistence Methodology. *Journal of Chemical Physics* **2015**, *142* (4). https://doi.org/10.1063/1.4905572.

(112) Luis, D. P.; López-Lemus, J.; Maspoch, M. Ll.; Franco-Urquiza, E. A.; Saint-Martin, H. Methane Hydrate: Shifting the Coexistence Temperature to Higher Temperatures with an External Electric Field. *Mol Simul* **2016**, *42* (12), 1014–1023. https://doi.org/10.1080/08927022.2016.1139704.

(113) Smirnov, G. S.; Stegailov, V. V. Melting and Superheating of SI Methane Hydrate: Molecular Dynamics Study. *Journal of Chemical Physics* **2012**, *136* (4). https://doi.org/10.1063/1.3679860.

(114) Luis, D. P.; García-González, A.; Saint-Martin, H. A Theoretical Study of the Hydration of Methane, from the Aqueous Solution to the SI Hydrate-Liquid Water-Gas Coexistence. *Int J Mol Sci* **2016**, *17* (6), 378. https://doi.org/10.3390/ijms17060378.

(115) Jin, D.; Coasne, B. Molecular Simulation of the Phase Diagram of Methane Hydrate: Free Energy Calculations, Direct Coexistence Method, and Hyperparallel Tempering. *Langmuir* **2017**, *33* (42), 11217–11230. https://doi.org/10.1021/acs.langmuir.7b02238.

(116) Docherty, H.; Galindo, A.; Vega, C.; Sanz, E. A Potential Model for Methane in Water Describing Correctly the Solubility of the Gas and the Properties of the Methane Hydrate. *Journal of Chemical Physics* **2006**, *125* (7). https://doi.org/10.1063/1.2335450.

(117) Zhang, Z.; Walsh, M. R.; Guo, G.-J. Microcanonical Molecular Simulations of Methane Hydrate Nucleation and Growth: Evidence That Direct Nucleation to SI Hydrate Is among the Multiple Nucleation Pathways. *Phys. Chem. Chem. Phys.* **2015**, *17* (14), 8870–8876. https://doi.org/10.1039/C5CP00098J.

(118) Zhang, Z.; Liu, C.-J.; Walsh, M. R.; Guo, G.-J. Effects of Ensembles on Methane Hydrate Nucleation Kinetics. *Phys. Chem. Chem. Phys.* **2016**, *18* (23), 15602–15608. https://doi.org/10.1039/C6CP02171A.

(119) Luis, D. P.; López-Lemus, J.; Maspoch, M. L.; Franco-Urquiza, E. A.; Saint-Martin, H. Methane Hydrate: Shifting the Coexistence Temperature to Higher Temperatures with an External Electric Field. *Mol Simul* **2016**, *42* (12), 1014–1023. https://doi.org/10.1080/08927022.2016.1139704.

(120) Luis, D. P.; López-Lemus, J.; Mayorga, M.; Romero-Salazar, L. Performance of Rigid Water Models in the Phase Transition of Clathrates. *Mol Simul* **2010**, *36* (1), 35–40. https://doi.org/10.1080/08927020903096072.

(121) Yan, K. F.; Li, X. Sen; Chen, Z. Y.; Xia, Z. M.; Xu, C. G.; Zhang, Z. Molecular Dynamics Simulation of the Crystal Nucleation and Growth Behavior of Methane Hydrate in the Presence of the Surface and Nanopores of Porous Sediment. *Langmuir* **2016**, *32* (31), 7975–7984. https://doi.org/10.1021/acs.langmuir.6b01601.

(122) Molinero, V.; Moore, E. B. Water Modeled As an Intermediate Element between Carbon and Silicon. *J Phys Chem B* **2009**, *113* (13), 4008–4016. https://doi.org/10.1021/jp805227c.

(123) Jacobson, L. C.; Hujo, W.; Molinero, V. Nucleation Pathways of Clathrate Hydrates: Effect of Guest Size and Solubility. *Journal of Physical Chemistry B* **2010**, *114* (43), 13796–13807. https://doi.org/10.1021/jp107269q.

(124) Berendsen, H. J. C.; Postma, J. P. M.; van Gunsteren, W. F.; Hermans, J. Interaction Models for Water in Relation to Protein Hydration. In *Intermolecular Forces*; 1981; Vol. 31, pp 331–342. https://doi.org/10.1007/978-94-015-7658-1_21.

(125) Berendsen, H. J. C.; Grigera, J. R.; Straatsma, T. P. The Missing Term in Effective Pair Potentials. *Journal of Physical Chemistry* **1987**, *91* (24), 6269–6271. https://doi.org/10.1021/j100308a038.

(126) Jorgensen, W. L.; Chandrasekhar, J.; Madura, J. D.; Impey, R. W.; Klein, M. L. Comparison of Simple Potential Functions for Simulating Liquid Water. *J Chem Phys* **1983**, *79* (2), 926–935. https://doi.org/10.1063/1.445869.

(127) Abascal, J. L.; Vega, C. A General Purpose Model for the Condensed Phases of Water: TIP4P/2005. *J Chem Phys* **2005**, *123* (23), 234505. https://doi.org/10.1063/1.2121687.

(128) Abascal, J. L. F.; Sanz, E.; Fernández, R. G.; Vega, C. A Potential Model for the Study of Ices and Amorphous Water: TIP4P/Ice. *Journal of Chemical Physics* **2005**, *122* (23). https://doi.org/10.1063/1.1931662.

(129) Alejandre, J.; Chapela, G. A.; Saint-Martin, H.; Mendoza, N. A Non-Polarizable Model of Water That Yields the Dielectric Constant and the Density Anomalies of the Liquid: TIP4Q. *Physical Chemistry Chemical Physics* **2011**, *13*, 19728–19740. https://doi.org/10.1039/c1cp20858f.

(130) Mahoney, M. W.; Jorgensen, W. L. A Five-Site Model for Liquid Water and the Reproduction of the Density Anomaly by Rigid, Nonpolarizable Potential Functions. *Journal of Chemical Physics* **2000**, *112* (20), 8910–8922. https://doi.org/10.1063/1.481505.

(131) Jacobson, L. C.; Hujo, W.; Molinero, V. Amorphous Precursors in the Nucleation of Clathrate Hydrates. *J Am Chem Soc* **2010**, *132* (33), 11806–11811. https://doi.org/10.1021/ja1051445.

(132) He, Z.; Linga, P.; Jiang, J. What Are the Key Factors Governing the Nucleation of CO2 Hydrate? *Physical Chemistry Chemical Physics* **2017**, *19* (24), 15657–15661. https://doi.org/10.1039/C7CP01350G.

(133) He, Z.; Gupta, K. M.; Linga, P.; Jiang, J. Molecular Insights into the Nucleation and Growth of CH4 and CO2 Mixed Hydrates from Microsecond Simulations. *Journal of Physical Chemistry C* **2016**, *120* (44), 25225–25236. https://doi.org/10.1021/acs.jpcc.6b07780.

(134) Martin, M. G.; Siepmann, J. I. Transferable Potentials for Phase Equilibria. 1. United-Atom Description of n -Alkanes. *J Phys Chem B* **1998**, *102* (14), 2569–2577. https://doi.org/10.1021/jp972543+.

(135) Lopes, P. E. M.; Murashov, V.; Tazi, M.; Demchuk, E.; MacKerell, A. D. Development of an Empirical Force Field for Silica. Application to the Quartz-Water Interface. *Journal of Physical Chemistry B* **2006**, *110* (6), 2782–2792. https://doi.org/10.1021/jp055341j.

(136) Kirchner, M. T.; Boese, R.; Billups, W. E.; Norman, L. R. Gas Hydrate Single-Crystal Structure Analyses. *J Am Chem Soc* **2004**, *126* (30), 9407–9412. https://doi.org/10.1021/ja049247c.

(137) Abraham, M. J.; Murtola, T.; Schulz, R.; Páll, S.; Smith, J. C.; Hess, B.; Lindah, E. Gromacs: High Performance Molecular Simulations through Multi-Level Parallelism from Laptops to Supercomputers. *SoftwareX* **2015**, *1–2*, 19–25. https://doi.org/10.1016/j.softx.2015.06.001.

(138) Essmann, U.; Perera, L.; Berkowitz, M. L.; Darden, T.; Lee, H.; Pedersen, L. G. A Smooth Particle Mesh Ewald Method. *J Chem Phys* **1995**, *103* (19), 8577–8593. https://doi.org/10.1063/1.470117.

(139) Berendsen, H. J. C.; Postma, J. P. M.; Van Gunsteren, W. F.; Dinola, A.; Haak, J. R. Molecular Dynamics with Coupling to an External Bath. *J Chem Phys* **1984**, *81* (8), 3684–3690. https://doi.org/10.1063/1.448118.

(140) Moridis, G. J.; Kowalsky, M. B. Depressurization-Induced Gas Production from Class-1 Hydrate Deposits. *Proceedings - SPE Annual Technical Conference and Exhibition* **2005**, No. March, 4655–4677.

(141) Rodger, P. M.; Forester, T. R.; Smith, W. Simulations of the Methane Hydrate/Methane Gas Interface near Hydrate Forming Conditions Conditions. *Fluid Phase Equilib* **1996**, *116* (1–2), 326–332. https://doi.org/10.1016/0378-3812(95)02903-6.

(142) Fidler, J.; Rodger, P. M. Solvation Structure around Aqueous Alcohols. *J Phys Chem B* **1999**, *103* (36), 7695–7703. https://doi.org/10.1021/jp9907903.

(143) Anderson, A.; Ashurst, W. R. Interfacial Water Structure on a Highly Hydroxylated Silica Film. *Langmuir* **2009**, *25* (19), 11549–11554. https://doi.org/10.1021/la901459b.

(144) Guo, G. Cage Adsorption Hypothesis on Hydrate Nucleation Mechanisms. In *Geophysics*; 2011.

(145) Sun, T.; Feng, L.; Gao, X.; Jiang, L. Bioinspired Surfaces with Special Wettability. *Acc Chem Res* **2005**, *38* (8), 644–652. https://doi.org/10.1021/ar040224c.

(146) Seddon, J. R. T.; Lohse, D.; Ducker, W. A.; Craig, V. S. J. A Deliberation on Nanobubbles at Surfaces and in Bulk. *ChemPhysChem* **2012**, *13* (8), 2179–2187. https://doi.org/10.1002/cphc.201100900.

(147) Alheshibri, M.; Qian, J.; Jehannin, M.; Craig, V. S. J. A History of Nanobubbles. *Langmuir* **2016**, *32* (43), 11086–11100. https://doi.org/10.1021/acs.langmuir.6b02489.

(148) Bishnoi, P. R.; Natarajan, V.; Kalogerakis, N. A Unified Description of the Kinetics of Hydrate Nucleation, Growth, and Decomposition. *International Conference on Natural Gas Hydrates* **1994**, *715* (1), 311–322. https://doi.org/10.1111/j.1749-6632.1994.tb38843.x.

(149) Phan, A.; Cole, D. R.; Striolo, A. Aqueous Methane in Slit-Shaped Silica Nanopores: High Solubility and Traces of Hydrates. *Journal of Physical Chemistry C* **2014**, *118* (9), 4860–4868. https://doi.org/10.1021/jp500081t.

(150) IEA. *World Energy Outlook 2020*; 2020. https://doi.org/10.1787/20725302.

(151) IEA. *Global Energy Review 2021*; 2021. https://doi.org/10.1787/a60abbf2-en.

(152) Ilgen, A. G.; Heath, J. E.; Akkutlu, I. Y.; Bryndzia, L. T.; Cole, D. R.; Kharaka, Y. K.; Kneafsey, T. J.; Milliken, K. L.; Pyrak-Nolte, L. J.; Suarez-Rivera, R. Shales at All Scales: Exploring Coupled Processes in Mudrocks. *Earth Sci Rev* **2017**, *166*, 132–152. https://doi.org/10.1016/j.earscirev.2016.12.013.

(153) Josh, M.; Esteban, L.; Delle Piane, C.; Sarout, J.; Dewhurst, D. N.; Clennell, M. B. Laboratory Characterisation of Shale Properties. *J Pet Sci Eng* **2012**, *88–89*, 107–124. https://doi.org/10.1016/j.petrol.2012.01.023.

(154) Saraji, S.; Piri, M. The Representative Sample Size in Shale Oil Rocks and Nano-Scale Characterization of Transport Properties. *Int J Coal Geol* **2015**, *146*, 42–54. https://doi.org/10.1016/j.coal.2015.04.005.

(155) Striolo, A.; Cole, D. R. Understanding Shale Gas: Recent Progress and Remaining Challenges. *Energy and Fuels* **2017**, *31* (10), 10300–10310. https://doi.org/10.1021/acs.energyfuels.7b01023.

(156) Wang, J.; Dong, M.; Yang, Z.; Gong, H.; Li, Y. Investigation of Methane Desorption and Its Effect on the Gas Production Process from Shale: Experimental and

Mathematical Study. *Energy & Fuels* **2017**, *31* (1), 205–216. https://doi.org/10.1021/acs.energyfuels.6b02033.

(157) Ishida, T.; Aoyagi, K.; Niwa, T.; Chen, Y.; Murata, S.; Chen, Q.; Nakayama, Y. Acoustic Emission Monitoring of Hydraulic Fracturing Laboratory Experiment with Supercritical and Liquid CO2. *Geophys Res Lett* **2012**, *39* (16). https://doi.org/10.1029/2012GL052788.

(158) Fathi, E.; Akkutlu, I. Y. Multi-Component Gas Transport and Adsorption Effects during CO2 Injection and Enhanced Shale Gas Recovery. *Int J Coal Geol* **2014**, *123*, 52–61. https://doi.org/10.1016/j.coal.2013.07.021.

(159) Hughes, J. D. Energy: A Reality Check on the Shale Revolution. *Nature* **2013**, *494* (7437), 307–308. https://doi.org/10.1038/494307a.

(160) King, G. E. Thirty Years of Gas Shale Fracturing: What Have We Learned? *Proceedings - SPE Annual Technical Conference and Exhibition*. September 19, 2010, pp 900–949. https://doi.org/10.2118/133456-ms.

(161) Baihly, J.; Altman, R.; Malpani, R.; Luo, F. Shale Gas Production Decline Trend Comparison over Time and Basins. *Proceedings - SPE Annual Technical Conference and Exhibition*. September 19, 2010, pp 5276–5300. https://doi.org/10.2118/135555-ms.

(162) Selley, R. C. Sedimentary Rocks: Mineralogy and Classification. In *Encyclopedia of Geology*; Selley, R. C., Cocks, L. R. M., Plimer, I. R. B. T.-E. of G., Eds.; Elsevier: Oxford, 2004; pp 25–37. https://doi.org/10.1016/B0-12-369396-9/00304-X.

(163) Zhou, S.; Xue, H.; Ning, Y.; Guo, W.; Zhang, Q. Experimental Study of Supercritical Methane Adsorption in Longmaxi Shale: Insights into the Density of Adsorbed Methane. *Fuel* **2018**, *211*, 140–148. https://doi.org/10.1016/j.fuel.2017.09.065.

(164) Li, J.; Zhou, S.; Gaus, G.; Li, Y.; Ma, Y.; Chen, K.; Zhang, Y. Characterization of Methane Adsorption on Shale and Isolated Kerogen from the Sichuan Basin under Pressure up to 60 MPa: Experimental Results and Geological Implications. *Int J Coal Geol* **2018**, *189*, 83–93. https://doi.org/10.1016/j.coal.2018.02.020.

(165) Kelemen, S. R.; Afeworki, M.; Gorbaty, M. L.; Sansone, M.; Kwiatek, P. J.; Walters, C. C.; Freund, H.; Siskin, M.; Bence, A. E.; Curry, D. J.; Solum, M.; Pugmire, R. J.; Vandenbroucke, M.; Leblond, M.; Behar, F. Direct Characterization of Kerogen by X-Ray and Solid-State 13C Nuclear Magnetic Resonance Methods. *Energy and Fuels* **2007**, *21* (3), 1548–1561. https://doi.org/10.1021/ef060321h.

(166) Behar, F.; Vandenbroucke, M. Chemical Modelling of Kerogens. *Org Geochem* **1987**, *11* (1), 15–24. https://doi.org/10.1016/0146-6380(87)90047-7.

(167) Zhang, L.; LeBoeuf, E. J. A Molecular Dynamics Study of Natural Organic Matter: 1. Lignin, Kerogen and Soot. *Org Geochem* **2009**, *40* (11), 1132–1142. https://doi.org/10.1016/j.orggeochem.2009.08.002.

(168) Siskin, M.; Scouten, C. G.; Rose, K. D.; Aczel, T.; Colgrove, S. G.; Pabst, R. E. Detailed Structural Characterization of the Organic Material in Rundle Ramsay Crossing and Green River Oil Shales. In *Composition, Geochemistry and Conversion of Oil Shales*; Snape, C., Ed.; Springer Netherlands: Dordrecht, 1995; pp 143–158. https://doi.org/10.1007/978-94-011-0317-6_9.

(169) Orendt, A. M.; Pimienta, I. S. O.; Badu, S. R.; Solum, M. S.; Pugmire, R. J.; Facelli, J. C.; Locke, D. R.; Chapman, K. W.; Chupas, P. J.; Winans, R. E. Three-Dimensional Structure of the Siskin Green River Oil Shale Kerogen Model: A Comparison between Calculated and Observed Properties. *Energy and Fuels* **2013**, *27* (2), 702–710. https://doi.org/10.1021/ef3017046.

(170) Zhang, Z.; Jamili, A. Modeling the Kerogen 3D Molecular Structure. *Society of Petroleum Engineers - SPE/CSUR Unconventional Resources Conference* **2015**, 1–14. https://doi.org/10.2118/175991-ms.

(171) Ungerer, P.; Collell, J.; Yiannourakou, M. Molecular Modeling of the Volumetric and Thermodynamic Properties of Kerogen: Influence of Organic Type and Maturity. *Energy and Fuels* **2015**, *29* (1), 91–105. https://doi.org/10.1021/ef502154k.

(172) Lee, H.; Shakib, F. A.; Liu, K.; Liu, B.; Bubach, B.; Varma, R. S.; Jang, H. W.; Shokouhimher, M.; Ostadhassan, M. Adsorption Based Realistic Molecular Model of

Amorphous Kerogen. *RSC Adv* **2020**, *10* (39), 23312–23320. https://doi.org/10.1039/d0ra04453a.

(173) Ho, T. A.; Criscenti, L. J.; Wang, Y. Nanostructural Control of Methane Release in Kerogen and Its Implications to Wellbore Production Decline. *Sci Rep* **2016**, *6* (June), 1–9. https://doi.org/10.1038/srep28053.

(174) Ho, T. A.; Wang, Y.; Xiong, Y.; Criscenti, L. J. Differential Retention and Release of CO2 and CH4 in Kerogen Nanopores: Implications for Gas Extraction and Carbon Sequestration. *Fuel* **2018**, *220* (January), 1–7. https://doi.org/10.1016/j.fuel.2018.01.106.

(175) Ho, T. A.; Wang, Y.; Criscenti, L. J. Chemo-Mechanical Coupling in Kerogen Gas Adsorption/Desorption. *Physical Chemistry Chemical Physics* **2018**, *20* (18), 12390–12395. https://doi.org/10.1039/c8cp01068d.

(176) Kazemi, M.; Maleki, H.; Takbiri-Borujeni, A. Molecular Dynamics Study of Transport and Storage of Methane in Kerogen. *SPE Eastern Regional Meeting* **2016**, *2016-Janua* (September), 13–15. https://doi.org/10.2118/184058-MS.

(177) Michalec, L.; Lísal, M. Molecular Simulation of Shale Gas Adsorption onto Overmature Type II Model Kerogen with Control Microporosity. *Mol Phys* **2017**, *115* (9–12), 1086–1103. https://doi.org/10.1080/00268976.2016.1243739.

(178) Sui, H.; Yao, J. Effect of Surface Chemistry for CH4/CO2 Adsorption in Kerogen: A Molecular Simulation Study. *J Nat Gas Sci Eng* **2016**, *31*, 738–746. https://doi.org/10.1016/j.jngse.2016.03.097.

(179) Wang, Z.; Li, Y.; Liu, H.; Zeng, F.; Guo, P.; Jiang, W. Study on the Adsorption, Diffusion and Permeation Selectivity of Shale Gas in Organics. *Energies (Basel)* **2017**, *10* (1), 1–15. https://doi.org/10.3390/en10010142.

(180) Pathak, M.; Kweon, H.; Deo, M.; Huang, H. Kerogen Swelling and Confinement: Its Implication on Fluid Thermodynamic Properties in Shales. *Sci Rep* **2017**, *7* (1), 12530. https://doi.org/10.1038/s41598-017-12982-4.

(181) Vasileiadis, M.; Peristeras, L. D.; Papavasileiou, K. D.; Economou, I. G. Modeling of Bulk Kerogen Porosity: Methods for Control and Characterization. *Energy and Fuels* **2017**, *31* (6), 6004–6018. https://doi.org/10.1021/acs.energyfuels.7b00626.

(182) Vasileiadis, M.; Peristeras, L. D.; Papavasileiou, K. D.; Economou, I. G. Transport Properties of Shale Gas in Relation to Kerogen Porosity. *Journal of Physical Chemistry C* **2018**, *122* (11), 6166–6177. https://doi.org/10.1021/acs.jpcc.8b00162.

(183) Zhao, T.; Li, X.; Zhao, H.; Li, M. Molecular Simulation of Adsorption and Thermodynamic Properties on Type II Kerogen: Influence of Maturity and Moisture Content. *Fuel* **2017**, *190*, 198–207. https://doi.org/10.1016/j.fuel.2016.11.027.

(184) Huang, L.; Ning, Z.; Wang, Q.; Qi, R.; Cheng, Z.; Wu, X.; Zhang, W.; Qin, H. Molecular Insights into Kerogen Deformation Induced by CO2/CH4 Sorption: Effect of Maturity and Moisture. *Energy and Fuels* **2019**, *33* (6), 4792–4805. https://doi.org/10.1021/acs.energyfuels.9b00409.

(185) Alafnan, S.; Solling, T.; Mahmoud, M. Effect of Kerogen Thermal Maturity on Methane Adsorption Capacity: A Molecular Modeling Approach. *Molecules* **2020**, *25* (16). https://doi.org/10.3390/molecules25163764.

(186) Tesson, S.; Firoozabadi, A. Methane Adsorption and Self-Diffusion in Shale Kerogen and Slit Nanopores by Molecular Simulations. *Journal of Physical Chemistry C* **2018**, *122* (41), 23528–23542. https://doi.org/10.1021/acs.jpcc.8b07123.

(187) Wu, T.; Firoozabadi, A. Effect of Microstructural Flexibility on Methane Flow in Kerogen Matrix by Molecular Dynamics Simulations. *Journal of Physical Chemistry C* **2019**, *123* (17), 10874–10880. https://doi.org/10.1021/acs.jpcc.8b12328.

(188) He, J.; Ju, Y.; Lammers, L.; Kulasinski, K.; Zheng, L. Tortuosity of Kerogen Pore Structure to Gas Diffusion at Molecular- and Nano-Scales: A Molecular Dynamics Simulation. *Chem Eng Sci* **2020**, *215*, 115460. https://doi.org/10.1016/j.ces.2019.115460.

(189) Rezlerová, E.; Brennan, J. K.; Lísal, M. Methane and Carbon Dioxide in Dual-Porosity Organic Matter: Molecular Simulations of Adsorption and Diffusion. *AIChE Journal* **2020**, No. April 2020, 1–17. https://doi.org/10.1002/aic.16655.

(190) Sun, Q.; Liu, W.; Zhang, N. Molecular Insights into Recovery of Shale Gas by CO2 Injection in Kerogen Slit Nanopores. *J Nat Gas Sci Eng* **2021**, *90* (March), 1–15. https://doi.org/10.1016/j.jngse.2021.103903.

(191) Li, W.; Zhang, M.; Nan, Y.; Pang, W.; Jin, Z. Molecular Dynamics Study on CO2 Storage in Water-Filled Kerogen Nanopores in Shale Reservoirs: Effects of Kerogen Maturity and Pore Size. *Langmuir* **2021**. https://doi.org/10.1021/acs.langmuir.0c03232.

(192) Chong, L.; Sanguinito, S.; Goodman, A. L.; Myshakin, E. M. Molecular Characterization of Carbon Dioxide, Methane, and Water Adsorption in Micropore Space of Kerogen Matrix. *Fuel* **2021**, *283*, 119254.

(193) Zhou, W.; Zhang, Z.; Wang, H.; Yang, X. Molecular Investigation of CO2/CH4 Competitive Adsorption and Confinement in Realistic Shale Kerogen. *Nanomaterials* **2019**, *9* (12). https://doi.org/10.3390/nano9121646.

(194) Sun, H. Compass: An Ab Initio Force-Field Optimized for Condensed-Phase Applications - Overview with Details on Alkane and Benzene Compounds. *Journal of Physical Chemistry B* **1998**, *102* (38), 7338–7364. https://doi.org/10.1021/jp980939v.

(195) Hagler, A. T.; Lifson, S.; Dauber, P. Consistent Force Field Studies of Intermolecular Forces in Hydrogen-Bonded Crystals. 2. A Benchmark for the Objective Comparison of Alternative Force Fields. *J Am Chem Soc* **1979**, *101* (18), 5122–5130. https://doi.org/10.1021/ja00512a002.

(196) Mayo, S. L.; Olafson, B. D.; Goddard, W. A. DREIDING: A Generic Force Field for Molecular Simulations. *Journal of Physical Chemistry* **1990**, *94* (26), 8897–8909. https://doi.org/10.1021/j100389a010.

(197) Wang, J.; Wolf, R. M.; Caldwell, J. W.; Kollman, P. A.; Case, D. A. Development and Testing of a General Amber Force Field. *J Comput Chem* **2004**, *25* (9), 1157–1174. https://doi.org/10.1002/jcc.20035.

(198) Harris, J. G.; Yung, K. H. Carbon Dioxide's Liquid-Vapor Coexistence Curve and Critical Properties as Predicted by a Simple Molecular Model. *Journal of Physical Chemistry* **1995**, *99* (31), 12021–12024. https://doi.org/10.1021/j100031a034.

(199) Berendsen, H. J. C.; Postma, J. P. M.; van Gunsteren, W. F.; Hermans, J. Interaction Models for Water in Relation to Protein Hydration. In *Intermolecular Forces*; Pullman, B., Ed.; Springer Netherlands: Dordrecht, 1981; Vol. 31, pp 331–342. https://doi.org/10.1007/978-94-015-7658-1_21.

(200) Dubbeldam, D.; Calero, S.; Ellis, D. E.; Snurr, R. Q. RASPA: Molecular Simulation Software for Adsorption and Diffusion in Flexible Nanoporous Materials. *Mol Simul* **2016**, *42* (2), 81–101. https://doi.org/10.1080/08927022.2015.1010082.

(201) Dubbeldam, D.; Torres-Knoop, A.; Walton, K. S. On the Inner Workings of Monte Carlo Codes. *Mol Simul* **2013**, *39* (14–15), 1253–1292. https://doi.org/10.1080/08927022.2013.819102.

(202) Bussi, G.; Donadio, D.; Parrinello, M. Canonical Sampling through Velocity Rescaling. *Journal of Chemical Physics* **2007**, *126* (1), 14101. https://doi.org/10.1063/1.2408420.

(203) Sarkisov, L.; Bueno-Perez, R.; Sutharson, M.; Fairen-Jimenez, D. Materials Informatics with PoreBlazer v4.0 and the CSD MOF Database. *Chemistry of Materials* **2020**, *32* (23), 9849–9867. https://doi.org/10.1021/acs.chemmater.0c03575.

(204) Talu, O.; Myers, A. L. Reference Potentials for Adsorption of Helium, Argon, Methane, and Krypton in High-Silica Zeolites. *Colloids Surf A Physicochem Eng Asp* **2001**, *187–188*, 83–93. https://doi.org/10.1016/S0927-7757(01)00628-8.

(205) Hirschfelder, J. O.; Curtiss, C. F.; Bird, R. B. *Molecular Theory of Gases and Liquids*; Curtiss, C. F. (Charles F., Bird, R. B. (Robert B., Laboratory, U. of Wisconsin. N. R., Eds.; John Wiley & Sons: New York, 1954.

(206) Düren, T.; Millange, F.; Férey, G.; Walton, K. S.; Snurr, R. Q. Calculating Geometric Surface Areas as a Characterization Tool for Metal - Organic Frameworks. *Journal of Physical Chemistry C* **2007**, *111* (42), 15350–15356. https://doi.org/10.1021/jp074723h.

(207) Stankiewicz, A.; Ionkina, N.; Motherwell, B.; Bennett, B.; Wint, O.; Mastalerz, M. Kerogen Density Revisited - Lessons from the Duvernay Shale. *Society of Petroleum Engineers - Unconventional Resources Technology Conference, URTeC 2015* **2015**, 864–874. https://doi.org/10.2118/178647-ms.

(208) Yiannourakou, M.; Ungerer, P.; Leblanc, B.; Rozanska, X.; Saxe, P.; Vidal-Gilbert, S.; Gouth, F.; Montel, F. Modé Lisation Moléculaire de l'adsorption Dans Les Solides Microporeux. *Oil and Gas Science and Technology* **2013**, *68* (6), 977–994. https://doi.org/10.2516/ogst/2013134.

(209) Facelli, J.; Pugmire, R.; Pimienta, I. *Atomistic Modeling of Oil Shale Kerogens and Asphaltenes along with Their Interactions with the Inorganic Mineral Matrix*; Pittsburgh, PA, and Morgantown, WV (United States), 2011. https://doi.org/10.2172/1113672.

(210) Okiongbo, K. S.; Aplin, A. C.; Larter, S. R. Changes in Type II Kerogen Density as a Function of Maturity: Evidence from the Kimmeridge Clay Formation. *Energy and Fuels* **2005**, *19* (6), 2495–2499. https://doi.org/10.1021/ef050194+.

(211) Jiménez, A.; Iglesias, M. J.; Laggoun-Défarge, F.; Suárez-Ruiz, I. Study of Physical and Chemical Properties of Vitrinites. Inferences on Depositional and Coalification Controls. *Chem Geol* **1998**, *150* (3–4), 197–221. https://doi.org/10.1016/S0009-2541(98)00048-5.

(212) Chalmers, G. R. L.; Marc Bustin, R. On the Effects of Petrographic Composition on Coalbed Methane Sorption. *Int J Coal Geol* **2007**, *69* (4), 288–304. https://doi.org/10.1016/j.coal.2006.06.002.

(213) Lu, X. C.; Li, F. C.; Watson, A. T. Adsorption Measurements in Devonian Shales. *Fuel* **1995**, *74* (4), 599–603. https://doi.org/10.1016/0016-2361(95)98364-K.

(214) Chalmers, G. R. L.; Bustin, R. M. The Organic Matter Distribution and Methane Capacity of the Lower Cretaceous Strata of Northeastern British Columbia, Canada. *Int J Coal Geol* **2007**, *70* (1-3 SPEC. ISS.), 223–239. https://doi.org/10.1016/j.coal.2006.05.001.

(215) Rexer, T. F.; Mathia, E. J.; Aplin, A. C.; Thomas, K. M. High-Pressure Methane Adsorption and Characterization of Pores in Posidonia Shales and Isolated Kerogens. *Energy and Fuels* **2014**, *28* (5), 2886–2901. https://doi.org/10.1021/ef402466m.

(216) Zhang, T.; Ellis, G. S.; Ruppel, S. C.; Milliken, K.; Yang, R. Effect of Organic-Matter Type and Thermal Maturity on Methane Adsorption in Shale-Gas Systems. *Org Geochem* **2012**, *47*, 120–131. https://doi.org/10.1016/j.orggeochem.2012.03.012.

(217) Loucks, R. G.; Reed, R. M.; Ruppel, S. C.; Hammes, U. Spectrum of Pore Types and Networks in Mudrocks and a Descriptive Classification for Matrix-Related Mudrock Pores. *Am Assoc Pet Geol Bull* **2012**, *96* (6), 1071–1098. https://doi.org/10.1306/08171111061.

(218) Eberle, A. P. R.; King, H. E.; Ravikovitch, P. I.; Walters, C. C.; Rother, G.; Wesolowski, D. J. Direct Measure of the Dense Methane Phase in Gas Shale Organic Porosity by Neutron Scattering. *Energy and Fuels* **2016**, *30* (11), 9022–9027. https://doi.org/10.1021/acs.energyfuels.6b01548.

(219) Bowers, G. M.; Loring, J. S.; Schaef, H. T.; Walter, E. D.; Burton, S. D.; Hoyt, D. W.; Cunniff, S. S.; Loganathan, N.; Kirkpatrick, R. J. Interaction of Hydrocarbons with Clays under Reservoir Conditions: In Situ Infrared and Nuclear Magnetic Resonance Spectroscopy and X-Ray Diffraction for Expandable Clays with Variably Wet Supercritical Methane. *ACS Earth Space Chem* **2018**, *2* (7), 640–652. https://doi.org/10.1021/acsearthspacechem.8b00039.

(220) Bowker, K. A. Barnett Shale Gas Production, Fort Worth Basin: Issues and Discussion. *American Association of Petroleum Geologists Bulletin* **2007**, *91* (4), 523–533. https://doi.org/10.1306/06190606018.

(221) Sun, Y.; Li, S.; Sun, R.; Liu, X.; Pu, H.; Zhao, J. Study of CO2enhancing Shale Gas Recovery Based on Competitive Adsorption Theory. *ACS Omega* **2020**, *5* (36), 23429–23436. https://doi.org/10.1021/acsomega.0c03383.

(222) Howarth, R. W.; Santoro, R.; Ingraffea, A. Methane and the Greenhouse-Gas Footprint of Natural Gas from Shale Formations. *Clim Change* **2011**, *106* (4), 679–690. https://doi.org/10.1007/s10584-011-0061-5.

(223) Zhang, Y.; Gautam, R.; Pandey, S.; Omara, M.; Maasakkers, J. D.; Sadavarte, P.; Lyon, D.; Nesser, H.; Sulprizio, M. P.; Varon, D. J.; Zhang, R.; Houweling, S.; Zavala-Araiza, D.; Alvarez, R. A.; Lorente, A.; Hamburg, S. P.; Aben, I.; Jacob, D. J. Quantifying Methane Emissions from the Largest Oil-Producing Basin in the United States from Space. *Sci Adv* **2020**, *6* (17), eaaz5120. https://doi.org/10.1126/sciadv.aaz5120.

(224) U.S. EPA. *Hydraulic Fracturing for Oil and Gas: Impacts from the Hydraulic Fracturing Water Cycle on Drinking Water Resources in the United States. Executive Summary*; U.S. Environmental Protection Agency, Washington, DC, EPA/600/R-16/236ES, 2016.

(225) Konschnik, K.; Dayalu, A. Hydraulic Fracturing Chemicals Reporting: Analysis of Available Data and Recommendations for Policymakers. *Energy Policy*. V3 ed. Harvard Dataverse 2016, pp 504–514. https://doi.org/10.1016/j.enpol.2015.11.002.

(226) Kim, T. H.; Cho, J.; Lee, K. S. Evaluation of CO2 Injection in Shale Gas Reservoirs with Multi-Component Transport and Geomechanical Effects. *Appl Energy* **2017**, *190*, 1195–1206. https://doi.org/10.1016/j.apenergy.2017.01.047.

(227) Li, X.; Elsworth, D. Geomechanics of CO2 Enhanced Shale Gas Recovery. *J Nat Gas Sci Eng* **2014**, *26*, 1607–1619. https://doi.org/10.1016/j.jngse.2014.08.010.

(228) Oldenburg, C. M.; Pruess, K.; Benson, S. M. Process Modeling of CO2 Injection into Natural Gas Reservoirs for Carbon Sequestration and Enhanced Gas Recovery. *Energy and Fuels* **2001**, *15* (2), 293–298. https://doi.org/10.1021/ef000247h.

(229) Godec, M.; Koperna, G.; Petrusak, R.; Oudinot, A. Potential for Enhanced Gas Recovery and CO2 Storage in the Marcellus Shale in the Eastern United States. *Int J Coal Geol* **2013**, *118*, 95–104. https://doi.org/10.1016/j.coal.2013.05.007.

(230) Lillies, A. T. Sand Fracturing with Liquid Carbon Dioxide. In *Annual Technical Meeting, ATM 1982*; 1982; pp 6–9. https://doi.org/10.2118/82-33-23.

(231) Godec, M.; Koperna, G.; Petrusak, R.; Oudinot, A. Enhanced Gas Recovery and CO2 Storage in Gas Shales: A Summary Review of Its Status and Potential. *Energy Procedia* **2014**, *63*, 5849–5857. https://doi.org/10.1016/j.egypro.2014.11.618.

(232) Jin, Z.; Firoozabadi, A. Thermodynamic Modeling of Phase Behavior in Shale Media. *SPE Journal* **2016**, *21* (1), 190–207. https://doi.org/10.2118/176015-PA.

(233) Hill, D. G.; Nelson, C. R. Gas Productive Fractured Shales: An Overview and Update. *Gas TIPS* **2000**, *6* (2), 4–13.

(234) John B. Curtis. Fractured Shale-Gas Systems. *Am Assoc Pet Geol Bull* **2002**, *86* (11), 1921–1938. https://doi.org/10.1306/61eeddbe-173e-11d7-8645000102c1865d.

(235) Chen, F.; Lu, S.; Ding, X.; Ju, Y. Evaluation of the Density and Thickness of Adsorbed Methane in Differently Sized Pores Contributed by Various Components in a Shale Gas Reservoir: A Case Study of the Longmaxi Shale in Southeast Chongqing, China. *Chemical Engineering Journal* **2019**, *367*, 123–138. https://doi.org/10.1016/j.cej.2019.02.105.

(236) Chai, D.; Yang, G.; Fan, Z.; Li, X. Gas Transport in Shale Matrix Coupling Multilayer Adsorption and Pore Confinement Effect. *Chemical Engineering Journal* **2019**, *370*, 1534–1549. https://doi.org/10.1016/j.cej.2019.03.276.

(237) Chareonsuppanimit, P.; Mohammad, S. A.; Robinson, R. L.; Gasem, K. A. M. High-Pressure Adsorption of Gases on Shales: Measurements and Modeling. *Int J Coal Geol* **2012**, *95*, 34–46. https://doi.org/10.1016/j.coal.2012.02.005.

(238) Sun, Z.; Li, X.; Liu, W.; Zhang, T.; He, M.; Nasrabadi, H. Molecular Dynamics of Methane Flow Behavior through Realistic Organic Nanopores under Geologic Shale Condition: Pore Size and Kerogen Types. *Chemical Engineering Journal* **2020**, *398* (November 2019), 124341. https://doi.org/10.1016/j.cej.2020.124341.

(239) Tissot, B. P.; Welte, D. H. *Petroleum Formation and Occurrence*; Springer Berlin Heidelberg: Berlin, Heidelberg, 1984. https://doi.org/10.1007/978-3-642-87813-8.

(240) Wang, T.; Tian, S.; Li, G.; Zhang, L.; Sheng, M.; Ren, W. Molecular Simulation of Gas Adsorption in Shale Nanopores: A Critical Review. *Renewable and Sustainable Energy Reviews* **2021**, *149* (June), 111391. https://doi.org/10.1016/j.rser.2021.111391.

(241) Wang, T.; Tian, S.; Li, G.; Sheng, M.; Ren, W.; Liu, Q.; Zhang, S. Molecular Simulation of CO2/CH4 Competitive Adsorption on Shale Kerogen for CO2

Sequestration and Enhanced Gas Recovery. *Journal of Physical Chemistry C* **2018**, *122* (30), 17009–17018. https://doi.org/10.1021/acs.jpcc.8b02061.

(242) Pathak, M.; Huang, H.; Meakin, P.; Deo, M. Molecular Investigation of the Interactions of Carbon Dioxide and Methane with Kerogen: Application in Enhanced Shale Gas Recovery. *J Nat Gas Sci Eng* **2018**, *51* (December 2017), 1–8. https://doi.org/10.1016/j.jngse.2017.12.021.

(243) Li, Z.; Yao, J.; Firoozabadi, A. Kerogen Swelling in Light Hydrocarbon Gases and Liquids and Validity of Schroeder's Paradox. *Journal of Physical Chemistry C* **2021**, *125* (15), 8137–8147. https://doi.org/10.1021/acs.jpcc.0c10362.

(244) Yu, K. Bin; Bowers, G. M.; Loganathan, N.; Kalinichev, A. G.; Yazaydin, A. O. Diffusion Behavior of Methane in 3D Kerogen Models. *Energy and Fuels* **2021**, *35* (20), 16515–16526. https://doi.org/10.1021/acs.energyfuels.1c02167.

(245) Collell, J.; Galliero, G.; Gouth, F.; Montel, F.; Pujol, M.; Ungerer, P.; Yiannourakou, M. Molecular Simulation and Modelisation of Methane/Ethane Mixtures Adsorption onto a Microporous Molecular Model of Kerogen under Typical Reservoir Conditions. *Microporous and Mesoporous Materials* **2014**, *197*, 194–203. https://doi.org/10.1016/j.micromeso.2014.06.016.

(246) Adewumi Babatunde, K.; Mamo Negash, B.; Rashik Mojid, M.; Ahmed, T. Y.; Regassa Jufar, S. Molecular Simulation Study of CO2/CH4 Adsorption on Realistic Heterogeneous Shale Surfaces. *Appl Surf Sci* **2021**, *543* (December 2020), 148789. https://doi.org/10.1016/j.apsusc.2020.148789.

(247) Huang, L.; Zhou, W.; Xu, H.; Wang, L.; Zou, J.; Zhou, Q. Dynamic Fluid States in Organic-Inorganic Nanocomposite: Implications for Shale Gas Recovery and CO2 Sequestration. *Chemical Engineering Journal* **2021**, *411* (December 2020), 128423. https://doi.org/10.1016/j.cej.2021.128423.

(248) Zhang, K.; Jiang, H.; Qin, G. Utilization of Zeolite as a Potential Multi-Functional Proppant for CO2 Enhanced Shale Gas Recovery and CO2 Sequestration: A Molecular Simulation Study on the Competitive Adsorption of CH4 and CO2 in

Zeolite and Organic Matter. *Fuel* **2019**, *249* (December 2018), 119–129. https://doi.org/10.1016/j.fuel.2019.03.061.

(249) Zhang, K.; Jiang, H.; Qin, G. Utilization of Zeolite as a Potential Multi-Functional Proppant for CO2 Enhanced Shale Gas Recovery and CO2 Sequestration: A Molecular Simulation Study of the Impact of Water on Adsorption in Zeolite and Organic Matter. *Fuel* **2021**, *292*, 120312. https://doi.org/10.1016/j.fuel.2021.120312.

(250) Li, J.; Wang, Y.; Chen, Z.; Rahman, S. S. Effects of Moisture, Salinity and Ethane on the Competitive Adsorption Mechanisms of CH4/CO2 with Applications to Coalbed Reservoirs: A Molecular Simulation Study. *J Nat Gas Sci Eng* **2021**, *95* (May), 104151. https://doi.org/10.1016/j.jngse.2021.104151.

(251) Li, J.; Wang, Y.; Chen, Z.; Rahman, S. S. Insights into the Molecular Competitive Adsorption Mechanism of CH4/CO2in a Kerogen Matrix in the Presence of Moisture, Salinity, and Ethane. *Langmuir* **2021**, *37* (43), 12732–12745. https://doi.org/10.1021/acs.langmuir.1c02274.

(252) Zhou, J.; Zhang, J.; Yang, J.; Jin, Z.; Luo, K. H. Mechanisms for Kerogen Wettability Transition from Water-Wet to CO2-Wet: Implications for CO2 Sequestration. *Chemical Engineering Journal* **2022**, *428*, 132020. https://doi.org/10.1016/j.cej.2021.132020.

(253) Karmakar, T.; Piaggi, P. M.; Perego, C.; Parrinello, M. A Cannibalistic Approach to Grand Canonical Crystal Growth. *J Chem Theory Comput* **2018**, *14* (5), 2678–2683. https://doi.org/10.1021/acs.jctc.8b00191.

(254) Perego, C.; Salvalaglio, M.; Parrinello, M. Molecular Dynamics Simulations of Solutions at Constant Chemical Potential. *Journal of Chemical Physics* **2015**, *142* (14). https://doi.org/10.1063/1.4917200.

(255) Ozcan, A.; Semino, R.; Maurin, G.; Yazaydin, A. O. Modeling of Gas Transport through Polymer/MOF Interfaces: A Microsecond-Scale Concentration Gradient-Driven Molecular Dynamics Study. *Chemistry of Materials* **2020**, *32* (3), 1288–1296. https://doi.org/10.1021/acs.chemmater.9b04907.

(256) Ozcan, A.; Perego, C.; Salvalaglio, M.; Parrinello, M.; Yazaydin, O. Concentration Gradient Driven Molecular Dynamics: A New Method for Simulations of Membrane Permeation and Separation. *Chem Sci* **2017**, *8* (5), 3858–3865. https://doi.org/10.1039/c6sc04978h.

(257) Loganathan, N.; Bowers, G. M.; Ngouana Wakou, B. F.; Kalinichev, A. G.; Kirkpatrick, R. J.; Yazaydin, A. O. Understanding Methane/Carbon Dioxide Partitioning in Clay Nano- and Meso-Pores with Constant Reservoir Composition Molecular Dynamics Modeling. *Physical Chemistry Chemical Physics* **2019**, *21* (13), 6917–6924. https://doi.org/10.1039/c9cp00851a.

(258) Tribello, G. A.; Bonomi, M.; Branduardi, D.; Camilloni, C.; Bussi, G. PLUMED 2: New Feathers for an Old Bird. *Comput Phys Commun* **2014**, *185* (2), 604–613. https://doi.org/10.1016/j.cpc.2013.09.018.

(259) The PLUMED consortium. Promoting Transparency and Reproducibility in Enhanced Molecular Simulations. *Nat Methods* **2019**, *16* (8), 670–673. https://doi.org/10.1038/s41592-019-0506-8.

(260) Cygan, R. T.; Romanov, V. N.; Myshakin, E. M. Molecular Simulation of Carbon Dioxide Capture by Montmorillonite Using an Accurate and Flexible Force Field. *Journal of Physical Chemistry C* **2012**, *116* (24), 13079–13091. https://doi.org/10.1021/jp3007574.

(261) Tan, K. L.; Hameed, B. H. Insight into the Adsorption Kinetics Models for the Removal of Contaminants from Aqueous Solutions. *J Taiwan Inst Chem Eng* **2017**, *74*, 25–48. https://doi.org/10.1016/j.jtice.2017.01.024.

(262) Simonin, J. P. On the Comparison of Pseudo-First Order and Pseudo-Second Order Rate Laws in the Modeling of Adsorption Kinetics. *Chemical Engineering Journal* **2016**, *300*, 254–263. https://doi.org/10.1016/j.cej.2016.04.079.

(263) Ballard, A. L.; Sloan, E. D. The Next Generation of Hydrate Prediction: An Overview. *Journal of Supramolecular Chemistry* **2002**, *2* (4–5), 385–392. https://doi.org/10.1016/S1472-7862(03)00063-7.

(264) Ho, Y. S.; McKay, G. Pseudo-Second Order Model for Sorption Processes. *Process Biochemistry* **1999**, *34* (5), 451–465. https://doi.org/10.1016/S0032-9592(98)00112-5.

(265) McKay, G.; Ho, Y. S.; Ng, J. C. Y. Biosorption of Copper from Waste Waters: A Review. *Separation and Purification Methods* **1999**, *28* (1), 87–125. https://doi.org/10.1080/03602549909351645.

(266) Ho, Y. S.; McKay, G. The Sorption of Lead(II) Ions on Peat. *Water Res* **1999**, *33* (2), 578–584. https://doi.org/10.1016/S0043-1354(98)00207-3.

(267) Plazinski, W.; Rudzinski, W.; Plazinska, A. Theoretical Models of Sorption Kinetics Including a Surface Reaction Mechanism: A Review. *Adv Colloid Interface Sci* **2009**, *152* (1–2), 2–13. https://doi.org/10.1016/j.cis.2009.07.009.

(268) Rudzinski, W.; Plazinski, W. Studies of the Kinetics of Solute Adsorption at Solid/Solution Interfaces: On the Possibility of Distinguishing between the Diffusional and the Surface Reaction Kinetic Models by Studying the Pseudo-First-Order Kinetics. *Journal of Physical Chemistry C* **2007**, *111* (41), 15100–15110. https://doi.org/10.1021/jp073249c.